EVALUATION OF A NOVEL AERO-ENGINE NOSE CONE ANTI-ICING SYSTEM USING A ROTATING HEAT PIPE

EVALUATION OF A NOVEL AERO-ENGINE NOSE CONE ANTI-ICING SYSTEM USING A ROTATING HEAT PIPE

By

SCOTT ANDREW GILCHRIST, B.ENG.

A Thesis

Submitted to the School of Graduate Studies

In Partial Fulfillment of the Requirements

For the Degree

Master of Applied Science

McMaster University

MASTER OF APPLIED SCIENCE (2005) McMaster University
(Mechanical Engineering) Hamilton, Ontario.

TITLE: Evaluation of a Novel Aero-engine Nose Cone Anti-icing System Using a Rotating Heat Pipe.

AUTHOR: Scott Andrew Gilchrist
B.Eng. (McMaster University, Canada, 2002)

SUPERVISOR: Drs. Daniel Ewing and Chan Y. Ching
Department of Mechanical Engineering

NUMBER OF PAGES: xviii, 186.

Abstract

Preventing ice accumulation on aircraft surfaces is important to maintain safe operation during flight. Ice accumulation on aero-engine nose cones is detrimental as large pieces may break off and be ingested into the engine damaging the compressor blades. Currently, hot bleed air is taken from the compressor and blown over the inside and outside surfaces of the nose cone to prevent ice formation on the surface. Although effective, this technique reduces the efficiency of the aero-engine. This investigation evaluates the performance of a novel anti-icing system that uses a rotating heat pipe to transfer heat from the engine to the nose cone. Rotating heat pipes are effective two-phase heat transfer devices capable of transporting large amounts of heat over small temperature differences and cross-sectional areas. In this system, waste heat that is generated in the engine would be transferred to the rotating heat pipe at an evaporator and then transferred into the critical areas of the nose cone at a condenser preventing ice accumulation on the outside surface.

In this investigation, the heat is transferred into the heat pipe from a fluid heated by the engine that would pass through a small annular gap between the rotating heat pipe and a stationary wall. The heat transfer for this configuration and the effect of passive heat transfer augmentation on the outside of the rotating heat pipe in the jacket was investigated experimentally for a range of Taylor numbers of $10^6 < Ta < 5\times10^7$ and for axial Reynolds numbers of $900 < \mathrm{Re}_x < 2100$, characteristic of this configuration when

engine lubricant was used as the working fluid. It was found that by using an array of three-dimensional cubical protrusions, the heat transfer in the evaporator could be increased by 35% to 100%. This result was better than that found using two-dimensional rib roughness. It was also found that the evaporator performance was a limiting factor in the heat transfer performance of the system under most conditions, so further optimization of the evaporator is important.

In the proposed condenser design, the condenser section of the rotating heat pipe would be encased in a lightweight, high conductivity polycrystalline graphite or similar composite material and the end of the heat pipe would be in direct contact with the nose cone. It was found that the end-wall of the heat pipe was not a source of high heat transfer, however it provided an effective means for heating the tip of the nose cone. The effect of using heating channels on the inside of the nose cone was also considered. Here, the condensate from the rotating heat pipe was driven through small radially spaced channels on the inside surface of the nose cone. The heating channels were found to be ineffective due to the small contact area that could be made with the nose cone. This was a result of the limited condensate flow that occurs in rotating heat pipes.

The heat transfer through the proposed system was 700W to 1100W using water and 400W to 800W using ethanol in the heat pipe. It was found that 50% to 75% of the arclength of the nose cone could be maintained above 0°C using water in the heat pipe at an ambient temperature of -30°C and an airplane speed of 300 km/h. This arclength decreased to approximately 25% when ethanol was used as the working fluid. An increase in airplane speed reduced this arclength maintained above 0°C significantly.

Acknowledgements

The author would like to express his gratitude to Dr. Daniel Ewing and Dr. Chan Y. Ching for their invaluable input, experience and encouragement during the completion of this work. The patience and time that they invested are most appreciated. In addition the author would like to thank:

- Mr. Andrew Buyers, Mr. Ron Lodewyks and Mr. David Shick for their guidance and assistance in manufacturing some of the components in the test facility.

- Joseph Brand and Michael Dowhan of Pratt & Whitney Canada and NSERC for the financial and technical support of this work.

- Leslie Aston, Karl Ditschun, John Valley Jr., Tom, Carol, Trevor, John and Joan Gilchrist and Agnes Lamb for their constant support and encouragement.

Table of Contents

List of Figures

List of Tables

Nomenclature

b	Exponent in model for the velocity profile in the evaporator liquid film of the heat pipe.
b_c	Width of heating channel cross-section, (m).
C_f	Friction coefficient for flow over a flat plate in mixed convection.
C_p	Specific heat, (J/kgK).
D	Hydraulic diameter, or diameter (m).
f	Friction factor for orthogonally rotating pipe flow, (dimensionless).
f_o	Friction factor for straight pipe flow, (dimensionless).
F_g	Gap height correction factor for the Taylor number.
$f(r)$	Exterior surface for the heat pipe end wall (m).
h_L	Head loss, (m^2/s^2).
Gr	Grashof number, $Gr = \frac{\omega^2 r \cos(\gamma)\beta\Delta T \delta^3}{\nu^2}$.
h	Heat transfer coefficient, (W/m^2K).
h_c	Heating channel cross-section height (m).
h_{fg}	Latent heat of vapourization, (J/kg).
Ja	Jakob number, $Ja = \frac{C_p \Delta T}{h_{fg}}$.
k	Thermal conductivity, (W/mK).
K	Parameter used to determine friction coefficient C_f for mixed convection.

L Length (m).

m Computational grid co-ordinate (m).

$\dot{m}$ Mass flow rate (kg/s).

n Normalized computational grid co-ordinate, $n = {}^{z}/_{f(r)}$.

Nu Nusselt number, $Nu = \frac{hl}{k}$.

p Computational grid nodal designation.

P Thermodynamic pressure or absolute pressure (Pa).

Pr Prandtl number, $\Pr = \frac{\mu C_p}{k}$.

q Heat transfer rate (W).

Computational grid nodal designation.

q'' Heat flux, (W/m^2).

r Local radius (m).

R Radius of an object or wall (m).

Ra Rayleigh number, $Ra = Gr \Pr$.

Re Reynolds number, $\mathrm{Re} = \frac{ul}{\nu}$.

Re_a Axial Reynolds number of flow over the nose cone, $\mathrm{Re}_a = \frac{Ur}{\nu}$.

Re_ω Rotational Reynolds number of flow over nose cone, $\mathrm{Re}_\omega = \frac{\omega r^2}{\nu}$.

Re^* Modified Reynolds number, $\mathrm{Re}^* = \sqrt{\mathrm{Re}^2{}_\omega + \mathrm{Re}^2{}_a}$.

Re_x Axial Reynolds number in spiral Taylor Couette flow.

s Streamline co-ordinate of the heating channel flow or local arclength along the nose cone surface from the pole (m).

S Arclength of the nose cone from pole to base, (mm or m).

T Temperature (°C or K).

Ta Taylor number, $Ta = \dfrac{\omega^2 r \delta^3}{\nu^2}$.

Ta_m Modified Taylor number, $Ta_m = \dfrac{\omega^2 r_m \delta^3}{\nu^2} \dfrac{1}{F_g{}^2}$.

u Streamwise velocity (m/s).

U Airplane speed or liquid film velocity at the free surface in the rotating heat pipe evaporator (m/s).

v Liquid film velocity normal to the tapered fin wall in the rotating heat pipe condenser (m/s).

x Co-ordinate parallel to the tapered condenser wall (m).

y Co-ordinate normal to the tapered condenser wall (m).

z Co-ordinate normal to the rotating heat pipe end wall (m).

Greek Symbols

α Taper angle of the rotating heat pipe condenser section (°).

β Volumetric expansion coefficient (1/K).

δ Film thickness (m).

Gap height in evaporator (m).

ΔT	Temperature difference.
γ	Taper angle of the evaporator wall in the rotating heat pipe (°).
ρ	Density (kg/m^3).
ρ_{LWC}	Liquid water content in the atmosphere (g/m^3).
τ	Shear stress (Pa).
μ	Absolute viscosity (Ns/m^2).
ν	Kinematic viscosity (m^2/s).
ω	Rotational frequency (rad/s).

Important sub-scripts

c	Heating channel.
co	Heating channel outlet.
f	Forced convection.
finfilm	Refers to the condensate film on the tapered wall of the rotating heat pipe condenser.
gap	Refers to the small gap in the stationary jacket evaporator.
hotfluid	Refers to the fluid heated by the aero-engine used in the evaporator.
i	Inner or center of a discrete control volume.
inf	Ambient.
j	Junction region. Face of a discrete control volume.
m	Mean value.

n	Natural convection.
nc	Nose cone shell.
ncfilm	Condensate film on the end wall of the rotating heat pipe.
o	Nominal value.
pool	Free surface of the pool in the rotating heat pipe condenser.
r	Radial direction.
sat	Saturation.
w	Wall.
wi	Inside wall.
wo	Outside wall.
x	Axial or parallel direction.

Chapter 1 Introduction

Ice accretion may occur on aircraft surfaces when they travel through clouds of suspended water droplets in the atmosphere that remain liquid at sub-zero temperatures. While the smaller particles will follow the flow field around the aircraft, the larger droplets will impact on the surface forming undesirable accumulations of ice. Ice accumulation on the aircraft can increase drag, reduced climbing ability of the aircraft, change the body shape, cause malfunction of wing flaps and result in internal engine damage. The prevention of ice accumulation is usually accomplished using two methods depending upon the location on the aircraft. In the first method, de-icing or partial prevention, ice is allowed to accumulate for a period of time after which it is removed through activation of a de-icing system. For example, wings are typically de-iced using pneumatic boots that inflate and deflate to physically break the ice accumulation off the leading edge. In the second method, anti-icing, a system is used to prevent ice formation by maintaining the impacting water above a temperature where freezing would occur or by evaporating it from the surface. Anti-icing is typically accomplished using chemical means or by heating the surface using electric heaters or hot air from the engine.

The prevention of ice accumulation on the nose cone of small turbo-fan aero-engines is of interest here. Ice accumulation on the nose cone can break off into the engine and damage the fan or compressor blades. Nose cones of small turbo-fan engines are normally anti-iced by blowing hot bleed from the engine compressor over the inside and outside surfaces of the nose cone through piccolo tubes as shown in figure 1.1.

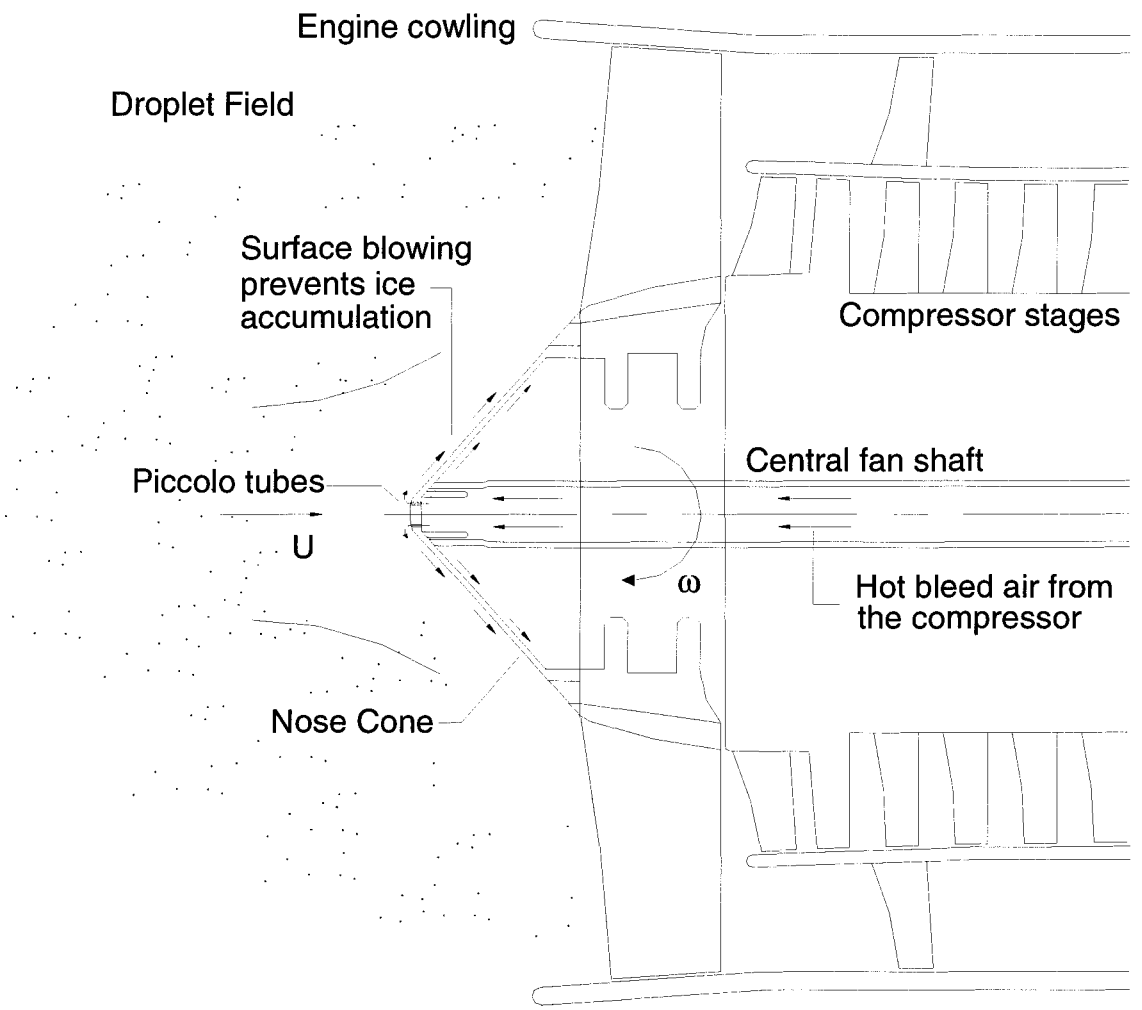

Figure 1.1: Schematic of the method currently used to anti-ice the nose cone of small turbo-fan aero-engines.

Although this method is effective, the use of bleed air from the compressor reduces the efficiency of the engine. Thus, reducing the amount of bleed air required to anti-ice the nose cone would increase the aero-engine efficiency.

The objective here was to evaluate the effectiveness of a novel anti-icing system that uses a rotating heat pipe to transport heat from the engine to the nose cone. A schematic of a typical rotating heat pipe is shown in figure 1.2. The rotating heat pipe consists of a condenser, adiabatic and evaporator section and a fixed charge of working fluid that resides in the cavity. The liquid phase travels along the wall to the evaporator by the centrifugal forces where the heat transfer from outside of the heat pipe causes evaporation of the liquid film on the inside. The vapour travels to the condenser where heat is transferred to a cold environment outside of the heat pipe as the vapour condenses and forms the liquid film on the wall. Rotating heat pipes are effective two-phase heat transfer device that have been considered for heat removal in several high-speed applications. For example, the cooling of electric generators in military aircraft was considered by Ponnappan et al., (1998).

In the proposed system, the evaporator section of the heat pipe would be designed to take heat from either the engine air used to cool the turbine blades or other sources. Similarly, the condenser section would be designed to extract heat from the condenser section of the rotating heat pipe and distribute it throughout the critical areas of the nose cone to prevent ice accumulation. One possible condenser and evaporator design that is considered in this investigation is shown schematically in figure 1.3. In this design, the evaporator consists of a stationary fluid jacket that surrounds the rotating heat pipe

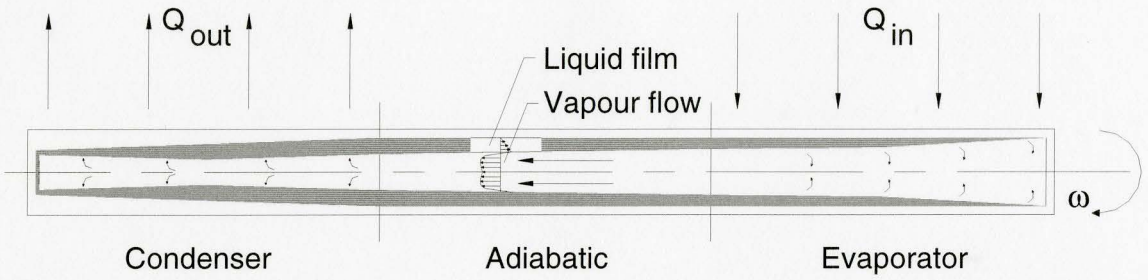

Figure 1.2: Schematic of a rotating heat pipe from Harley and Faghri (1995).

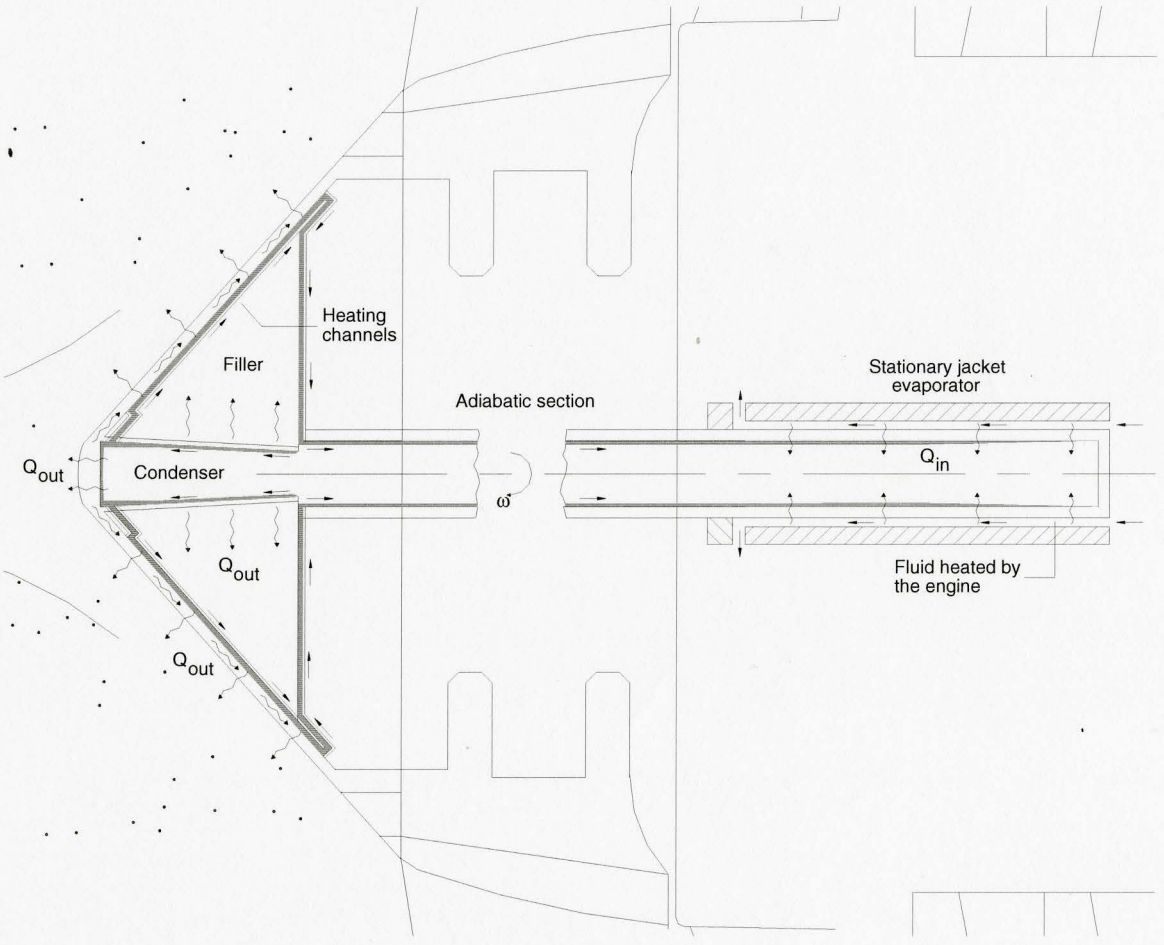

Figure 1.3: The rotating heat pipe anti-icing system with the evaporator and condenser concepts examined in this investigation.

evaporator. Fluid heated by the engine would pass through a small annular gap transferring heat through the heat pipe wall to evaporate the liquid film inside. Space constraints in aero-engines would limit the amount of room for the evaporator so the effect of passive heat transfer enhancement in the evaporator was also considered. In this design, the heat from the rotating heat pipe would be transferred to the nose cone through the end wall of the heat pipe and through a high conductivity filler material that would encase the heat pipe over the length of the condenser. The effect of adding heating channels along the inside of the nose cone was also considered. In this case the condenser would have a taper toward the nose cone that would drive the condensate into a pool above the heating channels. The fluid would then be pumped through the channels by the centrifugal forces and a difference in the radius of the free surface of the pool and the outlet of the channels. These channels would provide additional heating capacity for the nose cone and sub-cool the liquid traveling back to the evaporator.

This work evaluates the expected performance of the proposed rotating heat pipe anti-icing system for the airplane speeds, engine rotation speeds, and geometry typical of a small turbo-fan engine operating in a continuous icing environment. The anti-icing system performance was evaluated by modeling the components in the system independently and then coupling them together into a complete model that was solved iteratively. The literature review presented in chapter 2 outlines work in related fields and provides the basis used to model the system performance. The model for the system components and the overall system are presented in chapter 3. The experimental

investigation used to characterize the heat transfer in the evaporator jacket is presented in chapter 4. The performance of the system was then examined using water and ethanol as the working fluid in the heat pipe and the results are discussed in chapter 5. Conclusions and recommendations for future work are finally given in chapter 6 and 7.

Chapter 2 Literature Review

The proposed aero-engine anti-icing system includes a number of heat transfer processes. The atmospheric conditions and its interaction with the flow over the nose cone determine the heat transfer from the condenser and are examined in the first two sections of this chapter. The research on rotating heat pipes is then reviewed with focus on the condensation and evaporation process under high centrifugal acceleration. The condensation on the end wall of the heat pipe is then reviewed based on the literature for condensation to rotating disks. The investigations of the flow and heat transfer in rotating channels as would occur in the proposed heating channel design, are reviewed in section five followed by a review of investigations of Taylor-Couette flows that would occur in the evaporator in section six. Previous work on rib roughness is examined to provide design criteria for passive heat transfer augmentation in the evaporator. A brief discussion of metal matrix and carbon composite materials that could be used as the filler material to encase the rotating heat pipe condenser concludes the chapter.

2.1 Aircraft Icing

Ice accumulation on aircraft surfaces has an adverse effect on aircraft performance and led the Federal Aviation Administration (FAA) to develop the continuous and intermittent icing envelopes that aircraft may be exposed to during flight (Cebeci and Kafyeke, 2003). The continuous and intermittent icing environments outlined by the FAA are reproduced in figure 2.1. The icing environments are

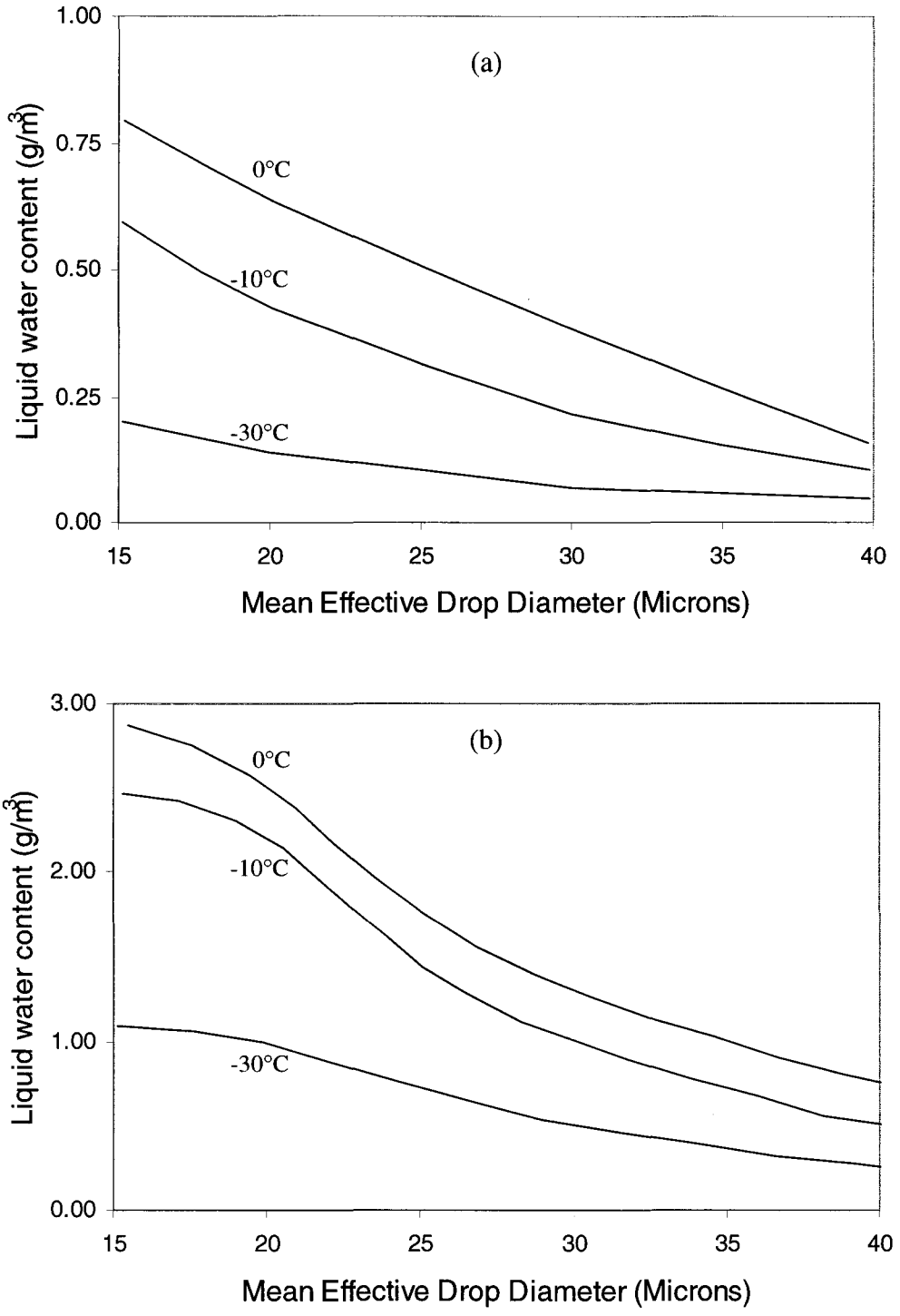

Figure 2.1: Icing envelopes reproduced from the FAR 25 Appendix C; (a) continuous aircraft spectrum and (b) intermittent aircraft icing spectrum.

characterized by the ambient temperature, the mean effective drop diameter and the liquid water content ρ_{LWC}, which is the density of water droplets per cubic meter in the atmosphere. Each curve in figure 2.1 depicts the variation of the liquid water content as a function of the mean effective diameter of the water droplets found in the atmosphere at a given air temperature. The mean effective diameter of the water droplets depends on the type of cloud or precipitation throughout the region in question. The diameter of the droplets in continuous and intermittent icing conditions ranges from 15μm to 40μm. The continuous and intermittent liquid water content is smaller throughout regions with larger drop diameters at lower ambient temperatures. The continuous icing environment has a liquid water content of 0.05 g/m^3 to 1 g/m^3 at ambient temperatures of -30°C to 0°C and could last up to 33 km (Cober et al., 2001). The intermittent liquid water content could be as high as 3 g/m^3. There has been concern about super-cooled large droplet (SLD) environments (Bourgault et al., 2000) that are associated with freezing rain or drizzle type precipitation. Droplet sizes up to 500 μm have been encountered in these environments and their effect on aircraft speed, drag and climb rate can be particularly adverse (Cober et al., 2001).

The icing that occurs on aircraft surfaces during these events is typically classified as either rime ice or glaze ice (Tabrizi and Johnson, 1989). The accretion of rime ice occurs at lower temperatures when droplets impinge on the surface and immediately freeze so that no runback occurs. Glaze icing occurs at warmer temperatures when droplets freeze from the aircraft surface outward while the liquid portion over the ice grows in thickness due to further droplet impingement on the region. The aerodynamic

shear force can overcome the surface tension forces causing the liquid to runback forming horned shaped surfaces about the stagnation points (Tabrizi and Johnson, 1989). Politovich (2003) noted that glaze icing tends to produce a larger penalty in aircraft performance. For rotating components such as the nose cone, the centrifugal force caused by the system rotation would significantly enhance run-back and at larger radii, shed the liquid from the surface. Thus, glaze icing would not appear to be as significant a concern except possibly near the tip of the nose cone.

Ice control systems are typically classified into de-icing or anti-icing systems. De-icing systems remove ice intermittently, whereas anti-icing systems prevent ice accumulation on the surface (Al-Khalil et al., 1990). For fixed wings, pneumatic boots that inflate and deflate are typically used for de-icing. The inflation of these boots physically breaks the ice from the surface however in some cases, complete removal is not achieved and can compromise further de-icing (Tabrizi and Johnson, 1989). For aero-engine nose cones, engine inlet nacelles and other areas, thermal systems employing electric heaters and surface blowing are typically used (Tabrizi and Johnson, 1989, Al-Khalil et al., 1997). In surface blowing anti-icing systems, hot bleed air from the engine compressor is blown over the inside of the surface or out over the surface through piccolo tubes positioned upstream of the icing point (Brown et al., 2002).

The demand for more efficient icing systems and better models to predict ice accretion to airplane surfaces is increasing (Cebeci and Kafyeke, 2003). Some codes currently used to predict ice accretion and icing shapes on the leading edge of fixed wings are LEWICE (Cebeci and Kafyeke, 2003), LEWICE3D (Cebeci and Kafyeke,

2003), CANICE (Cebeci and Kafyeke, 2003), VSAERO/ICE (Al-Khalil et al., 1990), DROP3D (Bourgault et al. 2000) and others. It is currently not possible to fully model the icing process (Bourgault et al., 2000). The problem is normally modeled in several parts outlined by Al-Khalil et al. (1997). The geometry of the surface is defined and typically discretized into panels. A two-dimensional or three-dimensional solution of the flow field is used to compute the flow around the body. The trajectory of the droplets is modeled using a Lagrangian tracking approach. A thermodynamic analysis of the surface, water and air interaction is solved and the models are coupled together and the resulting heat transfer and icing shapes are estimated. Some recent investigations of aircraft icing calculations and anti-icing control systems for fixed wings and engine nacelles are summarized in table 2.1. The icing process on aero-engine nose cones does not appear to be available in the open literature. The amount of compressor bleed air required to anti-ice the nose cone appears to be determined using icing tunnel tests by the manufacturer. This would depend on both the heat removal from both the liquid water content and the air flowing over the nose cone.

2.2 Heat Transfer and Flow Field over the Nose Cone

The heat transfer and ice accretion on the nose cone of an aero-engine depends on the flow field over the nose cone. No icing calculations for aero-engine nose cones were found in the open literature, however there have been a number of investigations of the flow field and heat transfer from rotating bodies in axial flow. A brief summary of some

Table 2.1: Summary of investigations in aircraft icing control.

INVESTIGATORS	APPROACH	STUDY AREA	KEY FINDINGS
Tabrizi and Johnson (1989)	Experimental.	Anti-icing of a typical aircraft leading edge using surface blowing. Leading edge was approximated using a circular cylinder with multiple slots at the stagnation point to issue the hot air. An icing tunnel was used with a spray system.	The surface blowing technique reduced the ice accretion for all slot geometries investigated. Increasing the number of slots and the hot air flow rate reduced the ice accumulation. Air humidity was found to have a significant effect on the icing.
Al-Khalil et al. (1990)	Computational.	Anti-icing of an engine inlet nacelle using the surface blowing technique. VSAERO code was used for the droplet trajectories and a two-dimensional heat transfer analysis was used for the metal skin.	Largest concentration of hot air was required near the stagnation region where direct impingement occurred. Freezing may occur in the run-back water even when the metal skin is at a relatively high temperature; including the run-back water in the thermodynamic analysis is important. Run-back water formed discrete clusters or rivulets.
Al-Khalil et al. (1997)	Computational.	Anti-icing of a commercial jet engine nacelle during climb and decent in -18°C ambient air. Electric heaters and compressor bleed air anti-icing system. Flow field solved using VSAERO code, droplet trajectories solved using ICE code.	Application of a typical icing solver to a commercial jet nacelle provided good agreement to icing tunnel test of icing collection efficiencies on the surface particularly during level flight. The deviation of the results from tests increased for large climb or decent.
Bourgault et al. (2000)	Computational.	The use of an Eulerian approach for droplet impingement prediction over the Lagrangian tracking approach. The DROP3D code was used.	The Navier-Stokes formulation of the problem in an Eulerian reference frame avoids tracking individual particles and generated acceptable results for water droplet impingement on a cylinder and a sphere.
Brown et al. (2002)	Experimental.	Predictions of a heat transfer correlation for an existing engine inlet nacelle anti-icing system using Piccolo tubes.	Results were correlated in the form $Nu = a\,\mathrm{Re}^{b}\left(C_x/d\right)^{c}\,\mathrm{Pr}^{1/3}$, where Re is the Reynolds number of the impingement area, C_x/d is the Piccolo hole spacing to diameter, Pr is the Prandtl number. Smallest hole spacing for the required mass flow rate should be used.
Politovich (2003)	Computational.	Ice accretion to a cylinder using a simple two-dimensional shape with a Lagrangian particle-tracking model.	An accretion based icing intensity index was proposed for airspeeds and geometries typical of several types of aircraft.

key studies is given in table 2.2. Comprehensive reviews of investigations on these flows can be found in Reed and Saric (1989) and Kobayashi (1994).

The initial development of the flow over the rotating nose cone is characterized by a laminar boundary layer and then the formation of the centrifugal or cross flow instability in the transition region. The type of instability depends on the geometry, rotational speed and axial velocity. The centrifugal and cross-flow instabilities are depicted schematically in figure 2.2. The flows over rotating disks exhibit a cross-flow instability where co-rotating vortices form at the transition region, while the flow over rotating cylinders exhibit counter rotating spiral vortices (Reed and Saric, 1989). For rotating cones, the instability depends on the angle of the cone. Kobayashi and Izumi (1983) examined the boundary layer stability on rotating cones in still fluid for total cone angles between 30° and 150°. Counter-rotating spiral vortices similar to those found on a rotating cylinder, were found in the transition region for total cone angles less than 60°. Co-rotating spiral vortices similar to those found on a rotating disk, were found in the transition region for total cone angles greater than 60° (Kobayashi and Izumi, 1983). The critical and transitional Reynolds numbers remained constant for different rotation speeds. Kohama and Kobayashi (1983a) found that an imposed axial flow caused this transition angle to decrease to a value between 30° and 60°. For the case of rotating spheres, co-rotating vortices occur in the transition region due to the cross-flow instability. The transition region moved from the equator to the pole with increasing rotation speed (Kohama and Kobayashi 1983b). It was also found that the critical and transitional Reynolds numbers did not remain constant but increased with rotation speed

Table 2.2: Summary of some investigations on the flow field over rotating bodies in axial flow.

INVESTIGATORS	APPROACH	STUDY AREA	KEY FINDINGS
Kreith et al. (1962)	Experimental. Naphthalene sublimation.	Boundary layer transition on a rotating cone in a quiescent environment.	Critical Reynolds number was characterized as a function of the rotation speed and for taper angles of 30° - 180° (disk). The critical Reynolds number increased from 2×10^4 – 2.2×10^5 as the taper angle increased.
Tien and Campbell (1963)	Experimental. Naphthalene sublimation.	Boundary layer transition and heat and mass transfer from a rotating cone in still fluid (Cone angle: 2α = 90°, 120°, 150°, 180° [disk]).	For the 90°, 120°, 150° angle cones, transition occurred around $\mathrm{Re}=\frac{\omega r^2}{\nu}\sim 180000$. Mass transfer correlations were also proposed.
Kobayashi and Izumi (1983)	Analytical, Experimental. Smoke visualization and hot wire anemometry used.	Boundary layer transition on a rotating cone in still fluid (Cone angle: 2α = 30° - 150°).	For total angles less than 60°, counter-rotating vortices found in the transition region. For total angles greater than 60°, co-rotating vortices similar to the rotating disk were found in the transition region. The critical and transitional Reynolds numbers increased from 10^3 to 6×10^5 as the total cone angle increased through the range where $\mathrm{Re}=\frac{\omega x^2\sin^2\theta}{\nu}$. here x is the distance from the apex along the surface, θ is the half angle of the cone. The number of spiral vortices in the transition region increased from about 22 – 30 as the cone angle increased. Transition Reynolds number remained constant as the rotation speed increased.
Kobayashi et al. (1983).	Experimental. Smoke visualization and hot wire anemometry used.	Boundary layer flow over a rotating 30° included angle sharp cone in axial flow.	Counter rotating spiral vortices were found in the transition region. A second instability superimposed on the primary spiral vortices appeared before the transition to a fully turbulent boundary layer. The boundary layer transition moved towards the apex with increasing rotation speed. The transition Reynolds number decreased with increasing rotation speed and decreasing axial velocity.

Table 2.2 continued.

Kohama and Kobayashi (1983a).	Experimental. Smoke visualization and hot wire anemometry used.	Transition and structure of the boundary layer on rotating bodies in axial flow.	For a rotating cone in still fluid, the spiral vortices are counter rotating for total cone angles up to 60° where after a transition to co-rotating vortices (similar to a disk) occurs. The transition angle decreases to 30° - 60° with an axial flow.
Kohama and Kobayashi (1983b).	Experimental. Smoke visualization and hot wire anemometry.	Transition and structure of the boundary layer on a rotating sphere in still fluid.	Transition region between the pole and equator has the same regular co-rotating spiral vortices as a rotating disk. The transition region moves toward the pole with increasing rotation speed. Critical and transitional Reynolds numbers increase with rotation speed and sphere diameter unlike the rotating cone.
Kohama (1984).	Experimental. Smoke visualization and hot wire anemometry.	Characterization of spiral vortices on a rotating 30° included angle cone in axial flow.	Detailed photographs of the time evolution of the spiral vortices were given. The vortices undergo rapid growth normal to the surface and tear off before the fully turbulent region.
Kohama (1985).	Experimental. Smoke visualization and hot wire anemometry.	Flow structures formed on a slender rotating ogive nose cone in axial flow.	Smoke visualization showed a smooth boundary layer over the initial part of the nose cone and then regular spiral streaks with counter rotating vortices were found in the transition region.
Kobayashi et al. (1988).	Experimental. Smoke visualization and hot wire anemometry.	Transition and structure of the boundary layer on a rotating sphere in axial flow.	Characterized both the laminar and turbulent type boundary layer separation and the transition between the two.
Garrett and Peake (2002).	Analytical.	Instability analysis of the boundary layer on a rotating sphere in still fluid.	The cross-flow instability is prominent below an altitude of 66° measured from the pole to the equator. Above this altitude, the streamline curvature mode was found to be dominant.

and sphere diameter. Garrett and Peake (2002) carried out an analytical study of the boundary layer over a rotating sphere in still fluid and found that the cross flow instability was dominant below an altitude of 66° while a streamline curvature mode was dominant above this. Kobayashi et al. (1988) found that two types of separation occurred on the rotating sphere in an imposed axial flow. Laminar separation occurred for low rotation speeds relative to the axial flow velocity. Turbulent separation occurred for high

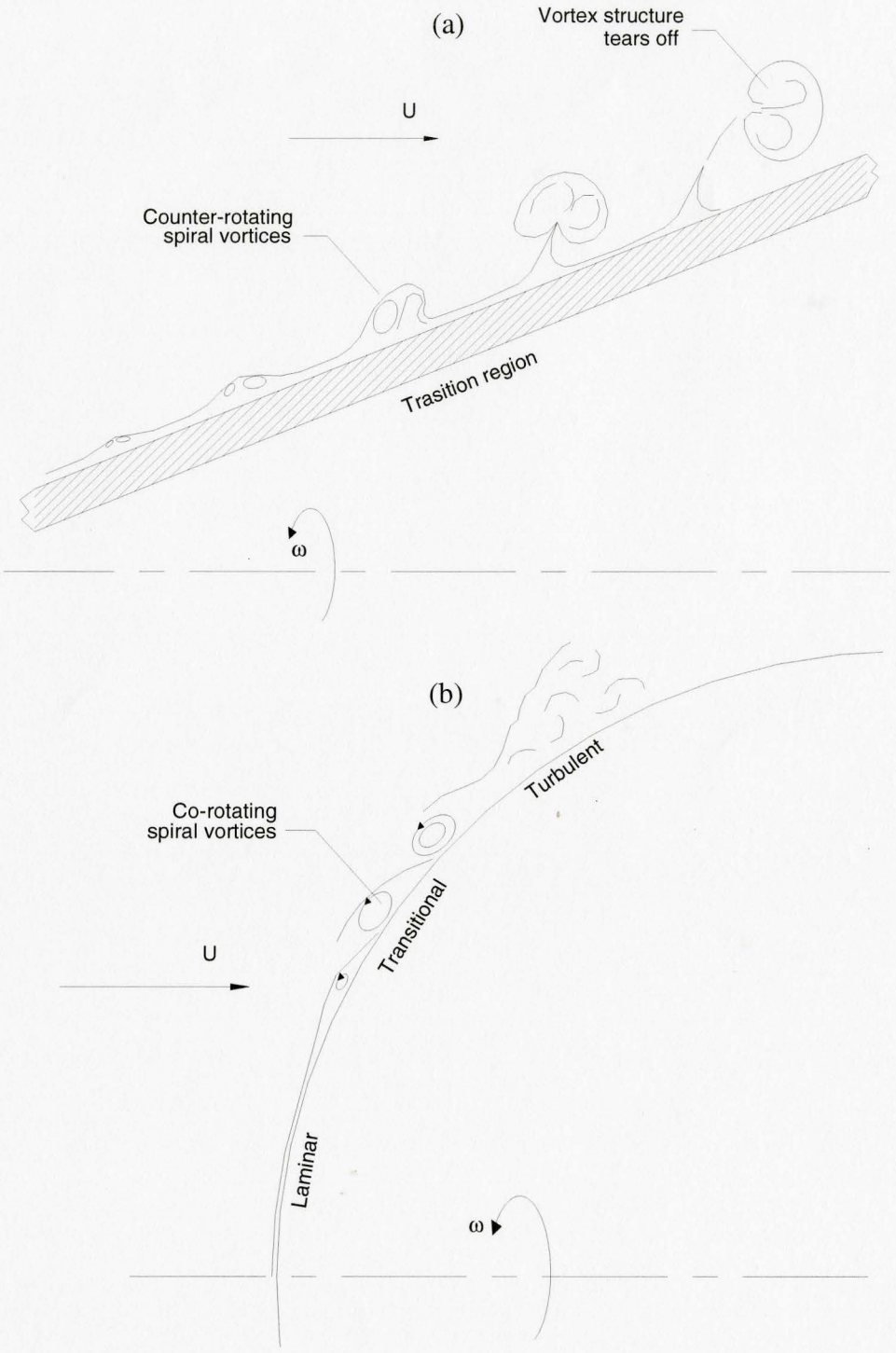

Figure 2.2: (a) schematic of the centrifugal instability over a slender rotating cone in axial flow from Kohama (1984), (b) schematic of the cross-flow instability over a rotating sphere in axial flow from Kohama and Kobayashi (1983b)

rotation speeds relative to the axial flow velocity due to the formation co-rotating spiral vortices in the transition region. This was a result of the cross-flow instability. The effect of increasing the axial velocity shifts the transition region towards the equator of the sphere. As shown below, the transition will occur within a 2mm to 6mm radius of the pole of the nose cone in this application. The total angle of this nose cone is about 84° and thus the boundary layer should exhibit co-rotating spiral vortices due to the cross-flow instability in the transition region and then be turbulent over most of the nose cone.

The heat transfer from rotating bodies in still fluid and axial flow has been examined in several cases. A review of some earlier studies is presented in Kreith (1968), and a brief summary is given in table 2.3 accompanied by some key heat transfer correlations. Heat transfer from a rotating disk in still fluid was considered by Sparrow and Gregg (1959a) analytically for laminar boundary layers and by Edwards et al. (1979) experimentally for both laminar and turbulent boundary layers. A set of mixed convection similarity solutions for rotating disks with and without an imposed axial flow was recently examined numerically by Soong and Chyuan (1998). Heat transfer from various rotating nose cone shapes in axial flow were examined analytically by Tien (1960), Koh and Price (1967) and Ozturk and Ece (1995). Laminar mixed convection heat transfer was considered numerically by Wang (1993) including the effects of sucking and blowing at the nose cone surface, while Hossain and Takhar (1997) included the effects of radiation in the presence of mixed convection. Salzberg and Kezios (1965) measured the heat transfer from a rotating cone with an included angle of 30° in axial flow for laminar and turbulent boundary layers using the Naphthalene sublimation

Table 2.3: Summary of investigations on the heat transfer from rotating bodies in still fluid and axial flow.

INVESTIGATORS	STUDY AREA	KEY FINDINGS
Sparrow and Gregg (1959a)	Heat transfer for the laminar boundary layer due to a rotating disk in still fluid.	Analytical solution of the governing equations were used to compute the average Nusselt number as: $Nu = \frac{h\left(\frac{\nu}{\omega}\right)^{1/2}}{k} = 0.88447\mathrm{Pr} \quad \mathrm{Pr} \to 0$ $Nu = 0.62048\mathrm{Pr}^{1/3} \quad \mathrm{Pr} \to \infty$
Tien (1960)	Heat transfer for the laminar boundary layer due to a rotating cone in still fluid.	Analytical solution of the governing equations were used to compute the average Nusselt number as: $Nu = \frac{h\left(\frac{\nu}{\omega\sin\alpha}\right)^{1/2}}{k} = 0.88447\mathrm{Pr} \quad \mathrm{Pr} \to 0$ $Nu = 0.62048\mathrm{Pr}^{1/3} \quad \mathrm{Pr} \to \infty$
Hartnett and Deland (1961)	Effect of Prandtl number and non-isothermal temperature distributions described by $T_w - T_\infty = Ar^m$ on laminar heat transfer from rotating disks and cones in still fluid.	Rapid increase in thermal boundary layer thickness as the Prandtl number decreased. For a constant Prandtl number, increasing m causes thinning in the thermal boundary layer and higher heat transfer. Significant differences were noted between non-isothermal and isothermal boundary conditions.
Kreith et al. (1963)	Heat transfer from rotating spheres in still fluid.	Experimental results for heat transfer in air were correlated as follows: $Nu_D = 0.43\mathrm{Re}_D^{0.5}\mathrm{Pr}^{0.4} \quad 10^2 < \mathrm{Re}_D < 5\times10^5$ $Nu_D = 0.066\mathrm{Re}_D^{0.67}\mathrm{Pr}^{0.4} \quad 5\times10^5 < \mathrm{Re}_D < 7\times10^6$ where $\mathrm{Re}_D = \frac{\omega D^2}{\nu}$
Salzberg and Kezios (1965)	Heat transfer for laminar and turbulent flow over a rotating 30° included angle cone using the Naphthalene sublimation technique.	Experimental correlations were given as follows: *Laminar* $Nu_s = \frac{hs}{k} = \left[0.73 + 0.03\left(\frac{\omega L\sin\alpha}{U_\infty}\right)\right]\mathrm{Re}_s^{1/2}$ where $\mathrm{Re}_s = \frac{s\left[(\omega x\sin\alpha)^2 + U^2\right]^{1/2}}{\nu}$ *Turbulent* $Nu_s = 0.065\mathrm{Re}_s^{0.8} \quad \mathrm{Re}_{s,c} < \mathrm{Re}_s < 10^6$ Critical Reynolds number for transition was given by $\mathrm{Re}_{x,c} = 110960\left[0.73\left(\frac{U_\infty}{\omega L\sin\alpha}\right)^2 + 0.08\left(\frac{U_\infty}{\omega L\sin\alpha}\right)\right]^{6/7}$

Table 2.3 continued.

Edwards et al. (1979).	Experimental heat transfer from a rotating disk in still fluid.	*Laminar* $$Nu_r = \frac{hr}{k} = \frac{0.585\mathrm{Re}_r^{1/2}}{\frac{0.6}{\mathrm{Pr}} + \frac{0.95}{\mathrm{Pr}^{1/3}}}$$ where $$\mathrm{Re}_r = \frac{\omega r^2}{\nu}$$ *Turbulent* $$Nu_r = 0.021\mathrm{Re}_r^{0.8}\,\mathrm{Pr}^{1/3} \qquad \mathrm{Re}_r > 2\times10^5$$
El-Shaarawi and Al-Jamal (1992).	Computational heat transfer for laminar flow over a rotating sphere in axial flow.	Average Nusselt numbers for sphere correlated by: *Uniform heat flux* $$Nu = \left[0.9142 + 0.053\left(\frac{Ta}{\mathrm{Re}^2}\right)^{0.4296}\right]\mathrm{Re}^{1/2}$$ where $$10^2 < \mathrm{Re} = \frac{U_\infty D}{\nu} < 3\times10^5, \quad 0 < \frac{Ta}{\mathrm{Re}^2} < 2\times10^4, \quad Ta = \frac{\omega^2 D^4}{4\nu^2}$$ *Uniform surface temperature* $$Nu = \left[295.142 + 5.3\left(\frac{Ta}{\mathrm{Re}^2}\right)^{0.3078}\right]\mathrm{Re}^{0.08598}$$
Tieng and Yan (1993).	Heat transfer from a spinning sphere in still fluid.	Mixed convection correlations were given by $$Nu^3 = Nu_N{}^3 + Nu_F{}^3 \qquad 1 \le Gr \le 10^5$$ $$Nu_N = 2 + 0.392Gr^{0.25} \qquad 1 \le Gr \le 10^5$$ $$Nu_F = 2 + 0.175\mathrm{Re}^{0.583} \qquad 10 \le \mathrm{Re} \le 10^4$$ where the subscripts *N, F* indicate natural and forced convection respectively and $$Nu = \frac{\bar{h}D}{k}, \quad Gr = \frac{\beta g \Delta T D^3}{\nu^2}, \quad \mathrm{Re} = \frac{\omega D^2}{\nu}$$
Axcell and Thianpong (2001).	Boundary layer transition and heat transfer from rotating smooth and rough disks in axial flow. Roughness was cubical protrusions of 1 mm and 2.5 mm dimension for pitch to height ratios of 4.8, 9.6, 12.	Boundary layer transition was estimated from heat transfer measurements. The Nusselt numbers were very similar for each roughness configuration and the heat transfer enhancement compared to a smooth disk was on the order of 30% for laminar boundary layers and 100% for turbulent boundary layers. Correlations were provided as follows: *Zero axial flow, laminar, all roughness configurations,* $$Nu = \frac{hr}{k} = 0.39\mathrm{Re}_\omega^{0.5}$$ where $$\mathrm{Re}_\omega = \frac{\omega r^2}{\nu}$$ *Axial flow, turbulent* $\left(4\times10^4 < \mathrm{Re}^* < 3\times10^5\right)$ 1mm cubes, pitch to height ratio = 12: $$Nu = 0.0045\mathrm{Re}^{*0.986},$$ where $$\mathrm{Re}^* = \left(\mathrm{Re}_\omega{}^2 + \mathrm{Re}_a{}^2\right)^{1/2} = \left[\left(\frac{\omega r^2}{\nu}\right)^2 + \left(\frac{Ur}{\nu}\right)^2\right]^{1/2}$$ and U is the approaching free stream velocity.

technique. Kreith (1963) measured forced convection from a rotating sphere in still fluid while Tieng and Yan (1993) measured both the free and forced convection heat transfer. The heat transfer from a rotating sphere in axial flow was considered for laminar boundary layers by Sickmann (1962) and El-Shaarawi and Al-Jamal (1992) for the case of uniform surface heat flux and uniform surface temperature boundary conditions. In the practical icing applications, the presence of droplets and water run-back will likely create roughness on the surface that will enhance the convective heat transfer. The effect of surface roughness on the heat transfer from a rotating disk in axial flow was examined experimentally by Axcell and Thianpong (2001) for three different square arrays of cubic protrusion roughness with pitch to height ratios from 5 to 12. The boundary layer transition occurred at a rotational Reynolds number of $\mathrm{Re}_\omega \approx 2\times10^5$ for the smooth disk where

$$\mathrm{Re}_\omega = \frac{\omega r^2}{\nu}, \tag{2.1}$$

and ω is the rotation frequency, r is the local radius and ν is the kinematic viscosity. For the rough disks, the transition occurred at lower rotational Reynolds numbers of $\mathrm{Re}_\omega \approx 4\times10^4$. The rotational Reynolds number corresponding to transition decreased as the axial velocity increased. It was found that the presence of surface roughness increased the heat transfer by up to 40% in the laminar boundary layer and up to 100% in the turbulent boundary layer. Increasing the axial velocity increased the heat transfer, but the effect of the axial velocity diminished significantly after transition to turbulence. The

effect of the pitch to height ratio on the heat transfer was small. The heat transfer results for 1 mm cubic protrusions in the turbulent regime were correlated by

$$Nu = \frac{hr}{k} = 0.0045 \mathrm{Re}^{*0.986}, \tag{2.2}$$

for $4\times10^4 < \mathrm{Re}^* < 3\times10^5$ where h is the heat transfer coefficient, k is the thermal conductivity. The effective Reynolds number was given by

$$\mathrm{Re}^* = \left(\mathrm{Re}_\omega^{\,2} + \mathrm{Re}_a^{\,2}\right)^{1/2}, \tag{2.3}$$

where Re_a is the axial Reynolds number computed from

$$\mathrm{Re}_a = \frac{Ur}{\nu}, \tag{2.4}$$

where U is the axial velocity of the approaching free stream.

2.3 The Rotating Heat Pipe

The anti-icing system considered here would use a rotating heat pipe to transport the heat from the engine to the nose cone. Gray (1969) originally proposed the rotating heat pipe as a hollow wickless shaft capable of transferring significantly more heat than a similar stationary solid rod. Interest in the use of rotating heat pipes as a thermal management device has increased and many analytical and experimental investigations have followed to characterize their operation. A summary of some investigations on rotating heat pipes is provided in table 2.4. Ballback (1969) developed a modified film condensation approach to characterize the condensation process and liquid film in the condenser. In the approach, the vapour shear stress was neglected and the heat transfer in

Table 2.4: Summary of investigations of rotating heat pipes.

INVESTIGATORS	APPROACH	STUDY AREA	KEY FINDINGS
Daniels and Al-Jumaily (1975)	Analytical, experimental.	2° tapered rotating heat pipe. Analytically modeled the condenser only using modified Nusselt laminar condensation approach including vapour and momentum drag. Experiments performed using a heat pipe charged with water, Arcton 113, 21 for speeds of 600 rpm – 1200 rpm.	Relative agreement between theory and experiment was attained for Arcton 113, 21. Disagreement was found for water; insufficient charge in the experiment claimed as the source. Increases in condenser length, taper angle, rotation speed and the property group $\frac{\rho^2 h_{fg} k^3}{\mu}$, increased the heat transfer. The effective conductivity of the heat pipe was several hundred times that of a copper rod of similar geometry.
Daniels and Williams (1978)	Experimental.	Rotating heat pipe with a 3° condenser and adiabatic section taper and a straight evaporator. Arcton 113 and acetone as working fluids for similar range to Daniels and Al-Jumaily (1975). Effect of non-condensable gas presence.	Non-condensable accumulated in the condenser and gas-blocked the vapour flow. This generates an inactive region in the condenser and reduces the heat transfer performance. Non-condensable creates a stratified layer in the radial direction also reducing the performance. Visual observations include a glass-smooth condenser film and a bubbly evaporator film.
Daniels and Al-Baharnah (1980)	Analytical.	The effect of non-condensable gas presence on rotating heat pipe performance.	Relative agreement in the trends was obtained to the experimental results of Daniels and Williams (1978).
Li et al. (1993)	Analytical.	Coupled heat transfer model for the evaporator, adiabatic, and condenser sections of a tapered rotating heat pipe. Modified Nusselt laminar condensation and evaporation approach used.	Results were characterized as a function of vapour saturation temperature and condenser wall temperature; the evaporator thermal resistance was hence not actually included. Required heat pipe fluid charge increases with increasing speed and heat load.
Ponnappan and Leland (1994)	Experimental.	Experiments on 25.4" diameter stainless steel heat pipes charged with water up to 3500 rpm.	The heat pipe transported up to 1300 W. Impinging air jet cooling of the condenser wall was inadequate however water misting proved adequate. No non-condensable gas problems were encountered. Results differed from computations.

Table 2.4 continued.

Harley and Faghri (1995)	Analytical.	Two-dimensional complete rotating heat pipe model including the vapour flow and transient start-up.	The vapour flow exhibits a flow reversal near the center. The vapour core is large in the evaporator due to blowing and small in the condenser due to sucking. The vapour flow was found to be nearly isothermal.
Ponnappan and Leland (1998)	Experimental.	Experiments on 25.4" diameter stainless steel heat pipes charged with water, methanol and ethanol up to 30000 rpm.	High-speed experimental results were obtained for the first time. Non-condensable gas effects were not encountered. Heat transport capacity did not agree with models of Daniels and Al-Jumaily (1975) and Li et al. (1993). Attributed to inadequate condenser cooling mechanism (air jets and oil mist jets) and questionable validity of laminar film analysis.
Song et al. (2003b)	Analytical.	Complete cycle high-speed rotating heat pipe model developed. Typical Nusselt laminar condenser model was used but a new mixed convection evaporator model presented. One-dimensional vapour flow model included.	Model predictions were in excellent agreement with high-speed test results of Ponnappan et al. (1998). At high speeds nucleate boiling is suppressed and natural convection becomes a dominant heat transfer mechanism in the evaporator film.

the evaporator was not included in the analysis. Daniels and Al-Jumaily (1975) modified the analysis of Ballback (1969) and included the effect of vapour and momentum drag using a one-dimensional model of the vapour flow. The evaporator section was ignored in this case. Various working fluids consisting of Arcton 113, Arcton 21 and water were investigated over a speed range of 600 rpm to 1200 rpm. Qualitative agreement to the model predictions was obtained for the Arcton series, however, the results for water were in complete disagreement. The vapour shear stress was found to be significant only at higher heat fluxes due to higher counter-flow vapour velocities. Daniels and Williams (1978) experimentally examined the effect of a non-condensable gas on rotating heat pipe

performance. Pressure measurements were obtained in the vapour space and visual observations were made through a window in the evaporator end. The non-condensable accumulated in the end wall region of the condenser and then blocked the vapour flow, leaving the end of the condenser relatively inactive and decreased the heat transfer performance. The non-condensable gas also accumulated in the radial direction and produced a stratified layer of vapour-gas mixture. The visual observations showed that the evaporator surface was laden with bubbles while in the condenser end the liquid free surface was glass smooth. The effect of a non-condensable gas presence was examined analytically in Daniels and Al-Baharnah (1980) and the results were in relative agreement with Daniels and Williams (1978).

Li et al. (1993) developed a complete rotating heat pipe model including the adiabatic and evaporator sections. Vapour and non-condensable gas effects were neglected and a modified laminar film condensation and evaporation model was used in the condenser and evaporator respectively. The model was used to characterize the vapour saturation and wall temperature difference in the condenser; hence the thermal resistance of the evaporator was not directly included. Faghri et al. (1993) numerically analyzed the vapour flow in an axially rotating heat pipe and Harley and Faghri (1995) numerically simulated the two-dimensional Navier-Stokes and one dimensional energy equation to model the transient and steady state performance for a heat pipe identical to that used by Daniels and Al-Jumaily (1975).

The previous investigations focused on lower rotation speeds typically less than 2000 rpm, however interest has recently developed in the use of rotating heat pipes for

thermal management in high-speed applications such as the present one. The use of a rotating heat pipes to cool the rotors of high speed military aircraft generators was proposed by Sterby et al. (1996) and Ponnappan and Leland (1998). Ponnappan and Leland (1994) initially investigated the performance of a 25.4 mm diameter stainless steel rotating heat pipes charged with water in the lower speed range (<3500rpm) to support development of a higher speed facility. In this case, the test speed range was 3500 rpm to 7000 rpm using the same water charged heat pipe (Ponnappan and Leland, 1995). Ponnappan et al. (1998) obtained measurements up to 30000 rpm for the first time with both water and methanol charged heat pipes of similar dimensions to the former two studies. The maximum heat transported during the experiments was 1033 W with water as the working fluid while 644 W was transported using methanol indicating that either fluid is a candidate in high-speed applications. The agreement of the experimental data to the model proposed by Daniels and Al-Jumaily (1975) was poor with the model over predicting the performance of the rotating heat pipe by almost an order of magnitude. The authors suggest that the discrepancy may be due to the poor cooling capacity of the condenser in their experiment, and some unknown high-speed dynamics may not be captured in the laminar models. Song et al. (2003b) developed a complete high-speed rotating heat pipe model in order to capture the high-speed dynamics. Following Daniels and Al-Jumaily (1975) and Harley and Faghri (1995), the liquid film in the condenser section was modeled using a laminar film condensation approach. A one dimensional vapour flow model was used similar to Daniels and Al-Jumaily (1975) where the vapour is assumed to be in solid body rotation. Song et al. (2003b) characterized the evaporator

film using a forced and mixed convection model. As proposed by Marto (1984) for the lower speeds, a film evaporation model analogous to the used in the condenser was employed for the high-speed cases since the onset of nucleate boiling is delayed as the system acceleration increases from 20g to 100g (eg. Merte and Clark 1961, Ulucakli and Merte 1990). In particular, Eschweiler et al. (1967) obtained boiling heat transfer measurements in a vertical rotating cylinder for accelerations up to 1280 g and found that nucleate boiling was completely suppressed for accelerations greater than 620g and natural convection became the dominant heat transfer mechanism. Song et al. (2003b) modeled the velocity profile in the film of the evaporator using a power law given by

$$\frac{u}{U} = \left(\frac{y}{\delta}\right)^{b}, \tag{2.5}$$

where U is the maximum film velocity at the liquid vapour interface and the exponent b depends upon the conditions of the flow whether forced or natural convection is present and if the film is laminar or turbulent. The Nusselt number of the liquid film was modeled using a standard correlation for mixed convection boundary layers given by (Churchill 1990, Incopera and DeWitt 1996)

$$Nu_m^{7/2} = Nu_f^{7/2} + Nu_n^{7/2}, \tag{2.6}$$

where Nu_f and Nu_n represent the forced and natural convection contributions respectively. The natural convection Nusselt number was determined using a correlation for natural convection under acceleration recommended by Marto (1984) given by

$$Nu_n = 0.133 Ra^{0.375}. \tag{2.7}$$

The wall shear stress in the liquid film was modeled as a function of the parameter $K = Gr/\mathrm{Re}^{5/2}$ following Afzal and Hussain (1984) for a mixed convection boundary layer on a flat plate. The model predictions were found to be in good agreement with high-speed test results of Ponnappan et al. (1998), Song et al. (2003a) and Song et al. (2003b). It was also noted that the poor performance observed by Ponnappan et al. (1998), was due to the fact that they had approximately 10 times the minimum amount of working fluid required to operate the heat pipe. The model suggested that the performance of the heat pipe could be increased significantly if less working fluid was used. Song et al. (2004) experimentally examined the effect of modest amounts of excess working fluid on the performance of rotating heat pipes. They found for rotating heat pipes with tapered condenser, increasing the fluid charge by a factor of 2 to 3 had little effect on the performance of the device. In this case, the model predicted that the excess fluid would reside in the evaporator and adiabatic sections and had little effect on the natural convection in the evaporator. As the fluid charge in the heat pipe increased, it would affect the film thickness in the condenser and the performance of this section. Thus, the results indicate the fluid distribution in the condenser is important in predicting the performance of the rotating heat pipe.

2.4 Condensation on the End-wall of the Heat Pipe

Condensation on the end-wall of the heat pipe could be important in the current aero-engine application and so it was included in the analysis. A summary of some

investigations in this field is provided in table 2.5. Sparrow and Gregg (1959b) examined the condensation to a rotating, horizontal, isothermal disk that is similar to the current geometry at the end of the heat pipe. The momentum and energy equations were solved in closed form similar to the Von Karman viscous pump problem (eg. Panton, 1996). The results for fluids with $\mathrm{Pr} > 1$ are shown in figure 2.3 as a function of the Jakob number defined by

$$Ja = \frac{C_p \Delta T}{h_{fg}}. \tag{2.8}$$

The Jakob number is the relative magnitude of sub-cooling to latent heat in the condensate film. For cases of small Jakob number or small sub-cooling, the Nusselt number was given by

$$Nu = \frac{h\left(\frac{\nu}{\omega}\right)^{1/2}}{k} = \left(\frac{2}{3}\right)^{1/4}\left(\frac{\mathrm{Pr}}{Ja}\right)^{1/4}. \tag{2.9}$$

The solution represents cases where energy convection and inertia are negligible. The limiting thickness when energy convection and inertia are negligible was given by

$$\delta\left(\frac{\omega}{\nu}\right)^{1/2} = \left(\frac{3}{2}\right)^{1/4}\left(\frac{Ja}{\mathrm{Pr}}\right)^{1/4}. \tag{2.10}$$

In the thin film limit, the condensate rotates as a solid body and is swept along the disk in the radial direction. A simple stretching of the velocity profile occurs in this case. For larger sub-cooling, the energy convection in the liquid film increased the heat transfer because the thermal boundary layer is thinner. For an increase in the inertia, the heat transfer decreased. The condensate layer thickness was found to be constant for an

Table 2.5: Summary of investigations of condensation to rotating bodies.

INVESTIGATORS	APPROACH	STUDY AREA	KEY FINDINGS
Sparrow and Gregg (1959b).	Analytical.	Laminar condensation of quiescent vapour to a rotating horizontal disk. Solution of the momentum and energy equations. Vapour shear stress neglected.	Film dynamics captured by the Jakob number, Prandtl number and length scale $\left(\frac{\nu}{\omega}\right)^{1/2}$. Thin films exhibit solid body rotation while inertia and convection are important in thick films. Film thickness is constant for a uniform temperature disk.
Nandapurkar and Beatty (1960)	Experimental.	Condensation of methanol, ethanol and Arcton 113 to an upside down horizontal water cooled disk.	Heat transfer coefficient was 25% - 30% less than predicted from Sparrow and Gregg (1959b).
Sparrow and Gregg (1960)	Analytical.	Similar methodology to that of Sparrow and Gregg (1959b). Focused on the effect of vapour shear stress.	Vapour shear opposes tangential motion of the film. Radial shear stress increased heat transfer in thin films; maximum velocity occurs in the vapour. The opposite is true for thick films. Maximum vapour shear stress effect was 3% for similar conditions to Nandapurkar and Beatty (1960).
Sparrow and Gregg (1961)	Analytical.	Laminar condensation of a quiescent vapour to a rotating obtuse cone. Solution of the momentum and energy equations. The vapour shear stress was neglected.	Heat transfer coefficient of the cone relative to the disk was always smaller; $\frac{h_{cone}}{h_{disk}} = \sqrt{\sin\alpha}$ where α is the half angle.
Espig and Hoyle (1965)	Experimental.	Presence of surface waves for thin water film flow over a rotating disk, fluid source at the disk center, no condensation.	Surface waves were present for the range $20 < \mathrm{Re} = 4\dot{m}/\pi\mu D < 600$ and the mean film thickness was greater than theoretical predictions.
Espig and Hoyle (1968)	Experimental.	Laminar condensation of quiescent steam to a rotating disk.	Heat transfer results within 80% to 170% of model, discrepancy attributed to the presence of surface waves.
Butuzov and Rifert (1972)	Experimental.	Condensation of steam to an upside down horizontal disk. Rotation speed of 50 rpm – 1900 rpm, ΔT = 1°C, 2.5°C, 4°C.	At low speeds condensate was shed from the surface in drops due to gravity. At higher speeds the film heat transfer followed the expected trend where the results were within 5% - 10% of theory.
Beckett et al. (1973)	Analytical.	Laminar condensation to a rotating horizontal disk. Vapour shear stress and temperature variable fluid properties included.	Predictions up to 27% lower than Sparrow and Gregg (1960) on account of the high non-linearity of the viscosity near the cooled disk surface.

Table 2.5 continued.

Wang and Greif (1981)	Analytical.	Laminar condensation to a rotating disk with an imposed axial flow. Solution of the integral momentum and energy solution accounting for vapour shear stress and impingement.	For Pr = 1 fluids. Low axial impingement velocities decreased the heat transfer while fast impingement velocities increased the heat transfer by up to 13%. For Pr = 10 – 100, effect of impingement was negligible.

isothermal disk. In thicker films, significant variation in the tangential velocity occurs across the thickness and advection of fluid towards the disk surface increases significantly as shown in the components of a typical velocity profile in figure 2.4.

The condensation on a rotating disk has been investigated experimentally in a number of cases. Nandapurkar and Beatty (1960) examined the condensation of methanol, ethanol and Arcton 113 to a water-cooled disk. The heat transfer coefficient was up to 30% smaller than that predicted by the model proposed by Sparrow and Gregg (1959b). The discrepancy was attributed to the vapour shear stress. Sparrow and Gregg (1960) modified their original analysis and included the vapour shear stress. They found that for thin films, the radial vapour drag increased the heat transfer, such as those studied by Nandapurkar and Beatty (1960) because the maximum velocity occurred in the vapour and a positive shear stress occurred at the interface. The opposite was true for thick films. Sparrow and Gregg (1960) found the effect of the vapour shear stress only changed the heat transfer by up to 3% so they thought that this could not explain the discrepancy found by Nandapurkar and Beatty (1960). Butuzov and Rifert (1972) later considered condensation to the downward facing side of a rotating disk for steam. They found that at low speeds, gravity affected the flow distribution however at high speeds the heat transfer results followed the expected trend. Yanniotis and Kolokotsa (1996)

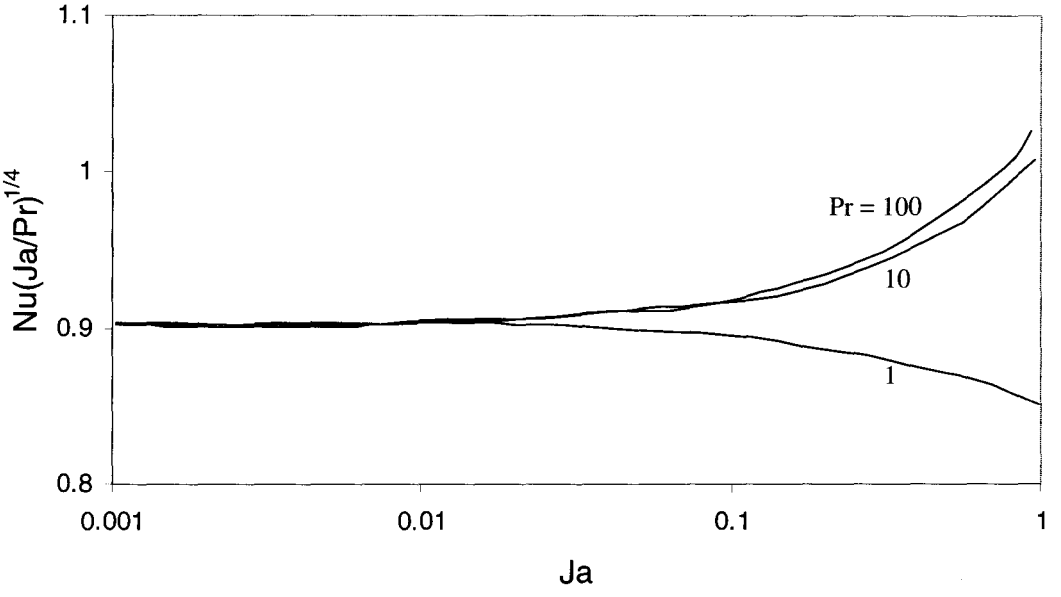

Figure 2.3: Heat transfer results for condensation to a rotating disk from Sparrow and Gregg (1959b).

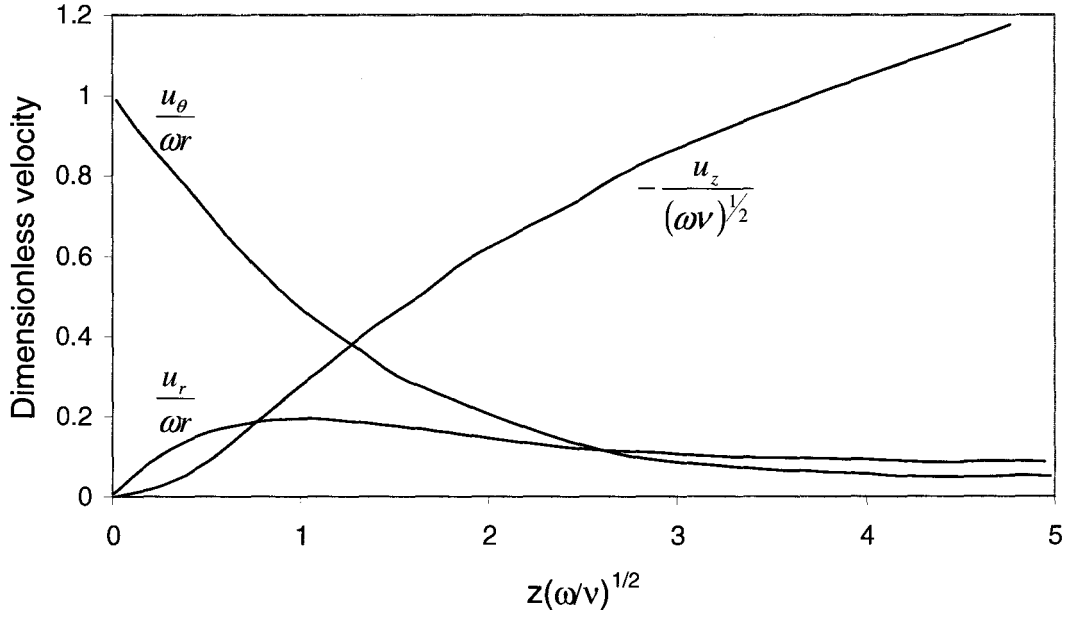

Figure 2.4: Profiles of the velocity components across the condensate layer for a thick film, ($\delta\left(\omega/\nu\right)^{1/2} = 5.0$), from Sparrow and Gregg (1959b). The subscripts *r*, θ, *z* indicate the radial, tangential and normal components.

performed a similar experiment and found that the film thickness and heat transfer were relatively uniform across the disk, however the results deviated from the model by up to 60%. Beckett et al. (1973) re-examined the steam condensation on a rotating disk analytically using the same approach outlined in Sparrow and Gregg (1960), but included variable fluid properties. The predicted heat transfer was up to 27% lower than that predicted by Sparrow and Gregg (1959b) for temperature differences up to 100°C.

The condensate film on the disk can transition from laminar to turbulence. Sparrow and Gregg (1959b) proposed that the film is laminar for $\mathrm{Re} = \omega^2 r / \nu < 3\times10^5$, based on results for single-phase boundary layer flow over a rotating disk found in Schlichting (1955). Espig and Hoyle (1965) experimentally investigated the presence of surface waves on thin water films flowing over a horizontal rotating disk and found surface waves were present for Reynolds numbers in the range of $20 < \mathrm{Re} < 600$ where

$$\mathrm{Re} = \frac{4\dot{m}}{\pi\mu D}, \tag{2.11}$$

and $\dot{m}$ is the mass flow rate and $0.5D$ is the radial position. The measured film thickness in this case was larger than that predicted by the model. Espig and Hoyle (1968) experimentally examined vapour condensation on a vertical rotating disk and found the heat transfer results were within 80% to 170% of the analytical results of Sparrow and Gregg (1959b). The discrepancy was attributed to the presence of surface waves.

In these investigations the condensation occurs from a large volume of quiescent vapour on a rotating disk. In the rotating heat pipe however, the vapour would approach

the end wall condensation film with a non-zero axial velocity. Wang and Greif (1981) analytically considered the effect of vapour impingement for both zero and non-zero vapour shear stress using a formulation similar to Sparrow and Gregg (1960). They found for fluids with Prandtl numbers of 10 and 100 the impingement had no appreciable effect. For fluids with $\mathrm{Pr} = 1$, the heat transfer increased by up to 13%.

2.5 Flow and Heat Transfer in Rotating Serpentine Channels

One possible design considered here to provide additional heating to the nose cone was to pump the condensate from the rotating heat pipe along the inside of the nose cone through radially spaced heating channels. The channels would be similar to the serpentine passages commonly used for turbine blade cooling. In turbine blade cooling, the serpentine channel rotates about an orthogonal axis and fluid is pumped from an inlet at the root of the blade to an outlet. The Coriolis force caused by the rotation produces a secondary flow that affects the heat transfer and the friction factor. The laminar flow and heat transfer in rotating isothermal ducts of rectangular cross section was examined numerically by Hwang and Jen (1990) for Prandtl numbers of 0.7, 7 and aspect ratios of 0.2 to 5. The secondary flow pattern that developed consisted of a pair of counter rotating vortices when the parameter $\mathrm{Re}\,\mathrm{Re}_\omega$ was increased from 0 up to 3×10^5 where

$$\mathrm{Re}\,\mathrm{Re}_\omega = \frac{UD}{\nu}\frac{\omega D^2}{\nu}. \tag{2.12}$$

Here, U is the axial velocity, D is the hydraulic diameter, ω is the rotation speed and ν is the kinematic viscosity. The Coriolis force tends to push fluid from the channel core

towards the trailing wall and induces the vortex motion as the fluid turns toward the sidewalls and distorts the axial velocity profile as shown in figure 2.5. When $\mathrm{Re}\,\mathrm{Re}_{\omega}$ varied from 2.5×10^4 to 3.5×10^4, the flow exhibited a hysteresis where a second weaker pair of vortices also appeared depending on the initial starting conditions of the simulation. Mori and Nakayama (1968) analytically modeled the laminar fluid flow and heat transfer in a radially rotating straight circular pipe. The flow was divided into a core region that was dominated by a secondary flow caused by the Coriolis forces and a near wall boundary layer dominated by the viscous forces. They developed composite velocity and temperature profiles and correlations for the friction factor and average Nusselt number for constant wall temperature and constant heat flux boundary conditions. The ratio of the friction factor for radially rotating pipes relative to stationary pipes was given by

$$\frac{f}{f_o} = 0.118\left(\frac{N}{X}\right)^{1/4} \frac{1}{1-2.82\left(\frac{N}{X}\right)^{-1/4}}, \tag{2.13}$$

where

$$N = \frac{\omega D_c^{\,2}}{2\nu}\mathrm{Re}_D, \tag{2.14}$$

$$X = \left[1+1.25\left(\frac{\omega D_c^{\,2}}{2\nu\,\mathrm{Re}_D}\right)^2\right]^{1/2} - 1.118\left(\frac{\omega D_c^{\,2}}{2\nu\,\mathrm{Re}_D}\right), \tag{2.15}$$

and

$$f_o = \frac{64}{\mathrm{Re}_D}. \tag{2.16}$$

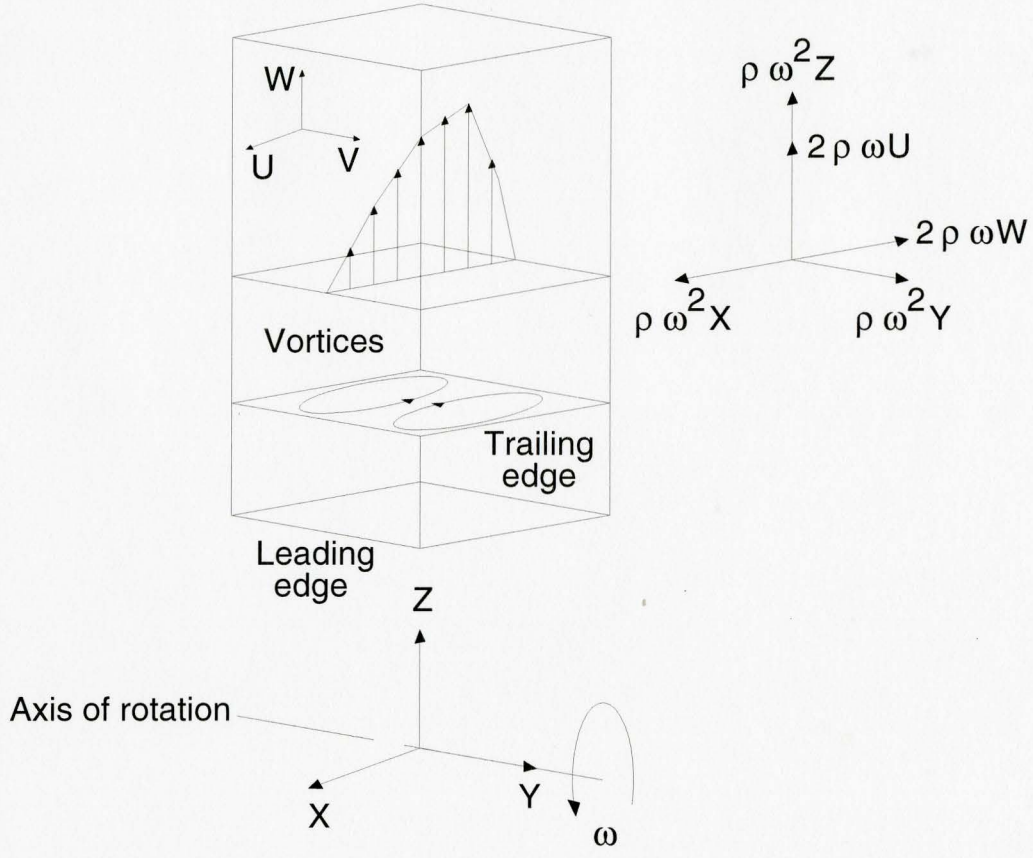

Figure 2.5: Schematic of the secondary flows in a duct rotating about an orthogonal axis from Hwang and Kuo (1997).

For the constant heat flux boundary condition, the ratio of the Nusselt number for radially rotating pipes to stationary pipes was given by

$$\frac{Nu}{Nu_o} = \frac{\frac{0.216}{\zeta}\left(\frac{N}{X}\right)^{1/4}}{1-4.80\left[1-\frac{0.176}{\zeta}-\frac{0.07}{\zeta\,\mathrm{Pr}}\left(\frac{1}{\zeta}+4.33\right)\right]\left(\frac{N}{X}\right)^{-1/4}}, \tag{2.17}$$

for $\mathrm{Pr} \geq 1$ where $Nu_o = 4.36$ and

$$\zeta = \frac{2}{11}\left[1+\left(1+\frac{77}{4X}\frac{1}{\mathrm{Pr}^2}\right)^{1/2}\right], \tag{2.18}$$

while

$$\frac{Nu}{Nu_o} = \frac{\frac{0.216}{\zeta}\left(\frac{N}{X}\right)^{1/4}}{1-2.82\left[\zeta+\frac{0.5}{\zeta}-\frac{0.1}{\zeta^2}-\frac{0.8}{\zeta\,\mathrm{Pr}}\left(\zeta-\frac{0.25}{\zeta}+\frac{0.05}{\zeta^2}\right)\right]\left(\frac{N}{X}\right)^{-1/4}}, \tag{2.19}$$

for $\mathrm{Pr} < 1$ where

$$\zeta = \frac{1}{5}\left[2+\left(\frac{10}{X}\frac{1}{\mathrm{Pr}^2}-1\right)^{1/2}\right]. \tag{2.20}$$

For the constant wall temperature boundary condition, the ratio was given by

$$\frac{Nu}{Nu_o} = \frac{0.258}{\zeta}\left(\frac{N}{\chi}\right)^{1/4}. \tag{2.21}$$

A similar approach was taken by Mori et al. (1971) for turbulent flow in rotating circular pipes. Recent experimental investigations by Morris and Ghavami-Nasr (1991), Yang et al. (1992), Han and Zhang (1992), Han et al. (1993) and Kuo and Hwang (1996) focused

on turbulent flow and heat transfer in rotating rectangular and square serpentine passages for conditions typical of turbine blade cooling. In these studies air was used and the Reynolds number based on hydraulic diameter were typically 1000 – 25000. Heat transfer for each side of the channel was obtained as well as the effect of channel curvature in the turns. It was found that heat transfer on the leading wall was up to 20% lower than in the non-rotating case while the heat transfer on the trailing wall was up to 20% higher than the non-rotating case. This occurs because fluid in the core region is first advected close to the trailing wall due to the Coriolis force and then re-circulated near the leading wall. The heat transfer on the sidewalls was always between that of the leading and trailing walls.

2.6 Heat Transfer in Taylor-Couette Flow with Axial Flow

One of the methods that was considered to add heat from the aero-engine into the rotating heat pipe was a stationary jacket surrounding the heat pipe with a small annular gap between the two. A hot fluid from the engine would then pass through this gap transferring heat to the evaporator section of the rotating heat pipe. The flow produced in the gap is a spiral Taylor-Couette flow that was originally considered by Taylor (1923). For the case of a stationary outer cylinder and a rotating inner cylinder with no axial flow, Taylor showed that pairs of counter-rotating vortices known as Taylor vortices, shown schematically in figure 2.6 form in the axial direction after a critical speed. Further transitions occur as the cylinder speed is increased and numerous investigations have described these transitions in detail. For example, Coles (1965) conducted an

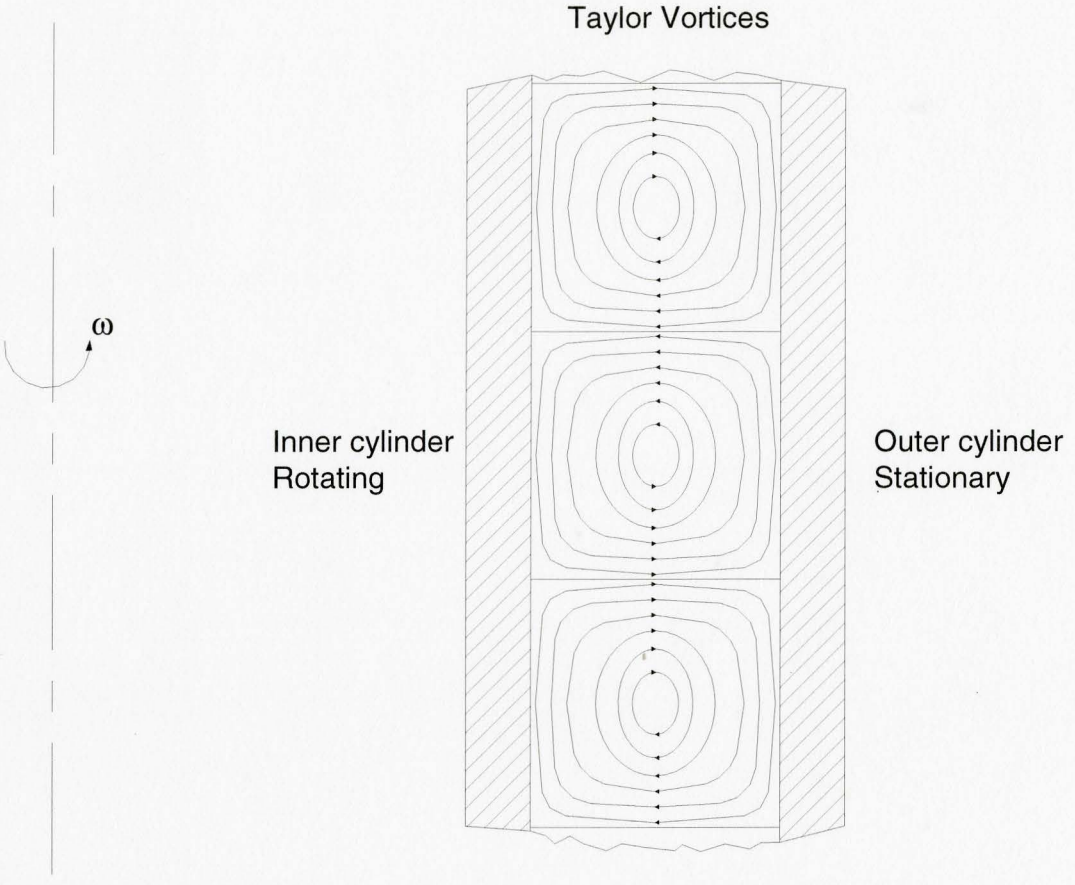

Figure 2.6: Schematic of the streamlines of Taylor vortices in the flow confined between an inner rotating cylinder, above a critical speed, and an outer stationary cylinder (Taylor, 1923).

extensive study and found that as many as 25 different states, defined by the number and speed of the traveling azimuthal waves, could exist at a given rotation speed and up to 70 transitions occur. Andereck et al. (1986) produced a transition map through similar experiments to Coles (1965). A review of other investigations can be found in a number of sources including Maron and Cohen (1991).

The spiral Taylor-Couette flow formed when an axial flow is imposed in the gap is of interest here. The stability of the flow in the gap has been examined extensively in the literature and a summary is provided in table 2.6. Kaye and Elgar (1958) examined the stability of the flow experimentally and proposed that four basic regimes exist, namely, laminar, laminar plus vortices, turbulent and turbulent plus vortices. The flow regimes were characterized using the modified Taylor number given by (Kaye and Elgar, 1958)

$$Ta = \frac{\omega r_m^{1/2}\delta^{3/2}}{\nu}\frac{1}{F_g}, \tag{2.22}$$

where

$$F_g = \frac{\pi^2}{41.2}\left(1-\frac{\delta}{2r_m}\right)^{-1} P^{-1/2}, \tag{2.23}$$

$$P = 0.0571\left[1-0.652\left(\frac{\delta/r_m}{1-\delta/2r_m}\right)\right]+0.00056\left[1-0.652\left(\frac{\delta/r_m}{1-\delta/2r_m}\right)\right]^{-1}, \tag{2.24}$$

and

$$\mathrm{Re}_x = \frac{2U\delta}{\nu}. \tag{2.25}$$

Table 2.6: Investigations on the stability of Taylor-Couette flow with and without axial flow.

INVESTIGATORS	APPROACH	STUDY AREA	KEY FINDINGS
Kaye and Elgar (1958)	Experimental.	Flow regimes and transition in Taylor-Couette flow with an imposed axial flow. Axial Reynolds number varied up to 2000.	Hot wire measurements showed the existence of four basic regimes; laminar, laminar plus vortices, turbulent and turbulent plus vortices. The dimensionless Taylor number was proposed and used to derive the flow regime map. Increases in axial flow rate suppressed the transition to Taylor-vortices.
DiPrima (1960)	Analytical.	Primary instability in laminar Taylor-Couette flow with axial flow. Inner and outer cylinders rotating in the same direction at different speeds.	Stability analysis using a symmetrical disturbance showed qualitative agreement with the transition measurements from laminar to laminar plus vortices flow of Kaye and Elgar (1958) for axial Reynolds numbers of 0 - 100. The critical Taylor number exhibited a parabolic dependence upon the axial Reynolds number.
Chandrasekhar (1962)	Analytical.	Primary instability in laminar Taylor-Couette flow with axial flow. Inner and outer cylinders rotating in the same direction at different speeds. The critical Taylor number dependence in the limit where the axial Reynolds number approaches zero.	The critical Taylor number T_c for the first transition from laminar to laminar plus vortices flow was expressed as a function of the axial Reynolds number R as $T_c = T_{co} + 26.5R^2$, where T_{co} is the critical Taylor number with no axial flow.
Snyder (1962)	Experimental.	Primary instability in laminar Taylor-Couette flow with axial flow. Inner cylinder rotating, outer cylinder at rest. Axial Reynolds number varied up to 100.	Good agreement obtained to DiPrima (1960) for axial Reynolds numbers less than 40. Above an axial Reynolds number of 40, discrepancies up to 15% were found.
Schwarz et al. (1964)	Experimental.	Primary instability in laminar Taylor-Couette flow with axial flow. Inner cylinder rotating, outer cylinder at rest. Effect of axial Reynolds number.	Three types of instabilities were found including an axi-symmetric mode, azimuthal mode and a non-symmetric mode due to interaction of the first two. Excellent agreement was found with the analytical results of Krueger and DiPrima (1964) for the axi-symmetric mode.

Table 2.6 continued.

Krueger and DiPrima (1964)	Analytical.	Primary instability in laminar Taylor-Couette flow with axial flow. Effect of counter-rotating inner and outer cylinders for axial Reynolds numbers less than 25.	The stability characteristics for counter-rotation were qualitatively similar to co-rotation. Relative agreement with experimental results was attained.
Coles (1965)	Experimental.	Transition in laminar Taylor-Couette flow, no axial flow. Effect of independently rotating inner and outer cylinders.	Detailed hot-wire measurements revealed complex transition patterns in Taylor-Couette flow after the first transition to Taylor vortices. Up to 70 transitions were found after the formation of Taylor vortices. 20 – 25 states defined by the number of Taylor vortices and superimposed traveling azimuthal waves were observed at a given rotation speed.
Hughes and Reid (1968)	Analytical.	Primary instability in laminar Taylor-Couette flow with axial flow. Inner and outer cylinders rotate in the same direction at different speeds. Application of the linear stability analysis for large axial Reynolds number.	Agreement with the experimental results of Kaye and Elgar (1958) obtained for axial Reynolds numbers less than 300. Above 300 the results are in disagreement. It is suggested that the non-axi-symmetric disturbances should be included to improve the analytical analysis.
Andereck et al. (1986)	Experimental.	Flow regimes in Taylor-Couette flow with no axial flow. Co-rotating and counter-rotating inner and outer cylinders.	A very detailed transition map illustrated many flow states and transitions also noted by Coles (1965).
Chang and Chen (2002)	Analytical.	Primary instability in laminar Taylor-Couette flow with axial flow. Co-rotation and counter-rotation of the inner and outer cylinders. Axial Reynolds number varied up to 100.	The discussion focuses on which modes are prominent depending on flow parameters. The disturbance was found to be non-axi-symmetric for sufficiently large axial Reynolds number as supposed by Hughes and Reid (1968).

Here, ω is the rotation frequency, r_m is the mean gap radius, δ is the gap height and U is the mean axial component of velocity. The criteria for transition from laminar to laminar plus vortices flow for axial Reynolds numbers less than 100 was considered analytically and experimentally in numerous cases (eg. Di Prima 1960, Chandrasekhar 1962, Snyder 1962, Krueger and DiPrima 1964, Schwarz et al. 1964). Becker and Kaye

(1962) examined the convective heat transfer in axial Taylor-Couette flow and also used the results to characterize the flow regimes. Hughes and Reid (1968) analytically examined the stability problem for axial Reynolds numbers up to 5000, however the analysis was in significant disagreement with existing data for axial Reynolds numbers above 300. More recent numerical investigations of stability in axial Taylor-Couette flow are given in Polkowski (1984), Crespo and Marques (1993), Meseguer and Marques (2000) and Chang and Chen (2002). The results from Becker and Kaye (1962) and others are shown in figure 2.7. It is important to note that the modified Taylor number used by Becker and Kaye (1962) is the square of that used by Kaye and Elgar (1958). For the anti-icing application, if engine oil lubricant were used as the working fluid, the Taylor number range for typical operating conditions is on the order of $2\times10^6 < Ta_m < 5\times10^7$, where the modified Taylor number here is the square of that defined by Kaye and Elgar (1958) following Becker and Kaye (1962). The modified Taylor number range indicates that the flow should be in the turbulent plus vortices regime.

The convection heat transfer in Taylor-Couette flows and axial Taylor-Couette flows have also been the subject of numerous investigations summarized in table 2.7 and reviewed in detail in Kreith (1968) and Maron and Cohen (1991). Gazely (1958) experimentally measured the heat transfer in axial Taylor-Couette flow for various types of slotted inner cylinders typical of electric motor stators in the laminar and laminar plus vortices regime. Becker and Kaye (1962) examined the heat transfer for axial Reynolds numbers up to 5960 and modified Taylor numbers from 10^3 to 2×10^6. The Nusselt number given by

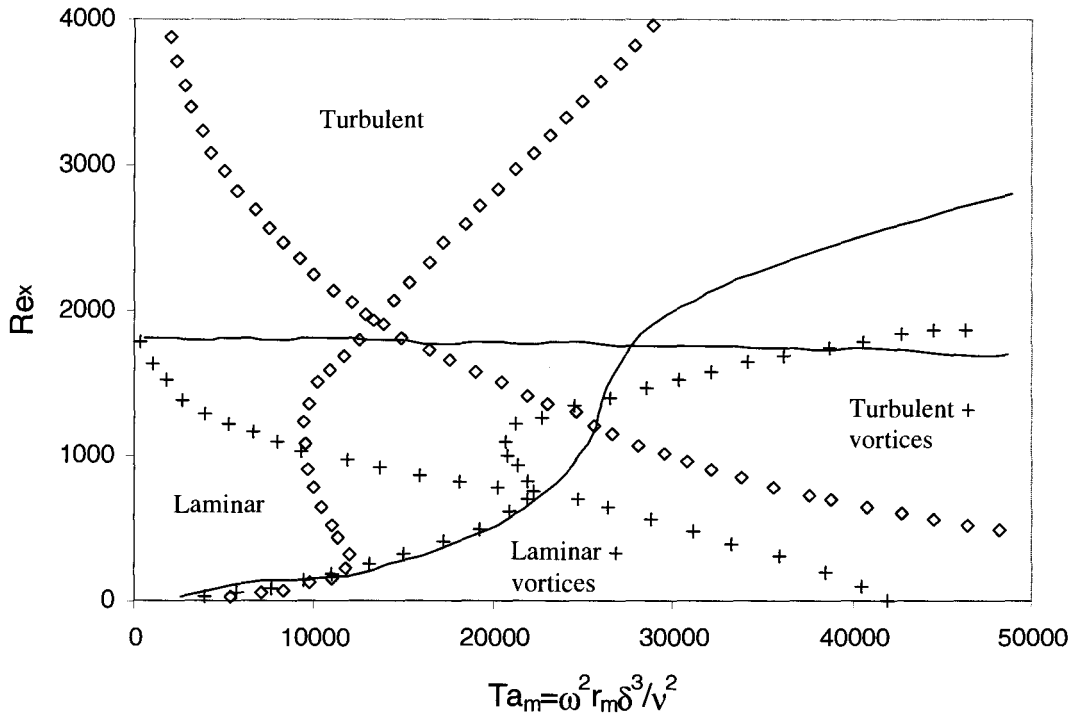

Figure 2.7: Flow regimes in axial Taylor-Couette flow; + Cornish (1933), — Becker and Kaye (1962), ◊ Astill (1964).

Table 2.7: Summary of investigations in convection heat transfer in Taylor-Couette flow with and without axial flow.

INVESTIGATORS	APPROACH	STUDY AREA	KEY FINDINGS
Gazely (1958)	Experimental.	Rotating inner cylinder and stationary outer cylinder with an imposed axial velocity. Various inner cylinder surfaces typical of those found in electric motors were used.	An effective Reynolds number based on the peripheral inner cylinder velocity and the axial flow velocity was used to characterize the data. The axial flow had a stabilizing effect similar to that found in the stability investigations. The slotted inner cylinder surface did not have an appreciable effect on the heat transfer.
Bjorklund and Kays (1959)	Experimental.	Co-rotating and counter-rotating inner and outer cylinders, no axial velocity. Gap height to inner cylinder diameter ratio varied from 0.054 – 0.128.	The heat transfer in the laminar and laminar plus vortices region was measured. The Taylor number was found to be a good correlating parameter for the heat transfer data rather than the Reynolds number. Effect of gap height was collapsed using the Taylor number.
Becker and Kaye (1962)	Experimental.	Rotating inner cylinder, stationary outer cylinder with axial flow. Heat transfer data characterized in the different flow regimes. Axial Reynolds number varied from 0 – 5960, Taylor number varied from 1×10^3 - 2×10^5.	Conduction heat transfer prevailed in the laminar regime until first critical Taylor number was reached where a sharp increased occurred in laminar plus vortices flow. Increasing the axial Reynolds number delayed the transition. A gradual increase in heat transfer from turbulent to turbulent plus vortices occurred. Heat transfer was independent of axial Reynolds number as the Taylor number increased. Transition from turbulent to turbulent plus vortices flow differed from Kaye and Elgar (1958).
Kuzay and Scott (1977)	Experimental.	Rotating inner cylinder, stationary outer cylinder with axial flow. Developing and fully developed turbulent flow characterized for axial Reynolds numbers of 1.5×10^4 – 6.5×10^4.	Temperature profiles in the axial and radial directions measured in the gap. The results were correlated using another parameter $\alpha \equiv \frac{2}{\pi}\frac{D_h}{D_i}\frac{V_T}{U_M}$, that was the "tightness" of the flow helix in the gap.

Table 2.7 continued.

Lee and Minkowycz (1989)	Experimental.	Rotating inner cylinder, stationary outer cylinder with axial flow. Heat transfer measured for Taylor numbers of 10^3 – 10^7 with axial Reynolds number of 50 – 1000. Slotted cylinders typical of electric motors and stators were used.	The presence of grooves on the inner cylinder increased the heat transfer significantly, contrary to that found by Gazely (1958). The heat transfer data became independent of axial Reynolds number with increasing Taylor number.
Arpaci and Kao (1997)	Analytical.	Independently rotating inner and outer cylinders with no axial flow in the laminar and turbulent regime.	Heat transfer, friction factor correlations proposed based on a turbulent micro-scale analysis. A new correlating parameter proposed given by $\pi_c = \frac{Ta\,\mathrm{Pr}^2}{1+\mathrm{Pr}}$. Heat transfer was found to have a $\mathrm{Pr}^{1/3}$ dependence for fluids with $0.7 < \mathrm{Pr} < 5$.
Jakoby et al. (1998)	Experimental.	Rotating inner cylinder, stationary outer cylinder with axial flow. Heat transfer measured for Taylor numbers of 10^5 – 10^9 and axial Reynolds numbers of 4000 – 30000.	The heat transfer was dominated by the inner cylinder rotation; the axial Reynolds number had an insignificant effect. An apparent stability boundary between steady and periodic flow in the turbulent plus vortices regime was identified.

$$Nu = \frac{2h\delta}{k}, \tag{2.26}$$

where h is the heat transfer coefficient and k is the thermal conductivity, had a constant value of 2 for purely laminar flow corresponding to pure conduction. There was a sharp increase in the Nusselt number at the transition from laminar to laminar plus vortices flow. An increase in the axial Reynolds number delayed this transition and decreased the Nusselt number. For low Taylor numbers and turbulent axial flow, the heat transfer was initially constant, with a modest increase in the heat transfer during the transition to turbulent plus vortices flow. As the Taylor number increased, the heat transfer seemed to become relatively independent of the axial Reynolds number. The heat transfer for Taylor-Couette flow in the turbulent regime was also considered experimentally in Kuzay

and Scott (1977) and Pfitzer and Beer (1992). Lee and Minkowycz (1989) obtained mass transfer measurements using the Naphthalene sublimation technique in turbulent and turbulent plus vortices flow for combinations of smooth and slotted inner and outer cylinders typical of electric motors. A slight increase in mass transfer was noted with the slotted inner cylinder. Jakoby et al. (1998) measured turbulent convection heat transfer for axial Reynolds numbers of 4000 – 30000 and Taylor numbers up to 10^9. The results showed that the heat transfer was dominated by the inner cylinder rotation speed or the Taylor number, and essentially independent of the axial Reynolds number. This was also evident in the data of Lee and Minkowycz (1989). Experimental heat transfer data from some of the sources discussed here is compared in figure 2.8 over a wide range of Taylor number and axial Reynolds numbers within the current application range.

The heat transfer investigations typically used water or air as the working fluids that had Prandtl numbers that were of order 1. In many turbulent flows, such as boundary layers, pipe and duct flows the Nusselt number depends on $\mathrm{Pr}^{1/3}$ (eg. Incopera and DeWitt 1996, Dong et al. 2002, Mitrovic et al. 2004). There are only a few investigations available that examine the effect of Prandtl number on the heat transfer in Taylor-Couette flow. Arpaci and Kao (1997) considered the existing experimental heat transfer data for air, water and methanol, $(0.7 < \mathrm{Pr} < 5)$, and proposed that it could be correlated by

$$Nu = 0.046(Ta\,\mathrm{Pr})^{1/3}. \tag{2.27}$$

Torii and Yang (1998) numerically examined the effect of the Prandtl number on the heat transfer in axial Taylor-Couette flow for an axial Reynolds number of 10000 and Taylor numbers on the order of 10^7 - 10^8. The results indicated a Prandtl number dependence of

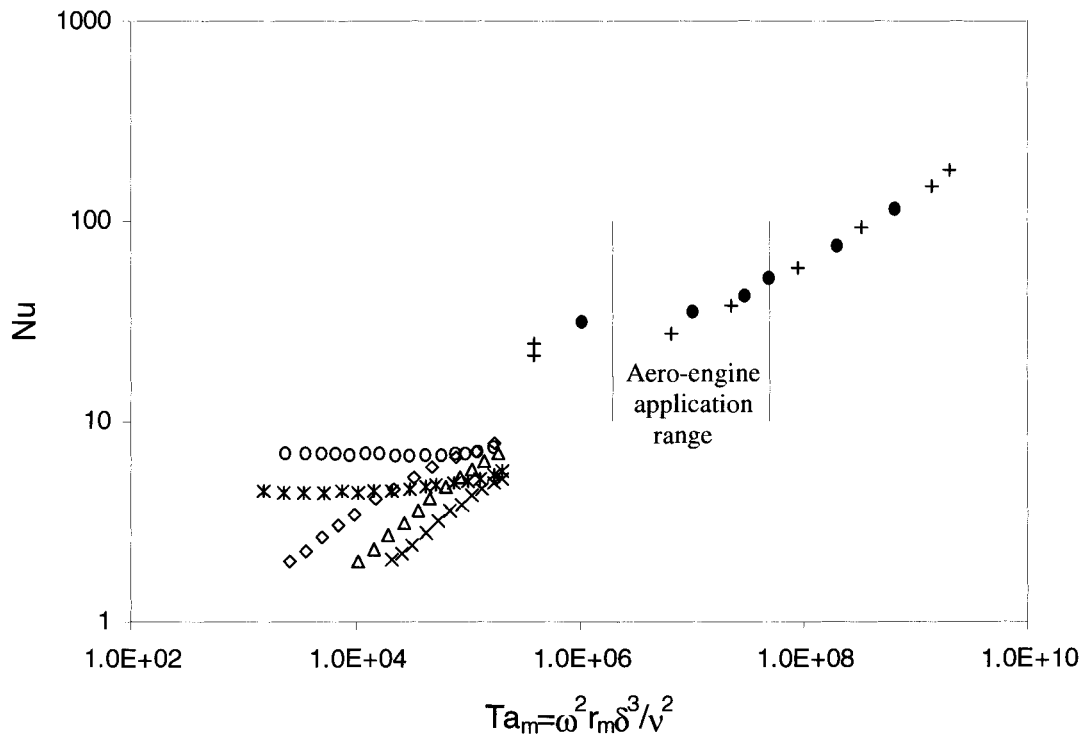

Figure 2.8: Experimental heat transfer results in axial Taylor-Couette flow. Data of Becker and Kaye (1962) for Re_x of ◊ 53, Δ 222, × 1592, * 3740, o 5960 and Jakoby et al. (1998) for Re_x of + 4000, • 12000.

$Nu \sim \mathrm{Pr}^{0.45}$ for $0.001 < \mathrm{Pr} < 100$; significantly larger than that found by Arpaci and Kao (1997). Thus, the Prandtl number dependence is not yet clear.

2.7 Heat Transfer Augmentation Techniques

The convection heat transfer in many systems including the rotating heat pipe evaporator in this investigation can be enhanced using passive techniques such as surface roughness. Some of the investigations for axial Taylor-Couette flow considered the heat transfer for cylinders with slots, but there does not appear to have been any systematic investigations to examine the effect of surface roughness on the heat transfer in this system. The use of passive heat transfer augmentation for many types of heat exchangers and applications have been studied in detail and are reviewed in detail in Webb (1971), Kalinin and Dreitser (1998) and Ligrani et al. (2003). Migai (1980) showed that approximately 65% of the thermal resistance in a turbulent boundary layer for $\mathrm{Re} = 10^4$ is contained within the wall layers composed of viscous sub-layer $(y+ < 5)$ and the transition layer $(5 < y+ < 60)$. Thus, the use of artificial turbulization is recommended primarily in these wall layers (Kalinin and Dreitser, 1998). Indeed, Sutherland (1967) found the convection heat transfer increased for wall turbulization with heights up to $y+ < 40$. For larger heights, the friction factor continued to increase while the heat transfer remained constant. Some common types of two-dimensional roughness include square, pyramid, cylindrical, and hemispherical ribs, (Webb et al, 1971) that are typically oriented perpendicular to the oncoming flow or at angles of 45° or 60° to the oncoming

flow (Ligrani et al. 2003). Common types of three-dimensional extended surfaces include arrays of wall-mounted cubes, pyramids and cylinders, (Chyu and Natarajan 1996) or dimple in the surface (Ligrani et al. 2003). Delta winglets are also commonly used as vortex generators (Jacobi and Shah 1995).

The flow patterns that develop over square ribs for various streamwise spacing are shown in figure 2.9. For small spacing, a re-circulating flow is confined to the cavity between the ribs. For larger spacing, the shear layer that separates from the top of the rib reattaches to the wall at an intermediate position before the adjacent rib. Mueller (1961) found the attachment length was 6 – 8 rib heights. Lin et al. (1966) reported that the size of the re-circulation zones and the attachment length (if present) were insensitive to the Reynolds number. Okamoto et al. (1993) found that the turbulence intensity and local heat transfer coefficient between the ribs increased in the streamwise direction and attained a maximum just after the shear layer attached. The turbulence intensity at the attachment point attained a maximum for a streamwise spacing to rib height of approximately 9. In a wide range of geometries, it is generally found that the heat transfer and friction factor are maximized for a pitch to rib height spacing of 10 (Edwards and Sheriff 1961, Han et al. 1978, Kalinin and Dreitser 1998). The rib height to hydraulic diameter of the channel or duct is typically 0.01 to 0.05.

The use of three-dimensional extended surfaces or protruding elements is also commonly used to enhance convection heat transfer. Hunt et al. (1978) examined the flow around various obstacles such as cubes, cuboids and obstructions with a hole using streak patterns produced by a thin layer of oil containing suspended particles laden on the

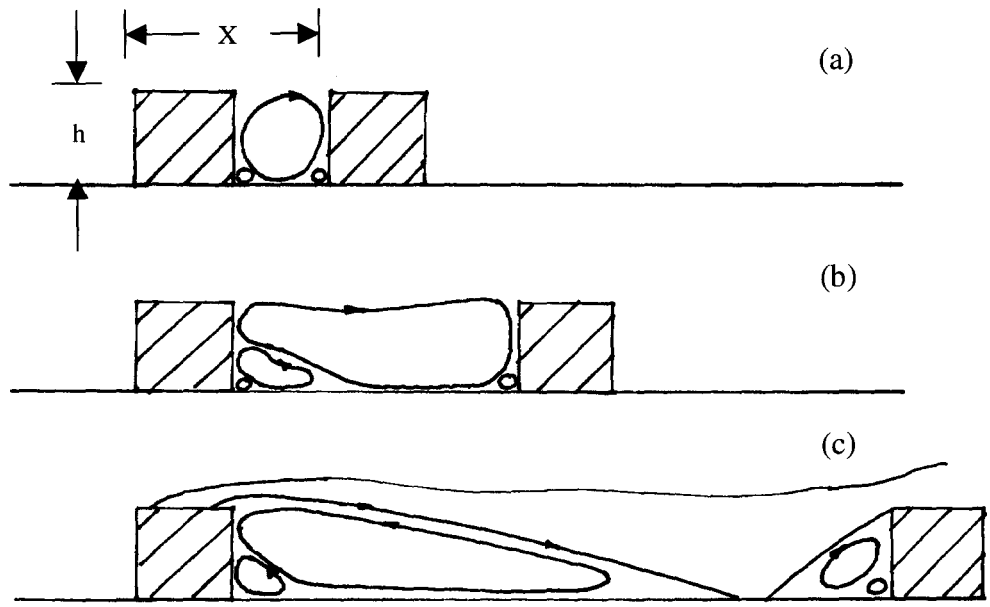

Figure 2.9: Schematic of the flow structures formed between square ribs at different streamwise spacing, (a) X/h=2, (b) X/h=4, (c) X/h=8 from Kalinin and Dreitser (1998).

object. The basic features of the flow around a cube in a turbulent boundary layer are shown in figure 2.10. This pattern is also typical of the flow around other three-dimensional obstructions as discussed in Chyu and Natarajan (1996). The flow around the object has a primary vortex formed by the adverse pressure gradient in the front that wraps around the sides of the obstacle. An intense secondary vortex formed under the primary vortex near the base of the object contributes significantly to the heat transfer. On the backside, an upside down "U" shaped horseshoe vortex forms that Chyu and Natarajan (1991) proposed was formed from the separated shear layer on the leading face and the two counter-rotating horseshoe vortices wrapped around the sides. Garimella and Eibeck (1990) experimentally investigated the convective heat transfer for an array of inline and staggered rectangular protruding elements on a heated base plate with different heights relative to the channel, the streamwise and spanwise spacing, and the Reynolds number. The flow tends to migrate to the gap over the elements so the mean velocities between the elements decreased with increasing Reynolds number. The average heat transfer produced by the array increased by 35% to 40% as the streamwise spacing increased from 2 to 6 element heights and no maximum was encountered for this range of spacing. The average heat transfer produced by the array increased by 15% as the spanwise spacing between the elements was increased from 0.5 to 2.2 times the height. The heat transfer seemed to be constant for spacing up to 6 element heights indicating the result is less sensitive to the spanwise spacing. Flow visualization showed that for small spacing a re-circulating flow region formed between the adjacent elements preventing

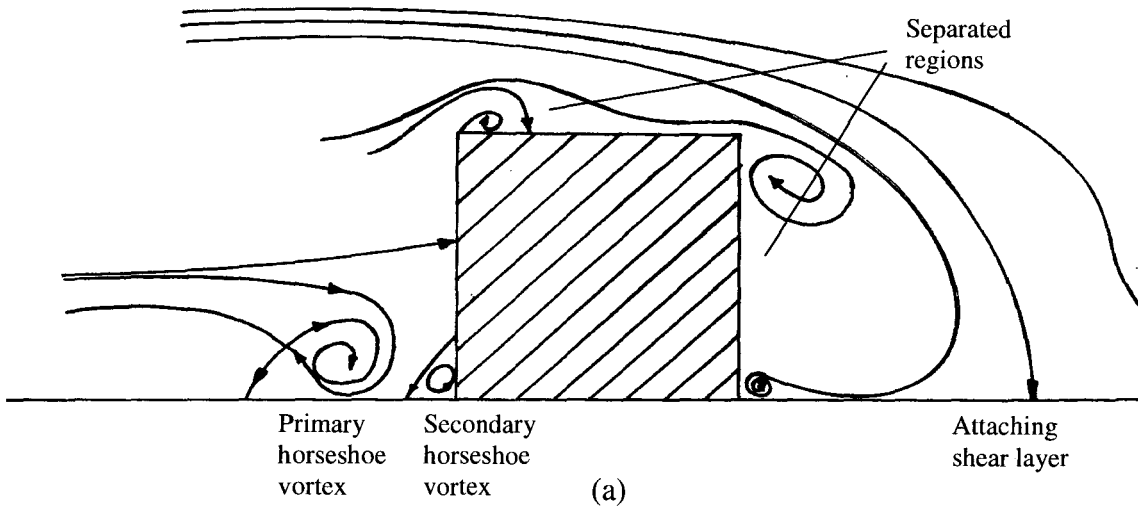

(a)

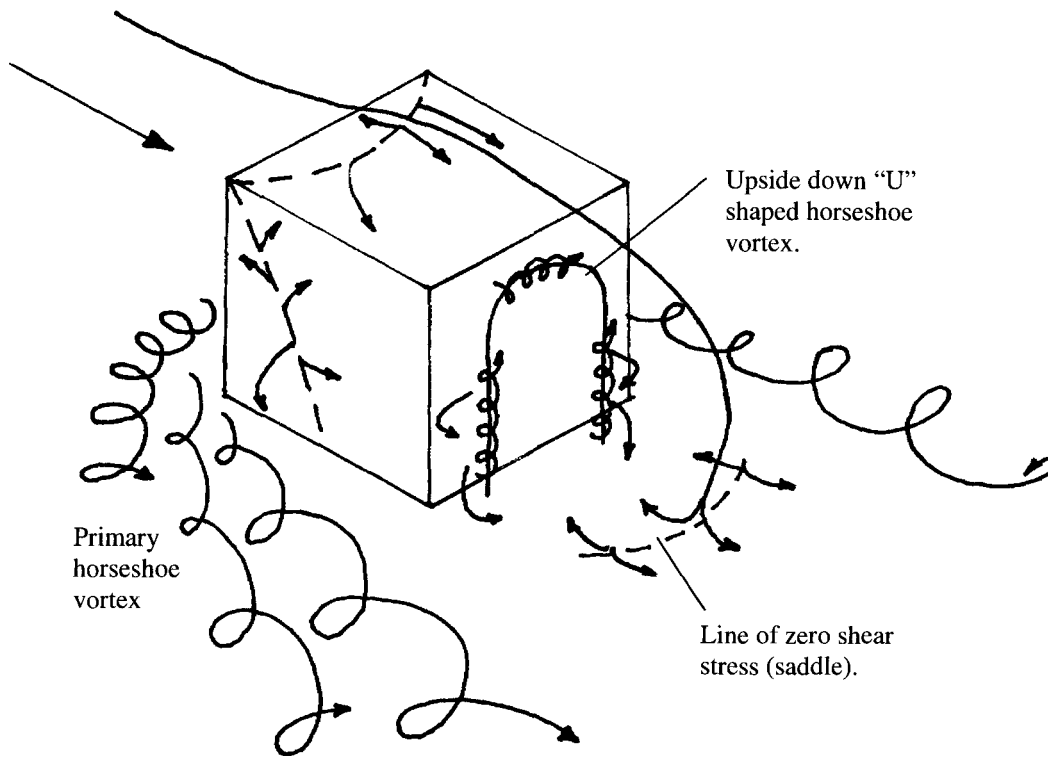

(b)

Figure 2.10: Schematic of the flow structures formed over a wall-mounted cube in a turbulent boundary layer; (a) profile view, (b) rear isometric view from Hunt et al. (1978).

efficient mixing with the mean flow. Staggering the array increased the heat transfer by 40% at the lowest channel height and 7% at the largest.

Heat transfer enhancement using three-dimensional extended surfaces is widely used for cooling turbine blades. In this application, arrays of tall slender cylindrical pins referred to as "pin fin arrays" are normally used in the interior blade cavities, though dimples, ribs and swirl chambers are also common (Ligrani et al. 2003). The pin array is the most common and the pins typically span the entire height of the cavity to also provide structural integrity. Pin fin arrays represent a large sub-set of three-dimensional heat transfer augmentation and a summary of investigations is given in table 2.8. Sparrow and Ramsey (1978) found that the average heat transfer for the pin array decreases as tip clearance above the pins is increased largely due to the flow passing over the pins. In contrast to the rectangular modules, the recommended spacing for the pin fin array seems to be 2.5 pin diameters in both the spanwise and streamwise direction, (Jubran et al.1993, Chyu et al. 1996, Chyu et al. 1998). Jubran et al. (1993) found that staggering the array increased the array average heat transfer by 16%.

Finally, in the anti-icing system design considered here, the condenser section of the rotating heat pipe was encased in a filler material that provided a heat transfer conduit directly to the nose cone. In this case, a low-density, high conductivity filler would be desirable and many materials are available that have these properties. For example, metal matrix foams, carbon fiber composites and polycrystalline graphite have been increasingly used in thermal management applications (Pedraza and Klemens 1993, Chung 1994, Ting et al. 1995). The highly anisotropic thermal conductivity of these

Table 2.8: Investigations of the heat transfer in pin fin arrays.

INVESTIGATORS	GEOMETRY	OBJECTIVE	TECHNIQUE	KEY RESULTS
Sparrow and Ramsey (1978)	Cylindrical, Staggered, h/D=1,2,3 h/H=0.29,0.58, 0.875 S/D=3 X/D=2.6 Re=5000-35000.	Per row heat transfer. Effect of tip clearance.	Naphthalene sublimation.	Monotonic increase in heat transfer over first 3 rows. Local maximum occurs at row 4. Heat transfer constant for remaining rows. The heat transfer increases with Reynolds number; row 4 maximum is larger at higher Reynolds numbers. The heat transfer increases with decreasing tip clearance because flow is forced through the array. Larger clearance allows flow over the pins and reduces mean velocities and heat transfer in the array.
Metzger et al. (1982)	Cylindrical, Staggered, h/D=1 h/H=1 S/D=2.5 X/D=1.5,2.5 Re=1000-100000.	Per row heat transfer. Effect of streamwise spacing.	Wind tunnel, heated base plate and pins.	Heat transfer increased over first 3-5 rows decreased by 12% over remaining rows. This differed from the results of Sparrow and Ramsey (1978).
Metzger et al. (1984)	Cylindrical & oblong, Inline/staggered, h/D=1 h/H=1 S/D=2.5 X/D=1.5,2.5 Re=1000-100000.	Effect of array orientation on circular pins. Effect of oblong shape.	Wind tunnel, heated base plate and pins.	Heat transfer increased by 9% as circular staggered pin array was rotated 60°; 18% increase in pressure drop. The oblong shape increased heat transfer by 20% with a 100% increase in pressure drop.
Jubran et al. (1993)	Cylindrical, Inline/staggered, h/D=9.45 h/H=0.5, 0.66, 1 S/D=1.25-11.27 X/D=2.44-19.53 Re=7500-32000.	Optimization of streamwise, spanwise spacing for various clearance ratios.	Wind tunnel, heated base plate and pins.	The optimum spacing was S/D=X/D=2.5 regardless of clearance, channel height or Reynolds number. Staggering the array increased the heat transfer by 16% compared to the inline arrangement.

Table 2.8 continued.

Tahat et al. (1994)	Cylindrical, Inline/staggered, h/D=9.45 h/H=not given. S/D=1.5-11.96 X/D=1.16-13.85 Re=2000-8000.	Optimization of streamwise, spanwise spacing.	Wind tunnel, heated base plate and pins.	Optimum spacing was S/D=1.47 and X/D=2.2 for both staggered and inline arrays.
Maudgal and Sunderland (1996)	Cylindrical, Staggered, h/D=6,12 h/H=0.6,1 S/D=1.3,1.7,2.6 X/D=1.3,1.7,2.6 Re=2500-5100. θ=0,30°,45°,60°,90°.	Effect of angle of impingement of the incoming flow; 90° has the flow parallel to the base plate.	Wind tunnel, heated base plate and pins.	For h/H=0.6, 40%-90% of the flow migrated to the clearance region. The heat transfer was 50% less than with no clearance.
Chyu et al. (1998)	Cylindrical, Inline/staggered, h/D=1 h/H=1 S/D=2.5 X/D=2.5 Re=5000-25000.	Relative contributions of pin and end wall to array heat transfer.	Naphthalene sublimation.	The heat transfer coefficient on the pins up to 20% higher than the end wall. It was claimed that the Naphthalene sublimation technique produced more accurate results and uniform boundary conditions.

Note: h – pin height d-pin diameter H–channel height S-spanwise spacing X-streamwise spacing.

materials was thought to be advantageous in this particular application because it could be used to force heat to be conducted primarily in the radial direction resulting in more uniform heat transfer to the nose cone. Ting et al. (1995) manufactured various carbon fiber mats using the vapour grown carbon fiber technique (VGCF) with a substrate. The room temperature thermal conductivity parallel to the fibers was 300 W/mK to 1600 W/mK for fiber volume fractions of 10% to 100%, while the thermal conductivity of the mat perpendicular to the fibers was 30 W/mK to 80 W/mK. The typical density of the

material was 1000 kg/m^3 to 2000 kg/m^3 over the volume fraction range and clearly a significant advantage is gained with respect to the weight when compared to copper or aluminum that have a density of 8933 kg/m^3 and 2702 kg/m^3 respectively.

Chapter 3 System Modeling

The anti-icing system proposed here was modeled using a number of different domains shown schematically in figure 3.1. Each domain embodied a heat transfer processes, component or region in the system. In the evaporator, three domains consisting of the spiral Taylor Couette flow in the gap around the heat pipe, the heat pipe wall and the film on the inside of the heat pipe were modeled separately and then coupled together. In the condenser, the film condensation on the end wall and tapered wall of the heat pipe were modeled individually and then coupled with the respective wall temperature boundary conditions. The conduction along the annular tapered wall was modeled separately. The hydraulic and heat transfer characteristics of the flow in the heating channels was modeled as a separate domain and coupled to the film condensation rate by the pool height and the temperature of the nose cone shell. The nose cone was divided into three domains consisting of the end wall, a small junction region and the nose cone shell. The filler material was also modeled separately. Finally, the atmospheric conditions and the flow over the nose cone were used to determine the heat transfer from the nose cone. The heat transfer rate in the evaporator and condenser were then coupled through the vapour temperature in the rotating heat pipe. The thermal resistance of the vapour flow was neglected assuming that it did not impose a significant thermal resistance following Daniels and Al-Jumaily (1975) and Song et al. (2003b).

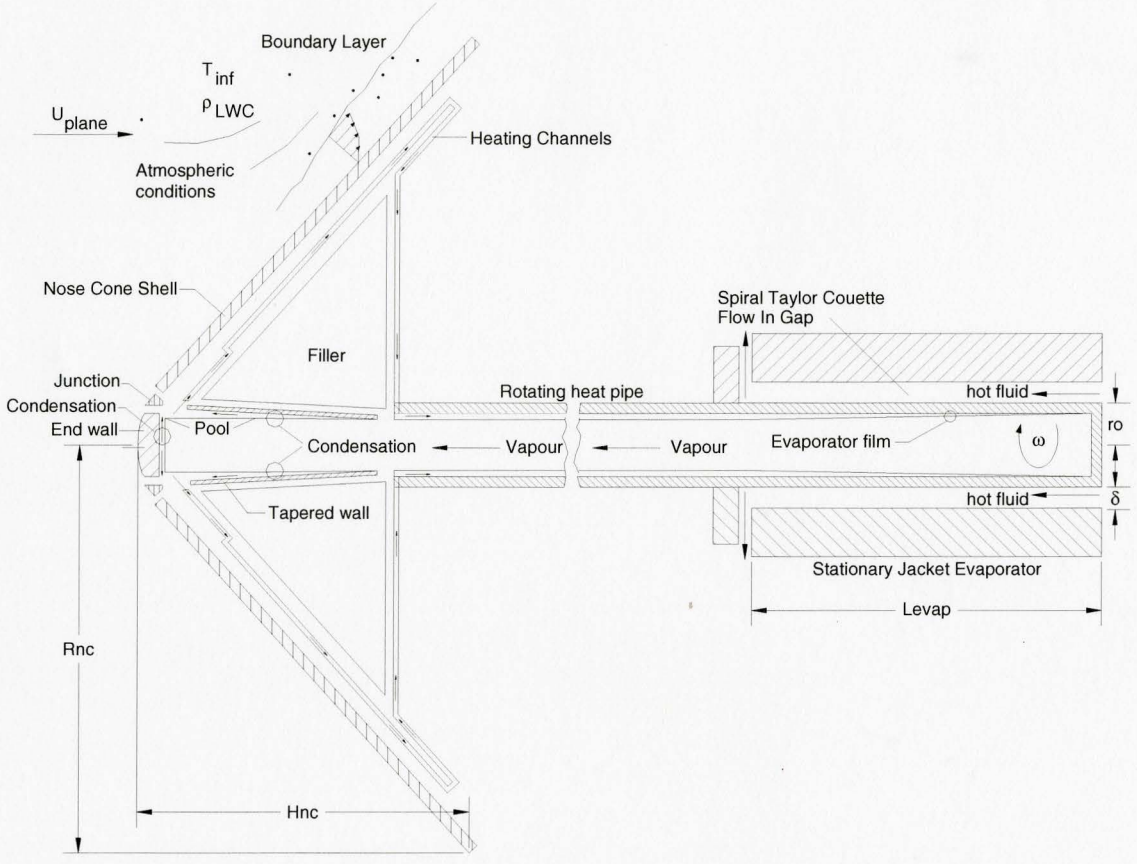

Figure 3.1: Schematic of the domains used to model the anti-icing system (exploded view).

3.1 Problem Definition

The typical range of the important parameters in the proposed anti-icing system is summarized in table 3.1. The engine rotation speed of a small turbo-fan engine is typically 5000 rpm to 20000 rpm. The engine speed when the plane often experiences icing conditions while ascending is typically 10000 rpm to 20000 rpm. The engine speed when the plane typically experiences icing conditions during decent is 5000 rpm to 7000 rpm. Aircraft using this type of turbofan usually have airspeeds ranging from 300 km/h to 600 km/h.

The icing conditions that the airplane may experience during flight depend on the altitude and the air temperature. The continuous icing spectrum defined in FAR 25 appendix C (Cebeci and Kafyeke, 2003), was used to characterize the typical ambient air temperature range and corresponding liquid water content. It was assumed that the droplets had a mean effective diameter of 15 microns. This resulted in the highest liquid water content at a given temperature within the continuous icing spectrum. The maximum liquid water content was 0.7 g/m^3 to 0.2 g/m^3 for ambient temperatures of -5°C to -30°C.

Two working fluids, air or engine lubricant, were considered for use in the evaporator. In this case, the engine lubricant (MIL-L-23699) was used as the working fluid and its properties are given in table 3.2. The engine lubricant could be heated by the engine to a minimum of 100°C and a maximum of 200°C. A rotating heat pipe with a maximum diameter of 25.4 mm (1 in.) could fit in the central fan shaft of the engine resulting in a maximum gap height in the evaporator of 2.54 mm (0.1 in.). The modified

Table 3.1: Typical ranges for important parameters in the anti-icing system.

DESCRIPTION	SYMBOL	RANGE OR VALUE	
SPEEDS			
Engine speed	ω	Cruise/decent: 5000 rpm to 7000 rpm Climb: 10000 rpm to 20000 rpm	
Airplane speed	U_{plane}	300 km/h – 600 km/h	
ATMOSPHERIC CONDITIONS			
Ambient temperature	T_{inf}	-5°C to -30°C	
Liquid water content	ρ_{LWC}	0.7 g/m^3 to 0.2 g/m^3	
EVAPORATOR			
Fluid from engine		MIL-L-23699 lubricant or air	
Evaporator fluid temperature	$T_{hot\,fluid}$	100°C minimum	
Gap height	δ	2.54 mm (0.1 in.)	
Modified Taylor number	Ta_m	10^6 - 10^8	
Axial Reynolds number	Re_x	1000 minimum	
Length	L_{evap}	101.6 mm (4 in.)	
ROTATING HEAT PIPE			
Outer radius	r_o	12.7 mm (0.5 in.)	
Inner radius	r_i	9.53 mm (0.375 in.)	
Heat pipe conductivity	k_{hp}	400 W/mK	
CONDENSER			
Taper angle	α	1° - 7°	
Tapered wall conductivity	k_{fin}	160 W/mK	
Filler conductivity	k_{filler}	400 W/mK	
NOSE CONE			
Height of nose cone	H_{nc}	Approx. 100 mm (4 in.)	
Radius of nose cone	R_{nc}	Approx. 115 mm (4.5 in.)	
Effective Reynolds number of flow over nose cone	Re^*	0 – 3.5×10^6	
Nose cone conductivity	k_{nc}	160 W/mK	
Nose cone thickness	t_{nc}	Shell ~ 3.18 mm (0.125 in.) Pole ~ 6.35 mm (0.25 in.)	
WORKING FLUID			
PROPERTY (30°C - 60°C)	SYMBOL	WATER	ETHANOL
Operating range (freeze, boil)	-	0°C to 100°C	-112°C to 78°C
Thermal conductivity (W/mK)	k	0.62 - 0.66	~ 0.17
Specific heat (J/kgK)	C_p	4178 – 4186	595 – 665
Latent heat (J/kg)	h_{fg}	2426 – 2345	889 – 989
Prandtl number	Pr	5.2 – 2.9	3.36 – 2.29
Density (kg/m^3)	ρ	~ 1000	~ 780
Absolute viscosity (Ns/m^2)	μ	7.69- 4.53	10.2 – 5.9

Table 3.2: Properties of engine oil lubricant MIL-L-23699.

TEMPERATURE T °C	DENSITY ρ (kg/m^3)	VISCOSITY μ (Ns/m^2) $\times 10^3$	THERMAL CONDUCTIVITY k (W/mK)	SPECIFIC HEAT C_p (J/kgK)	PRANDTL NUMBER Pr
21.1	987.6	46.6	0.14	1784	613.2
82.2	941.9	6.6	0.13	2068	105.7
87.8	938.3	5.8	0.13	2111	95.5
93.3	934.2	5.1	0.13	2138	85.6
98.9	930.0	4.7	0.13	2162	79.2
104.4	925.9	4.2	0.13	2191	71.8
121.1	914.0	3.1	0.12	2263	56.3
148.9	894.0	2.1	0.12	2395	41.4
176.7	873.6	1.6	0.12	2523	33.0
204.4	853.9	1.2	0.12	2650	28.4

Taylor number range for a nominal engine lubricant temperature of 100°C, is 10^6 to 10^8 following the definition in Becker and Kaye (1962). A nominal axial Reynolds number of 1000 was thought to be characteristic of the through-flow in the gap. The nominal length of the evaporator for this application was 102 mm (4 in.) following Song et al. (2003a,b).

The thermal conductivities of the components in the proposed system are also given in table 3.1. The rotating heat pipe used here was a copper wall heat pipe although in the practical application it may be necessary to use stainless steel. In the condenser, the tapered wall of the heat pipe was given the properties of aluminum so that it was similar to the nose cone that seems to be standard in existing nose cone designs although Nickel alloys have also been used. The range of taper angles of the condenser investigated here ranged from 1° to 7°, typical of practical rotating heat pipes. A polycrystalline graphite or similar composite was used as the filler material and given a thermal conductivity of 400 W/mK, a nominal value for this type of material.

The basic geometry of the nose cone for the turbo fan engine considered here has a base diameter of about 200 mm and a height of about 115 mm and a total taper angle of 84°. Following Axcell and Thainpong (2001), the effective Reynolds number for the flow over the nose cone is on the order of 3.5×10^6 resulting in a turbulent boundary layer.

The properties of water and ethanol considered as possible working fluids in the rotating heat pipe are also summarized in table 3.1. The thermal conductivity, specific and latent heat of ethanol are only 20% - 30% of that for water. Despite this, ethanol would be better for lower temperature applications such as this one because it would not freeze, thus avoiding complications during the startup of the anti-icing system that may occur with water.

3.2 The Aero-engine Nose Cone Condenser

The performance of the condenser section was modeled by considering the condensation of the vapour on the tapered extended fin and the end-wall of the rotating heat pipe. The heat transfer from this process was transferred into the nose cone or the filler material. The condensate films are shown schematically in figure 3.2. The condensation on these surfaces is subject to non-uniform temperature boundary conditions at the wall and the component of centrifugal acceleration tangent to the wall that drives the liquid into the pool region. Following Daniels and Al-Jumaily (1975), the condensation on the extended fin is modeled assuming that it is film condensation. In this case, the leading order momentum and energy equations for the film are given by

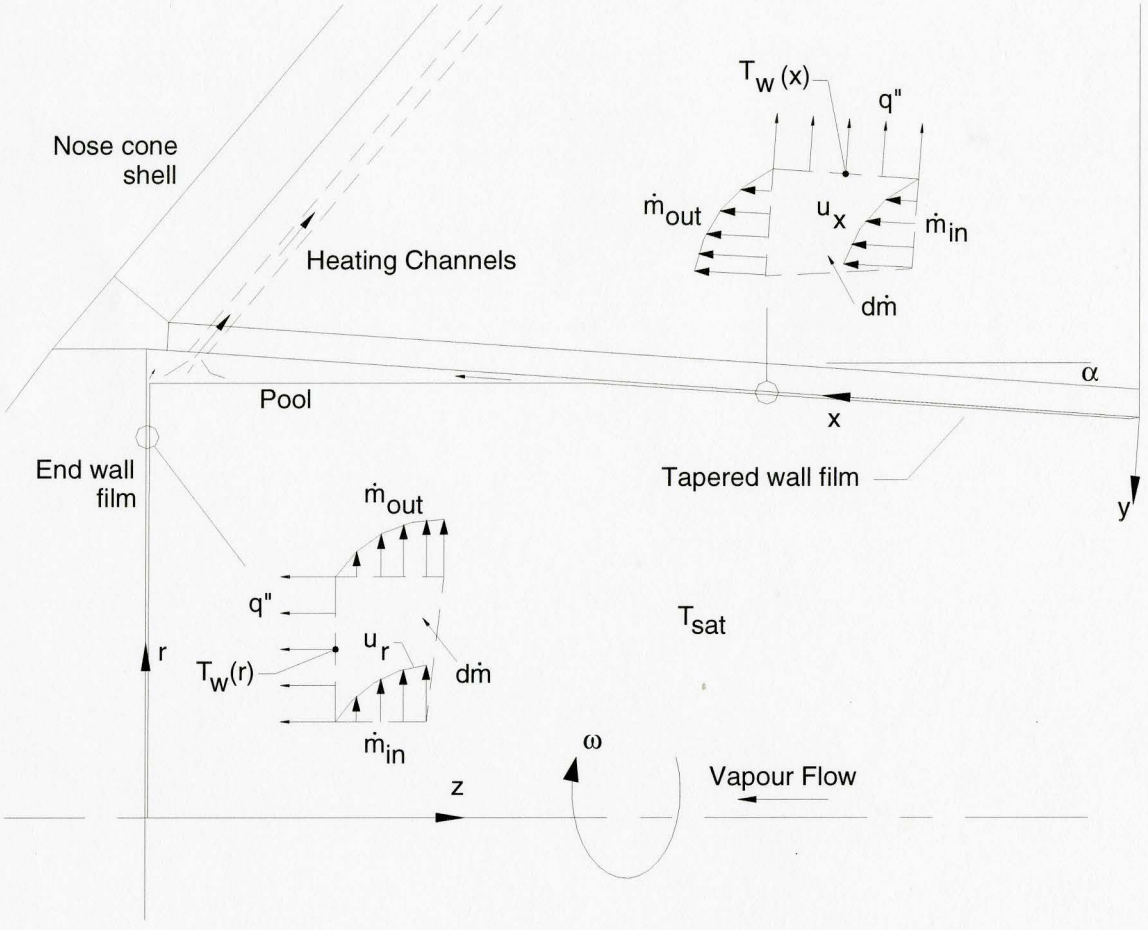

Figure 3.2: Schematic of the liquid films in the condenser.

$$\rho\omega^2 r\sin\alpha - \frac{\partial P}{\partial x} + \mu\frac{\partial^2 u_x}{\partial y^2} = 0, \tag{3.1}$$

$$\rho\omega^2 r\cos\alpha + \frac{\partial P}{\partial y} = 0, \tag{3.2}$$

$$k\frac{\partial^2 T}{\partial y^2} = 0. \tag{3.3}$$

where ρ, μ and k are the density, absolute viscosity and thermal conductivity of the condensate evaluated at the film temperature, ω is the rotation frequency, r is the radius, α is the taper angle of the wall, P is the absolute pressure, u_x is the velocity of the condensate parallel to the wall and T is the temperature. The boundary conditions at the wall at $y = 0$ are given by

$$u_x = 0 \tag{3.4}$$

and

$$T = T_w(x), \tag{3.5}$$

where $T_w(x)$ is the local wall temperature. The boundary conditions at the free surface of the film at $y = \delta$, are given by

$$\tau = \mu\frac{\partial u_x}{\partial y} = 0 \tag{3.6}$$

and

$$T = T_{sat}. \tag{3.7}$$

The magnitude of the vapour shear stress and the momentum drag relative to the driving force in the liquid film as well as the flow regime of the film were estimated in appendix

A. The results showed that the vapour shear stress was negligible for both water and ethanol for typical heat transfer rates in this application. The momentum drag was found to be of similar order to the driving force in the liquid film (on the order of 0.1 – 1.0) for both fluids. The effect of the momentum drag would accelerate and thin the film on the tapered wall since the liquid and vapour are co-flowing and this would increase the heat transfer. Including the momentum drag would be more accurate but it was neglected here to obtain a first order, conservative estimate of the heat transfer. The analysis also showed that the film is laminar and in solid body rotation if it is a film. Solving the momentum equations yields the velocity profile of the film given by

$$u_x = \left(\frac{\omega^2 R}{\nu}\right)\left(\sin\alpha - \cos\alpha\frac{d\delta}{dx}\right)\left(\delta y - \frac{y^2}{2}\right). \tag{3.8}$$

Following Daniels and Al-Jumaily (1975), it was assumed that $d\delta/dx << \tan\alpha$ so that the pressure gradient due to the change in film thickness is small. Neglecting higher order terms in the integration, the film thickness is given by

$$\delta_{fin,film} = \left(\frac{3\nu\dot{m}_{fin,film}}{2\pi\rho\omega^2 R^2 \sin\alpha}\right)^{1/3}, \tag{3.9}$$

where $\dot{m}_{fin,film}$ is the local mass flow rate of the condensate and R is the local radius of the wall. Integrating the energy equation across the film yields a linear temperature distribution. Thus, to first order, the heat flux across the film is given by

$$q''_{w,fin,film} = \frac{(T_{sat} - T_w)}{\frac{R}{k}\ln\left(\frac{R}{R-\delta}\right)}. \tag{3.10}$$

The condensation on the end of the heat pipe was modeled following the approach outlined in Sparrow and Gregg (1959b) for condensation to a rotating disk. Following Sparrow and Gregg (1960), the effect of the vapour shear stress and momentum drag were neglected and thin film approximations were used. The radial momentum equation in the rotating frame and the energy equation for the film are given by

$$\rho\omega^2 r + \mu\frac{\partial^2 u_r}{\partial r^2} = 0, \tag{3.11}$$

and

$$k\frac{\partial^2 T}{\partial z^2} = 0. \tag{3.12}$$

The boundary conditions along the wall at $z = 0$ are given by

$$u_r = 0 \tag{3.13}$$

and

$$T = T_w(r), \tag{3.14}$$

while the boundary conditions at the free surface of the film at $z = \delta$ are given by

$$\mu\frac{\partial u_r}{\partial z} = 0 \tag{3.15}$$

and

$$T = T_{sat}. \tag{3.16}$$

Solving the momentum equation yields the radial velocity profile given by

$$u_r = \frac{\omega^2 r}{\nu}\left(\delta z - \frac{z^2}{2}\right). \tag{3.17}$$

Integrating and rearranging, it follows that the film thickness is given by

$$\delta_{nc,film} = \left(\frac{3\nu \dot{m}_{nc,film}}{2\pi\rho\omega^2 r^2} \right)^{1/3}. \tag{3.18}$$

where $\dot{m}_{nc,film}$ is the local mass flow rate of the film. Integrating the energy equation across the film yields a linear temperature distribution to first order when the effect of convection is negligible. Thus the heat flux across the film is given by

$$q''_{w,nc,film} = \frac{k}{\delta}(T_{sat} - T_w). \tag{3.19}$$

Since the effect of convection was neglected, the energy released during the condensation process must balance the heat conducted across the film into the wall. Hence, the local mass condensation rate is given by

$$\frac{d\dot{m}}{dA} = \frac{q''}{h_{fg}}. \tag{3.20}$$

where dA is the differential area of the wall. In both cases, the condensate film thickness was determined using a shooting method that was iterated until the boundary conditions converged. It is important to note that the film thickness at the leading edge of the extended fin film may or may not be zero depending on the fin geometry and thermal conditions. For example, for shallow taper angles the centrifugal component parallel to the wall may not be sufficient to drive all of the condensate towards the pool. In this case, a portion of the condensed fluid could flow back over the end of the fin. This would be undesirable because the film thickness in the condenser would be larger than necessary and could be reduced by increasing the taper angle. Essentially, the condenser would be operating off-design and would have less than optimal performance. Moreover, the flow rate in the heating channels would be smaller thereby reducing the additional

heat transfer to the nose cone shell. In all cases considered here, the film thickness at the leading edge was assumed to be zero and was then solved up to the edge of the pool. The pool height was determined by solving for the flow rate through the channels. This would vary with height and thus balance the condensation mass flow rate with that in the channels. It was found in all cases that the pool height was sufficiently small so that it never exceeded the end of the fin.

The flow through the heating channels shown in figure 3.3, was modeled using the mechanical energy equation given by

$$\frac{\omega^2}{2}\left(R_{co}^2 - R_{pool}^2\right) - \left(\frac{P_{co} - P_{sat}}{\rho}\right) - \left(\frac{u^2}{2}\right) - h_l = 0, \tag{3.21}$$

where R_{pool} is the radius of the pool free surface and R_{co} is the radius of the channel outlet, ω is the rotation speed of the engine and u is the velocity of the flow in the channel. The first term represents the work done on the fluid from the centrifugal force due to the difference in the radius of the pool surface and the channel outlet. The second term accounts for the pressure difference between the pool free surface and the channel outlet. The condensate would discharge horizontally along the inside heat pipe wall at the channel outlet. It was assumed that the film thickness at the outlet was approximately equal to the height of the channel, so the nominal outlet pressure at the channel center was estimated by

$$P_{co} \approx \frac{\rho\omega^2 R_{co} h_c}{2} + P_{sat}. \tag{3.22}$$

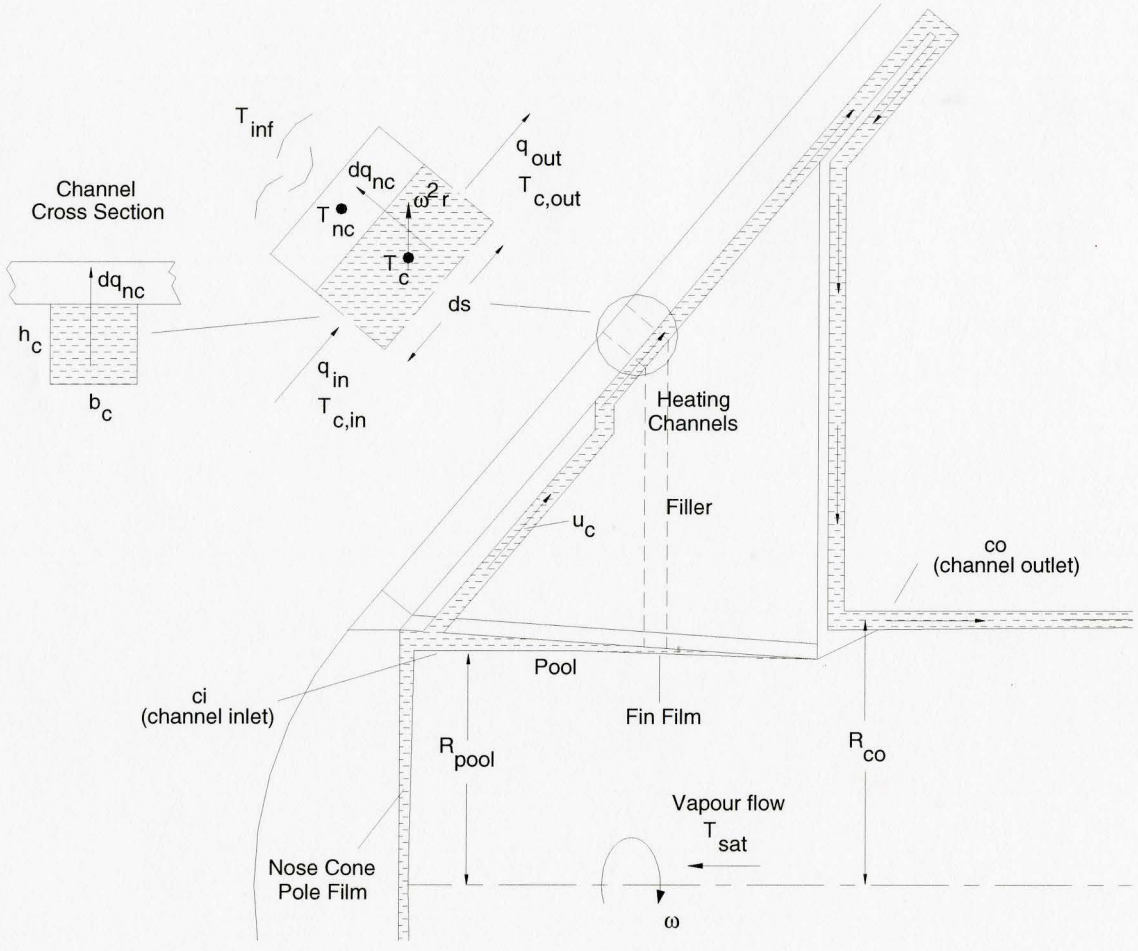

Figure 3.3: Schematic of the heating channel flow.

This term represents a correction to the first term. In practice, the fluid height at the outlet will depend on the fluid charge in the heat pipe, but any deviation from this value would be small. The third term accounts for the change in kinetic energy of the flow between the pool free surface and the outlet, often termed the outlet loss. The fourth term is the head loss or the energy dissipation through the channel. The major head loss was modeled using (Fox and McDonald, 1992)

$$h_l = \frac{f_c L_c u^2}{2D_c}, \tag{3.23}$$

where f_c is the friction factor, L_c is the total channel length of one channel and D_c is the hydraulic diameter. The minor losses other than the outlet loss were neglected. The friction factor was approximated using the result for laminar flow in a rotating pipe about an orthogonal axis given by (Mori and Nakayama, 1968)

$$\frac{f}{f_o} = 0.118\left(\frac{N}{X}\right)^{1/4} \frac{1}{1-2.82\left(\frac{N}{X}\right)^{-1/4}}, \tag{3.24}$$

where

$$N = \frac{\omega D_c^{\,2}}{2\nu}\mathrm{Re}_D, \tag{3.25}$$

$$X = \left[1+1.25\left(\frac{\omega D_c^{\,2}}{2\nu\,\mathrm{Re}_D}\right)^2\right]^{1/2} - 1.118\left(\frac{\omega D_c^{\,2}}{2\nu\,\mathrm{Re}_D}\right), \tag{3.26}$$

and f_o is the friction factor for laminar flow in a straight non-rotating pipe given by $f_o = 64/\mathrm{Re}_D$. Here, Re_D is the Reynolds number of the channel flow based on the

hydraulic diameter. The Reynolds number of the flow in the channels in all the cases considered here was below 100 so a turbulent correlation was not used. The change in the temperature of the liquid flow as it traveled along the channel was determined from the one-dimensional energy equation given by

$$\frac{\dot{m}_c C_p}{b_c}\frac{dT_c}{ds} = -q''_{nc}, \tag{3.27}$$

where $\dot{m}_c$ is the mass flow rate in the heating channel, C_p is the specific heat of the condensate, b_c is the width of the channel, $T_c(s)$ is the channel fluid temperature, s is the streamwise co-ordinate and q''_{nc} is the heat flux out of the channels and into the nose cone shell. The heat flux from the channel flow to the nose cone is given by

$$q''_{nc} = h_{channel}(T_c - T_{nc}), \tag{3.28}$$

where $h_{channel}$ is the heat transfer coefficient of the channel flow determined from (Mori and Nakayama, 1968)

$$\frac{Nu}{Nu_o} = \frac{\dfrac{0.216}{\zeta}\left(\dfrac{N}{X}\right)^{1/4}}{1-4.80\left[1-\dfrac{0.176}{\zeta}-\dfrac{0.07}{\zeta\,\mathrm{Pr}}\left(\dfrac{1}{\zeta}+4.33\right)\right]\left(\dfrac{N}{X}\right)^{-1/4}}, \tag{3.29}$$

for the cases when

$$\frac{\omega D_c^{\,2}}{2\nu\,\mathrm{Re}_D} \le \frac{\mathrm{Pr}}{2.236}\left(1-\frac{1}{\mathrm{Pr}^2}\right), \tag{3.30}$$

where

$$\zeta = \frac{2}{11}\left[1+\left(1+\frac{77}{4X}\frac{1}{\mathrm{Pr}^2}\right)^{1/2}\right], \tag{3.31}$$

$$Nu = \frac{h_c D_c}{k}, \tag{3.32}$$

and $Nu_o = 48/11$ for non-rotating pipe flow. For the cases when

$$\frac{\omega D_c^{\,2}}{2\nu\,\mathrm{Re}_D} > \frac{\mathrm{Pr}}{2.236}\left(1-\frac{1}{\mathrm{Pr}^2}\right), \tag{3.33}$$

the Nusselt number was determined from

$$\frac{Nu}{Nu_o} = \frac{\dfrac{0.216}{\zeta}\left(\dfrac{N}{X}\right)^{1/4}}{1-2.82\left[\zeta+\dfrac{0.5}{\zeta}-\dfrac{0.1}{\zeta^2}-\dfrac{0.8}{\zeta\,\mathrm{Pr}}\left(\zeta-\dfrac{0.25}{\zeta}+\dfrac{0.05}{\zeta^2}\right)\right]\left(\dfrac{N}{X}\right)^{-1/4}}, \tag{3.34}$$

where

$$\zeta = \frac{1}{5}\left[2+\left(\frac{10}{X}\frac{1}{\mathrm{Pr}^2}-1\right)^{1/2}\right]. \tag{3.35}$$

The solution for the heat transfer and temperature profile in the channels were coupled with the nose cone shell.

The temperature distribution in the nose cone itself was determined by solving the conduction equation. In the thicker central region of the nose cone the temperature distribution was determined by numerically solving the two-dimensional Laplace equation. The region was discretized using a grid that followed the contours of the nose cone. The physical grid was mapped onto a rectangular computational domain shown in figure 3.4 using the transformation given by (Anderson et al., 1984)

$$m = r \tag{3.36}$$

and

$$n = \frac{z}{f(r)}. \tag{3.37}$$

The transformation generates a physical grid with equal spacing in the radial direction and even spacing in the normal direction. The heat transfer modes for the boundary control volumes shown in figure 3.4, were treated using an energy balance method. The heat flux at the wall under the condensing film was given by

$$q'' = \frac{k}{\delta_{nc,film}}\left(T_{sat} - T_{p,q}\right). \tag{3.38}$$

The portion of the wall in contact with the pool was assumed insulated so that $q'' = 0$ over this region. The top boundary of the nose cone pole in contact with the junction region was assumed to be at a constant temperature T_j of the junction as indicated in figure 3.4.

The heat flux from the outside nose cone surface to the ambient was modeled as a combination of forced convection and heat transfer due to the impacting water droplets from the atmosphere. The droplets were assumed to be unaffected by the flow field around the nose cone and to impact directly on the surface and immediately increase from the ambient temperature to the surface temperature. The heat flux from the surface to the impacting droplets was estimated using

$$q'' = \rho_{LWC} U C_p \left(T_{p,q} - T_{\inf}\right), \tag{3.39}$$

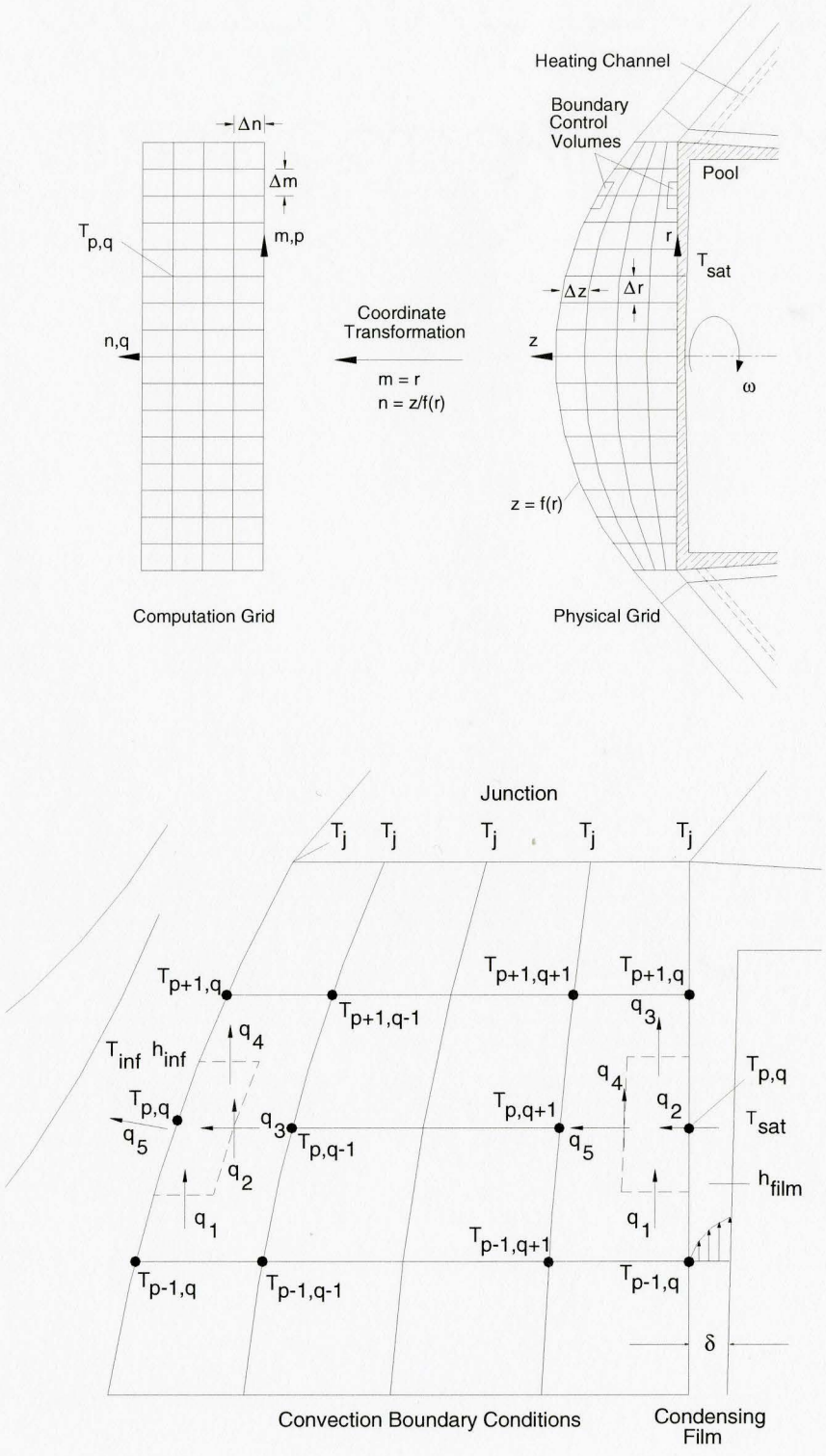

Figure 3.4: Schematic of the two-dimensional grid used to solve the temperature distribution in the central region of the nose cone.

where U is the airplane speed and C_p is the specific heat of the water droplets in the atmosphere. In many icing calculations, it is assumed that the droplets form a thin film driven back along the surface by aerodynamic shear, however Kind et al. (1998) noted that in some cases the droplets bead together in small discrete clusters and flow back along the surface. This would act to cause surface roughness augmenting the convective heat transfer to the air. This would be a worse case for anti-icing applications so the forced convection heat transfer was modeled using the correlation proposed by Axcell and Thianpong (2001) for turbulent heat transfer to a rotating disk with surface roughness in axial flow given by

$$Nu = \frac{h_{conv} r}{k} = 0.0045 \mathrm{Re}^{*0.986}, \tag{3.40}$$

where h_{conv} is the convective heat transfer coefficient, r is the local radius of the nose cone outer surface, k is the thermal conductivity of the ambient air evaluated at the film temperature. The modified Reynolds number Re*, was given by

$$\mathrm{Re}^* = \left[\left(\frac{\omega r^2}{\nu} \right)^2 + \left(\frac{U r}{\nu} \right)^2 \right]^{1/2}, \tag{3.41}$$

where ν is the kinematic viscosity of air evaluated at the film temperature. A detailed outline of the two-dimensional computation method used for the nose cone pole is given in appendix B.1.

The Biot number for the nose cone beyond the central region and the extended tapered fin in the condenser shown in figure 3.5 were found to be less than 0.1. This result indicated that temperature variations through the thickness of the nose cone shell

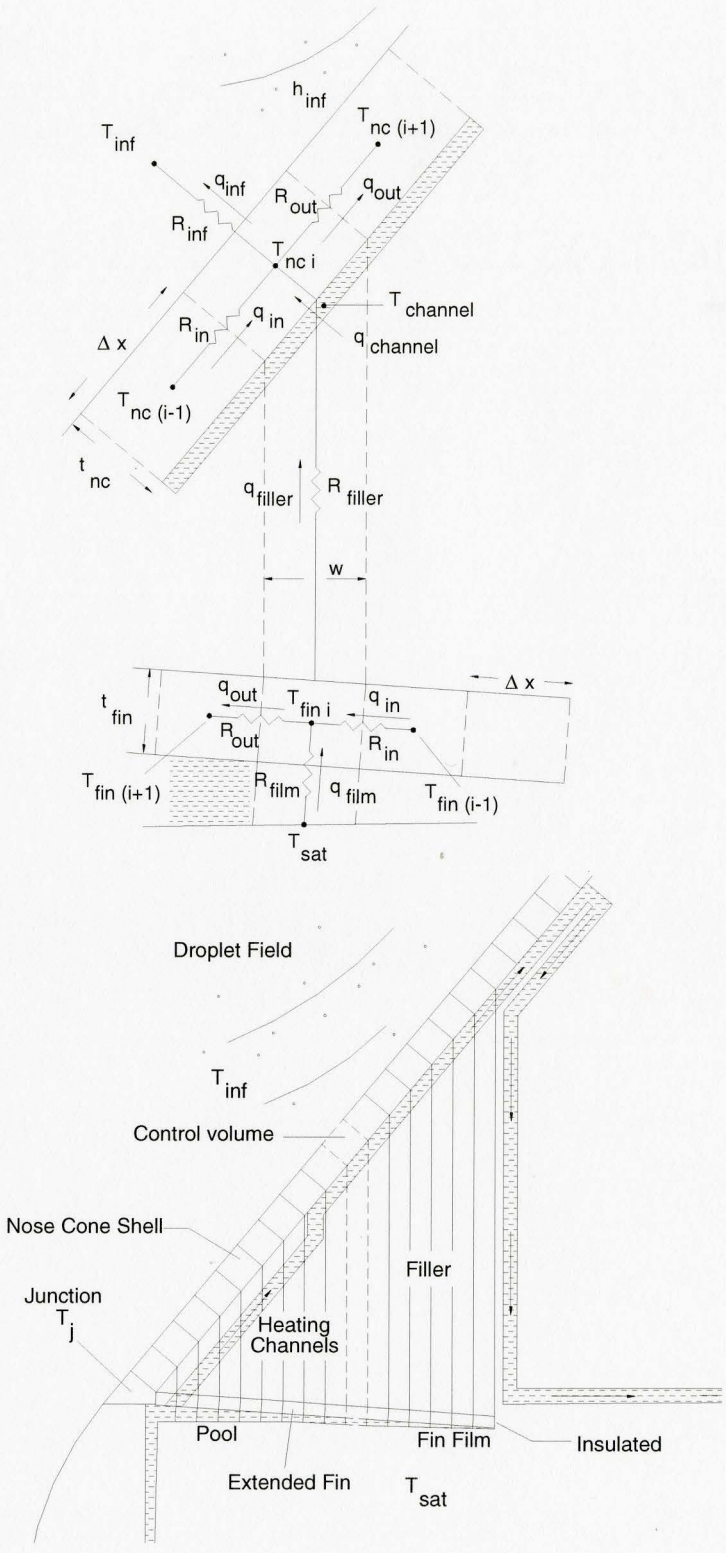

Figure 3.5: Schematic of the heat transfer model in the extended nose cone region.

and the thin extended fin would be negligible (Incopera and DeWitt 1996). The temperature distributions along the length of each fin were thus modeled in one-dimension. The polycrystalline graphite filler that would be added into the nose cone had a highly anisotropic thermal conductivity. It was proposed that it would conduct heat primarily in the radial direction so the filler material acts as a heat transfer conduit from the extended fin to the shell. The conduction in the other direction is typically an order of magnitude smaller and was neglected. The temperature distribution in the nose cone shell, the extended fin and the polycrystalline graphite filler were determined using a one-dimensional formulation as shown in figure 3.5. The thermal resistance between the filler and the nose cone and the fin were neglected. Insulated boundary conditions were used at the end of the extended fin and the nose cone shell.

The heat transfer modes in the junction region connecting the central region of the nose cone to the shell and extended fin are shown in figure 3.6. The junction was assumed to have a constant temperature throughout and a quasi one-dimensional model was used to compute the heat transfer in this region. This method provided a simple way of coupling the conduction heat transfer rates from the end wall of the heat pipe and the extended fin to the nose cone shell. The energy balance for the region is given by

$$q_{endwall-j} + q_{fin-j} - q_{j-ncshell} - q_{j-amb} = 0\,, \tag{3.42}$$

where the subscript "j" indicates the junction. The conduction heat transfer from the end wall of the heat pipe, the fin and the thin shell of the nose cone were estimated using a quasi one-dimensional formulation. The convection heat transfer from the outside

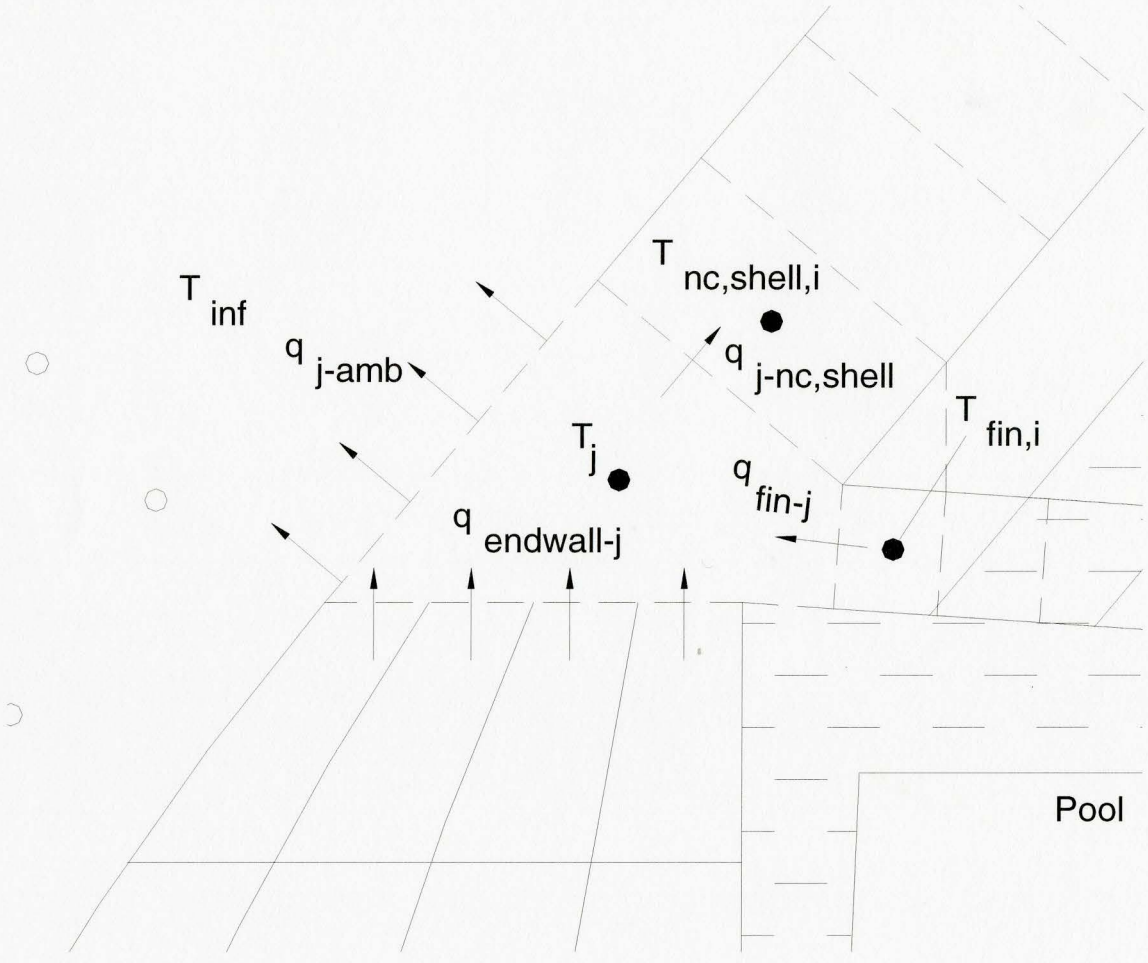

Figure 3.6: Schematic of the junction region between the thicker central region of the nose cone, the nose cone shell and the extended fin.

surface was computed using (3.40 and 3.41). A detailed description of the junction heat transfer model is given in appendix B.2.

The steady state solution for the condenser and the nose cone was determined iteratively using a computer algorithm given in appendix B.3. The solution was initiated by assuming a junction temperature and temperature distributions for the extended fin and the end of the heat pipe. The pool height was then found iteratively based on the condensation given the temperature profiles. The temperature of the junction was then found based on the current guess of the pool height and condensation films such that the heat transfer from the nose cone matched the heat transfer from the working fluid. The pool height and condensation films for the new temperature distributions were found and the procedure was repeated until there was an overall energy balance.

3.3 The Evaporator Design

A schematic of the evaporator design considered here for one type of aero-engine application is shown in figure 3.7. Following Song et al. (2003b), the heat transfer on the inside of the heat pipe is modeled using a mixed convection model. The velocity profile for the liquid film was modeled using a power law velocity profile given by

$$\frac{u}{U} = \left(\frac{y}{\delta}\right)^b, \tag{3.43}$$

where U is the maximum film velocity at the liquid vapour interface and the exponent b models the shape of the velocity profile. The shape depends upon whether the film is

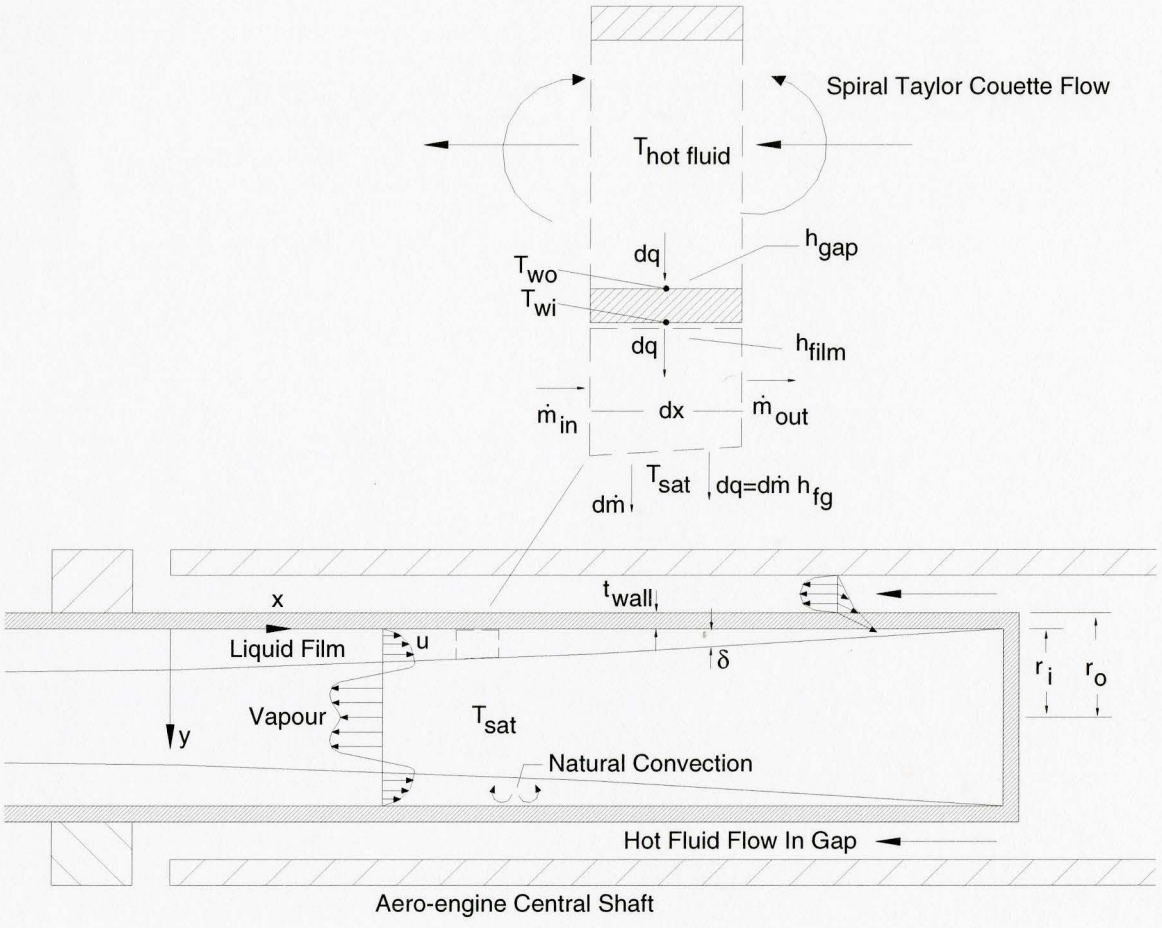

Figure 3.7: Schematic of the aero-engine evaporator.

laminar or turbulent and also on the influence of mixed convection. Following Song et al. (2003b), for cases where $Ra < 10^9$ for $1 < {Gr}/{\mathrm{Re}^2} < 10$ indicating laminar flow,

$$b = \frac{1}{3} \tag{3.44}$$

while for ${Gr}/{\mathrm{Re}^2} > 10$

$$b = \frac{1}{4}. \tag{3.45}$$

For turbulent flow where $Ra > 10^9$

$$b = \frac{1}{7}. \tag{3.46}$$

Here the Grashof number, the Reynolds number and the Rayleigh number are given by

$$Gr = \frac{\omega^2 r \cos(\gamma)\beta\Delta T\delta^3}{\nu^2}, \tag{3.47}$$

$$\mathrm{Re} = \frac{4U\delta}{\nu}, \tag{3.48}$$

and

$$Ra = Gr\,\mathrm{Pr}, \tag{3.49}$$

where β is the volumetric expansion coefficient and Pr is the Prandtl number. The film thickness was solved using the momentum integral equation. Neglecting the convective terms, the momentum balance in the film is given by

$$\int_0^{\delta} \omega^2 r\left(\sin\gamma - \cos\gamma\frac{d\delta}{dx}\right)dy - \frac{\tau_w}{\rho} = 0, \tag{3.50}$$

where γ is the taper angle of the wall. The first term is the driving force in the liquid film due to the wall taper angle and the pressure gradient; the driving force is in balance with the viscous force. The wall shear stress τ_w was estimated from

$$\tau_w = \frac{C_f \rho U^2}{2}, \tag{3.51}$$

where C_f is the skin friction coefficient. The free stream velocity U was also determined using equation (3.51). The skin friction coefficient was estimated following the approach of Afzal and Hussain (1984) for mixed convection in a boundary layer over a horizontal flat plate. The skin friction coefficient depended on the parameter K given by

$$K = \frac{Gr}{\mathrm{Re}^{5/2}}, \tag{3.52}$$

that is a measure of the importance of mixed convection. For cases where $0 < K < 1$ and forced convection is dominant, the skin friction coefficient is given by

$$C_f = 0.5, \tag{3.53}$$

while for cases where $K > 1$ and natural convection is dominant, the coefficient is given by

$$C_f = 0.5K^{3/5}. \tag{3.54}$$

Following Song et al. (2003b), the heat transfer across the film was evaluated by

$$q'' = h_{film}(T_{wi} - T_{sat}), \tag{3.55}$$

where the heat transfer coefficient was computed from

$$Nu_m^{7/2} = Nu_f^{7/2} + Nu_n^{7/2}, \tag{3.56}$$

where Nu_f and Nu_n are the Nusselt numbers for forced and natural convection respectively. For laminar film flow, the Nusselt number for forced convection is

$$Nu_f = 1, \tag{3.57}$$

while the Nusselt number for natural convection was estimated by (Marto, 1984)

$$Nu_n = 0.133Ra^{0.375}. \tag{3.58}$$

The change in the mass flow in the film was estimate by

$$\frac{d\dot{m}}{dA} = -\frac{q''}{h_{fg}}. \tag{3.59}$$

The heat transfer inside the heat pipe was coupled to the conduction through the heat pipe wall and the heat transfer from the lubricant flow outside of the rotating heat pipe. The axial conduction along the length of the heat pipe was neglected, thus the heat flux through the wall on the inside of the heat pipe is given by

$$q'' = \frac{T_{wo} - T_{wi}}{\frac{r_i}{k_w}\ln\left(\frac{r_o}{r_i}\right)}, \tag{3.60}$$

where T_{wo} is the temperature on the outer surface and k_w is the thermal conductivity of the heat pipe wall. The heat flux on the outside of the heat pipe wall was estimated from

$$q'' = h_{gap}\left(T_{hot,fluid} - T_{wo}\right), \tag{3.61}$$

where h_{gap} is the heat transfer coefficient on the outside of the heat pipe as it rotates in the stationary fluid jacket and $T_{hot,fluid}$ is the temperature of the working fluid heated by

the aero-engine. The temperature drop of the fluid in the gap over the length of the evaporator was small hence the temperature variation was neglected. The Nusselt number for the gap is given by

$$\frac{Nu}{\mathrm{Pr}^{1/3}} = 0.65 Ta_m^{0.226}, \tag{3.62}$$

where (Becker and Kaye, 1962)

$$Nu = \frac{2h_{gap}\delta}{k_{gap}}. \tag{3.63}$$

The evaporator was discretized into finite control volumes along the length of the heat pipe. The film thickness was determined by iteratively balancing mass, momentum and thermal energy for each volume based on the current guess of the wall temperature profile. It was assumed that the heat pipe contained a minimum charge of fluid and thus the film thickness at the end cap was assumed to be zero in the solution. Song et al. (2003b), found that the performance of the evaporator was relatively independent of the film thickness because the natural convection in this region increased as more fluid was included in the heat pipe. The film thickness solution was determined using a shooting method similar to that used for the condensate films. The wall temperature profile was then solved and the procedure was repeated until the heat transfer required to evaporate the fluid from the film was attained. A detailed outline of the computer algorithm used to compute the performance of the evaporator is given in appendix B.3.

The heat transfer in the condenser section and the evaporator section were coupled together by matching the vapour temperature in the two solutions. Following Daniels and Al-Jumaily (1975) and others, it was assumed there was no change in the

vapour temperature in the adiabatic section. Thus, the solutions were coupled by ensuring the mass flow of the vapour and the temperatures of the vapour in the two sections were equal.

Chapter 4 Heat Transfer Enhancement in Axial Taylor Couette Flow

Preliminary calculations showed that the thermal resistance on the outside of the rotating heat pipe in the evaporator was relatively large. Thus, it would be necessary to enhance the heat transfer in this region. There did not appear to have been any systematic experiments to examine the effect of heat transfer enhancement in this flow. So experiments were performed to characterize the heat transfer enhancement produced by adding two or three-dimensional roughness in this flow. As noted in the previous chapter, the applications of interest here have Taylor numbers of 10^6 – 10^8 and axial Reynolds numbers greater than 1000. The facility used in the investigation is presented first. The results are then presented and discussed.

4.1 Test Facility and Instrumentation

A schematic of the test facility used to measure the heat transfer for the axial Taylor Couette flow of interest here is shown in figure 4.1. The facility was similar to the facility used by Song et al. (2003a) to test rotating heat pipes. The facility consisted of an open cold-water loop and a closed hot-water loop that exchange heat at the test section attached to the end of a central shaft. The central shaft was hollow so that the cold water could flow through the center. The test section, located on the end of this central shaft, was enclosed in a stationary water jacket designed so there was a small annular gap between the rotating test cylinder and the outer wall. The hot water was

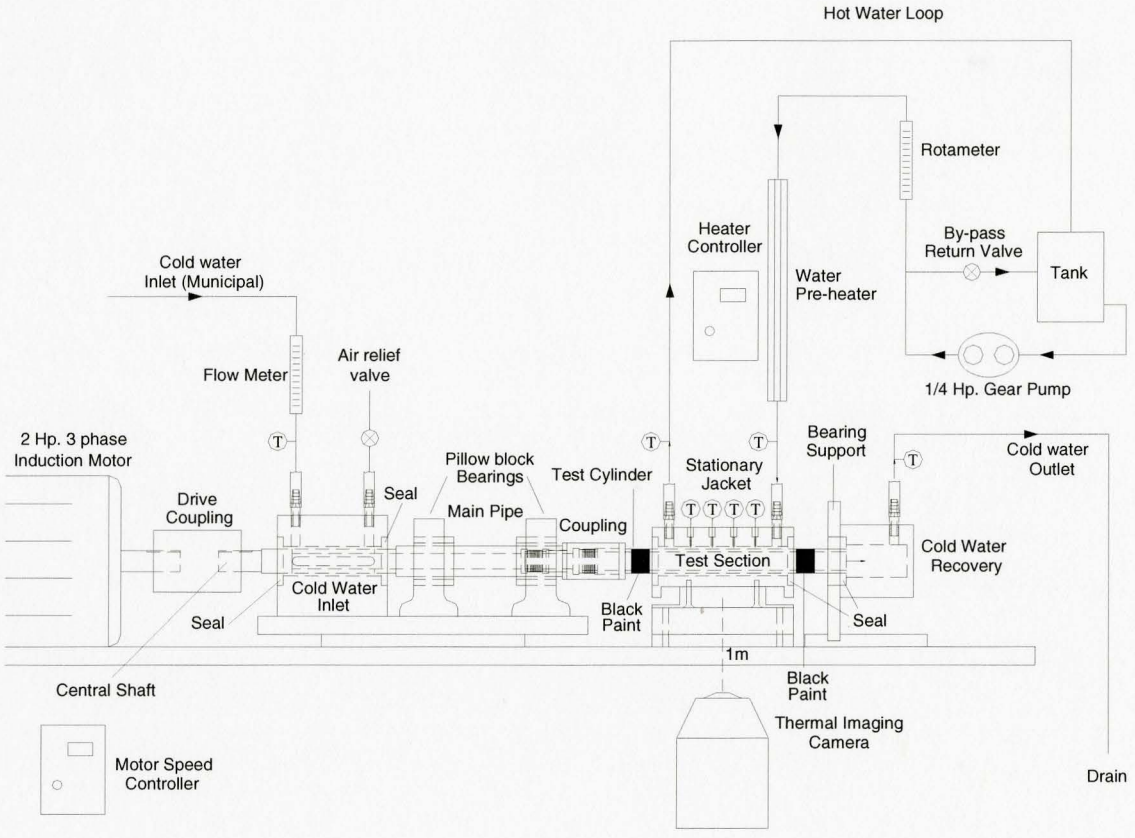

Figure 4.1: Schematic diagram of the test facility.

pumped through this gap from an inlet located at one end of the jacket to an outlet at the other end of the jacket. The cold water flowed inside the central shaft from the cold-water inlet upstream of the test section to the outlet downstream of the test section. The shaft was driven by a motor connected to the left end of the shaft by a plastic coupling. The heat transfer was measured for three test sections. The outer surface on the first test section was smooth. The outer surface on the second test section had two-dimensional axial rib roughness while the third test section had three-dimensional cubic protrusions.

A detailed schematic of the stationary jacket surrounding the test cylinder is shown in figure 4.2. The jacket was made from clear Acrylic and had an overall length of 145 mm with an inner bore diameter of 30.5 mm. The hot water was circulated through the gap from the inlet to the outlet located 111 mm apart. A CR 10131 seal was used on each end of the jacket to seal the gap. The whole test section was supported with an aluminum base structure bolted to the table. The temperature of the flow in the gap was measured using four 0.508 mm diameter T-type thermocouples positioned between the inlet and the outlet. These thermocouples had special limits of error of $\pm$ 0.5°C. The junctions were immersed into the flow a distance equal to one-half of the gap height.

The hot water that circulated through the gap was supplied in a closed loop. The water in this loop was circulated using a ¼ Hp. Leeson gear pump. The flow to the pump was drawn from a reservoir and a portion of the flow exiting the pump was returned to the reservoir through the bypass loop in order to control the flow rate to the water jacket. The flow rate to the water jacket was measured downstream of the bypass loop using an Omega FL-1501A rotameter with a capacity 3 L/min and an accuracy of 2% of full-scale.

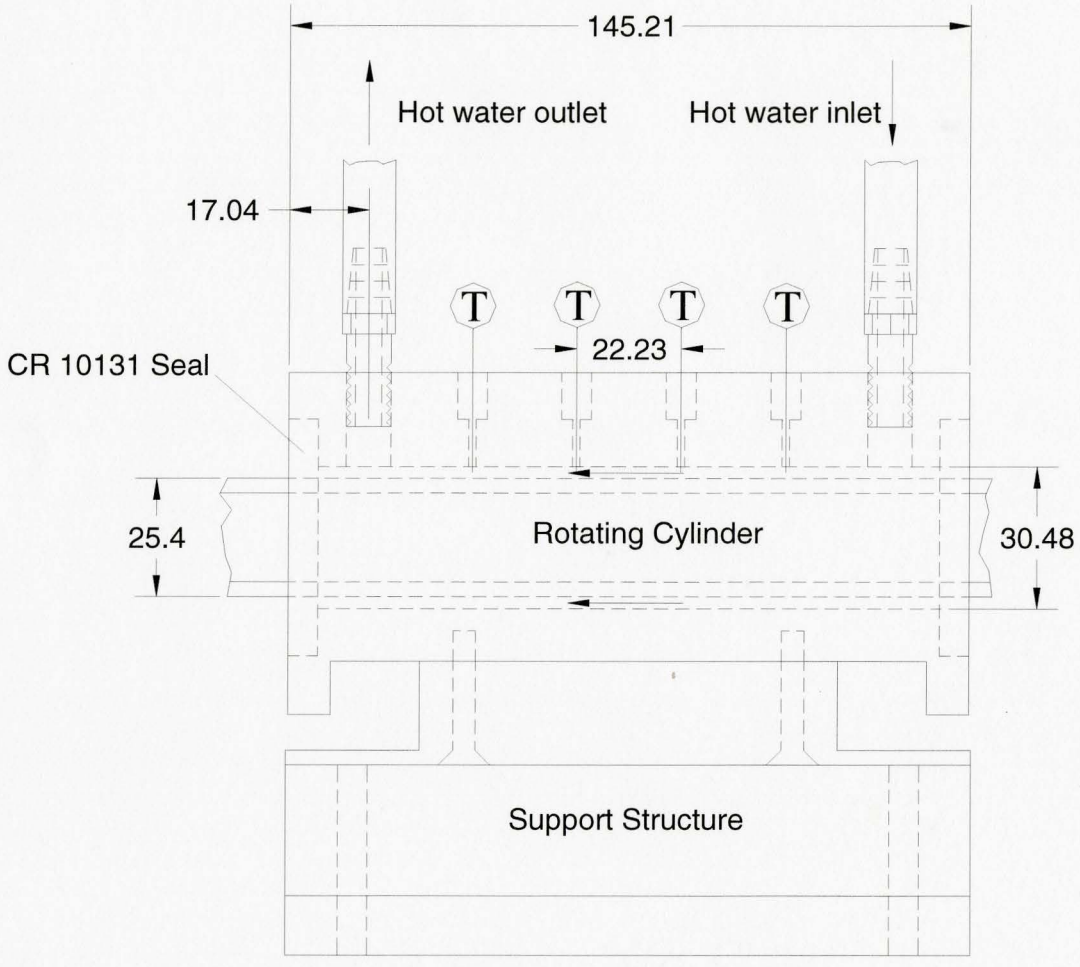

Figure 4.2: Schematic of the stationary water jacket and test cylinder, (all dimensions in mm).

The water flow then passed through a copper pipe equipped with a 2kW tape heater that was used to heat the water entering the test section. The tape heater was approximately 1 m long and was secured to the pipe with epoxy resin. A T-type thermocouple was attached to the outside of the copper pipe at the midpoint of the taper heater. This thermocouple was used as an input to a LOVE 16A2 PID controller that controlled the power supply to the tape heater. It was found that this system could maintain the temperature of the water entering the water jacket to within ± 0.3°C. The temperature of the hot water at the inlet and the outlet of the jacket were each measured using 1.59 mm diameter T-type thermocouples with special limits of error of ± 0.5°C. The hot water exiting from the test section was then returned to the reservoir.

The cold water flowing through the inside of the shaft was obtained from the building supply. The flow rate was measured using a Gilmont Flow meter with a capacity of 4.9 L/min and an accuracy of 2% of full scale. The cold water flow rate was controlled using a gate valve positioned upstream of the flow meter. The cold-water then entered the central shaft at the cold-water inlet through an Acetyl jacket similar to the water jacket at the test section. Slots were machined into the shaft to allow the cold water to enter the shaft as it rotated. One end of the main shaft was sealed while the rest was hollow so that all the water entering the main shaft flowed to the test section. The temperature of the water entering the shaft was measured using a 1.59 mm diameter T-type thermocouple. The main shaft was equipped with two Acetyl sleeves at each of the pillow block bearings to insulate the cold water from the effects of bearing heating. The test sections were connected to the main shaft using an Acetyl coupling that thermally

isolated the test cylinder from the main shaft. The inside of the test sections included two 4 mm thick Acetyl sleeves on either side of the water jacket to reduce heat transfer to the cold water outside of the water jacket. The cold water then flowed through the test section to the outlet that was supported using a bearing assembly. The flow exited the test cylinder into a cold-water recovery jacket and then to the drain through an outlet line. The cold-water outlet temperature was measured in the outlet line after the recovery jacket using a 1.59 mm diameter T-type thermocouple. The thermocouples used at the inlet and the outlet each had special limits of error of ± 0.5°C. The outlet line was elevated 1 m above the test facility to maintain pressure inside the central shaft. An air relief valve at the cold-water inlet was used to purge the air from the central shaft.

The rotameter used to measure the flow rate in the hot water loop and the flow meter used to measure the flow rate in the cold-water loop were calibrated by running flow from the meters and then weighing the water. The calibration was executed by weighing 20 kg to 25 kg of water collected over a 10 min to 14 min period using a stopwatch. The weighing scale had an accuracy of ± 1g and the error using the stopwatch was estimated at ± 0.5 seconds. The calibration range for the rotameter used in the hot water loop was 40% to 90% of full scale in increments of 10% and three trials were performed at each increment. The resulting calibration curve is shown in figure 4.3. The data was fit with a linear polynomial using the least squares method in the form

$$\dot{m}_h = 0.0005201R + 0.0005208 \ kg/s, \tag{4.1}$$

where R is the scale reading between 40 and 90. The cold-water flow was maintained at 40% of full scale (1.8 L/min) throughout the experiments and five trials were used to calibrate the flow meter at this flow rate.

The surface temperature on the test sections outside of the water jacket was measured using a high-speed infrared camera (Flir Therma-cam model SC3000) with an accuracy of ±1°C. A 19 mm wide strip on either side of the jacket was painted using flat black enamel paint (Tremclad brand). The camera was positioned 1m from the hot water jacket and the hot water jacket and surrounding area was observed. The emissivity of the black paint used on the test sections was calibrated using the setup shown in figure 4.4. Three coats of paint were applied to a region on the outside of a thin walled metal container and the surface temperature was measured using four T-type thermocouples (Omega brand SA1-T-72-SC). The four thermocouples had an accuracy of ± 0.7°C. The thermal imaging camera was positioned 1m from the container, the same distance used in the experiments, and directed at the painted region on the container. The container was initially filled with ice. The four temperatures were measured every 5 seconds for 30 seconds after steady state had been reached. The average surface temperature was 1.2°C and the four readings agreed to within ± 0.1°C. The procedure was repeated for boiling water and the average wall temperature was 97.4°C. The emissivity from these measurements was 0.94 ± 0.01. This agreed reasonably well with the calibration results of Gao (2000) who used a similar method with the same camera and found an emissivity of 0.94 to 0.97 for black soot paint. The sensitivity of the surface temperature to the emissivity calibration was examined using the metal container at room temperature. The

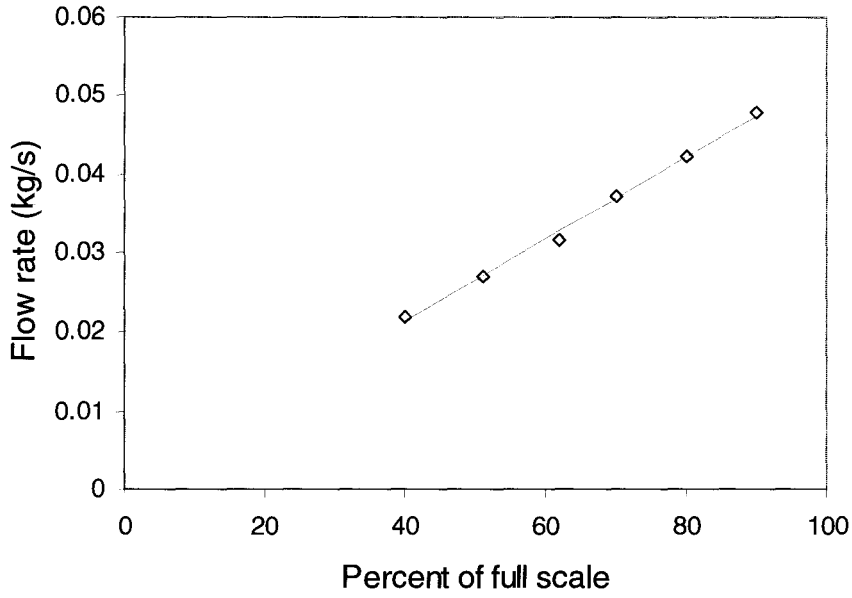

Figure 4.3: Calibration results for the hot water loop rotameter.

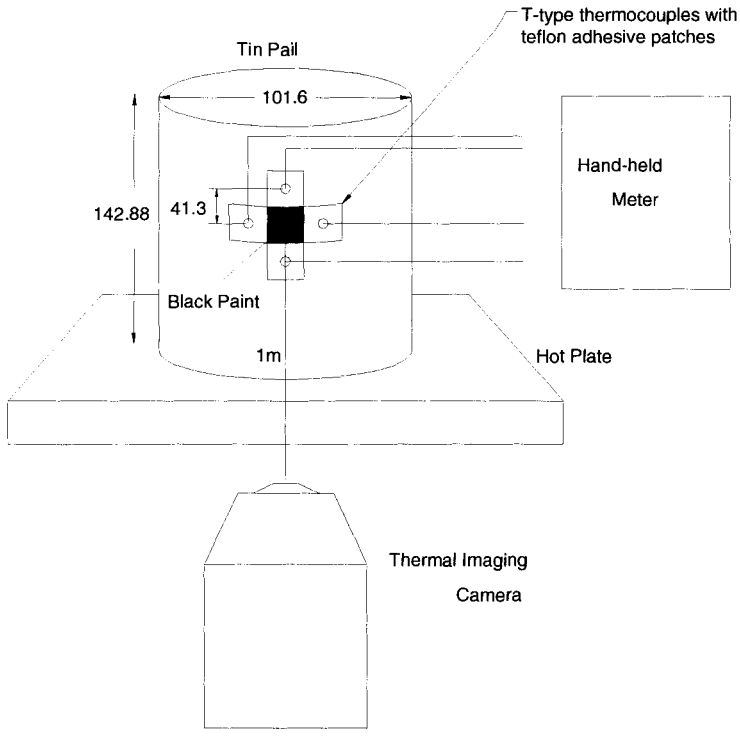

Figure 4.4: Schematic of the setup used to calibrate the emissivity of the black paint.

surface temperature of the painted region was 25.7°C at steady state. When the emissivity was changed from 0.94 to 0.90, the temperature measured by the camera increased by 0.01°C. It was concluded that small discrepancies in the emissivity would not have a significant effect on the surface temperature measurement.

The rotation speed of the central shaft was measured using a digital photo tachometer with an accuracy of ± 1 rpm. The rotation speed of the central shaft was calibrated against the read-out displayed on the inverter that was used to vary the speed of the motor. The calibration was carried out in increments of 5 units on the inverter display over the range of 5 to 80 and the results are shown in figure 4.5. The data was fit with a linear profile using the least squares technique and the result is given by

$$\omega = 59.746R \ (rpm), \tag{4.2}$$

where R is the read-out on the inverter.

The output from the thermocouples was acquired using a National Instruments SCB-68 16 channel data acquisition board and using an Omega brand multi-channel temperature readout. The time dependent change in the temperatures was initially monitored using the data acquisition system. It was found that the steady state temperatures were not accurate enough to yield an accurate energy balance. As a result, the Omega brand multi-channel readout was used to record the steady state temperatures.

The test cylinders used here were made from 6061-T6 aluminum alloy and had similar overall dimensions of 273 mm in length, 25.4 mm outer diameter, and wall thickness of 3.175 mm. A schematic of the smooth test cylinder is shown in figure 4.6. The outer surface of the smooth test cylinder was polished to eliminate scratches. The

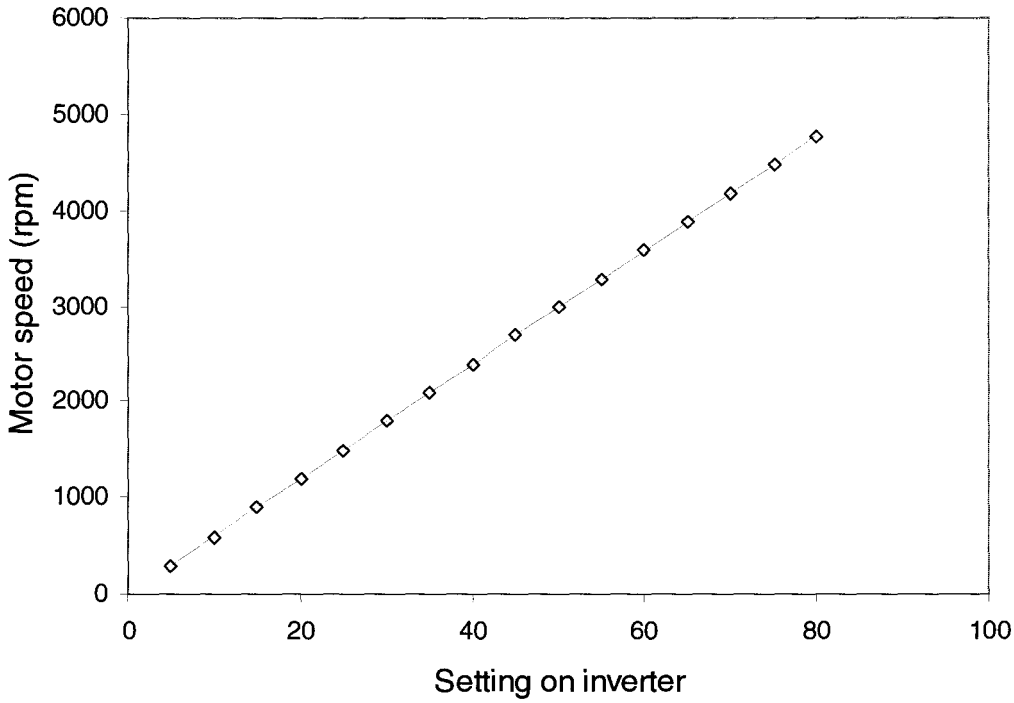

Figure 4.5: Calibration results for the rotation speed of the central shaft.

smooth cylinder was used as the reference for comparison with the augmented surfaces in this investigation since the heat transfer here occurred in a finite length Taylor-Couette flow device and could differ from other studies with much larger length to gap ratios. The second test section included axial ribs on the outer surface of the test section as shown in figure 4.7. The spacing between the ribs was approximately 10.5 rib heights and the ribs were 4.5 rib heights in width. The ratio of the rib height to gap height in the annulus was 0.05. This geometry is consistent with those that achieve maximum heat transfer enhancement for single-phase flows in rectangular and annular ducts (Kalinin and Dreitser, 1998). The third test section had three-dimensional protruding elements on the outer surface as shown in figure 4.8. The cubes were approximately 1.27 mm in height and extended one-half of the distance from the base of the cubes to the surrounding stationary wall of the water jacket. The spacing between adjacent cube faces in the peripheral direction was approximately 5.96 cube heights while the span-wise spacing was 3 cube heights. The array geometry is consistent with those used in rectangular duct flows (Garimella and Eibeck, 1990). The outer surface between the cubes was formed by milling away the material between the cubes. The maximum deviation of the surface profile from a true circular shape was estimated to be on the order of $\pm$ 0.005 mm.

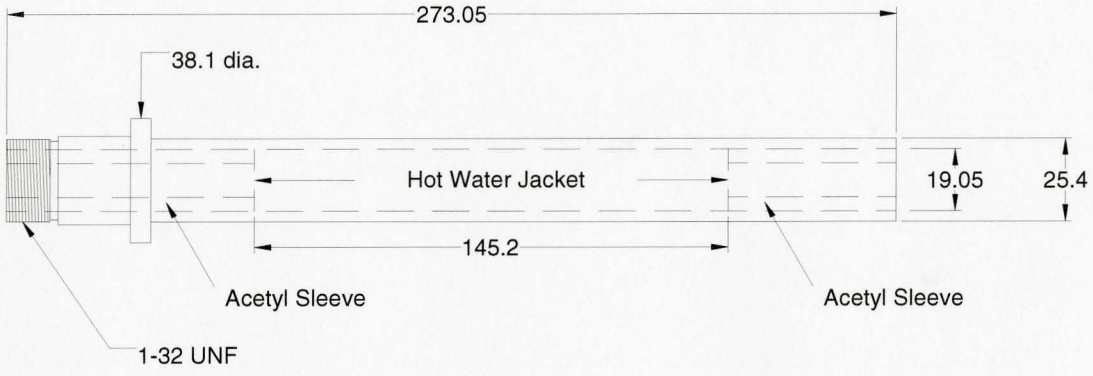

Figure 4.6: Schematic of the smooth test section; dimensions in mm.

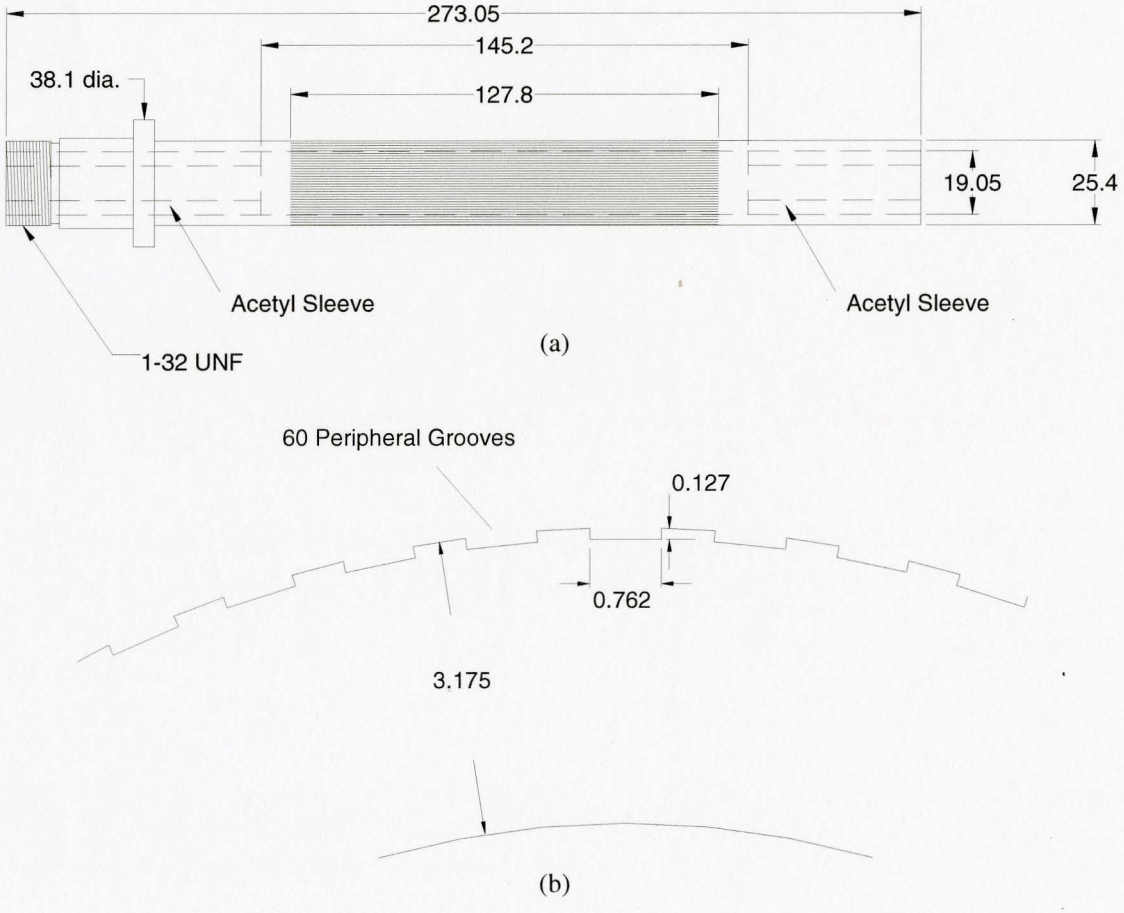

Figure 4.7: (a) schematic of the axial grooved test section, (b) detailed drawing of the axial grooves; all dimensions in mm.

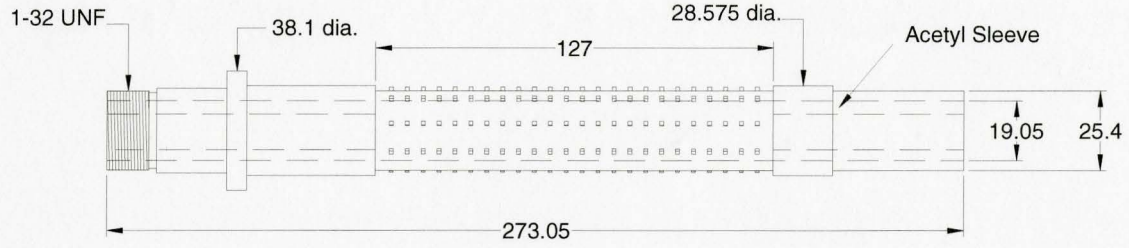

(a)

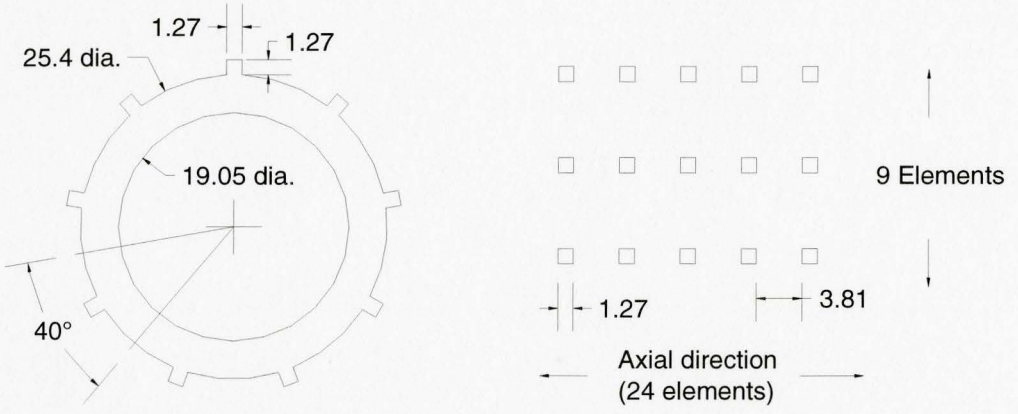

(b)

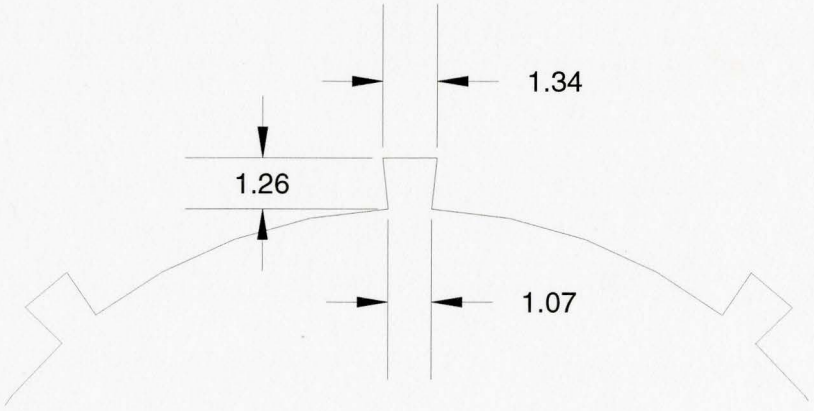

(c)

Figure 4.8: (a) schematic of the cubic protrusion test section, (b) detailed drawing of the array, (c) detailed drawing of a cubic protrusion; all dimensions in mm.

4.2 Experimental Procedure

The heat transfer measurements for all of the test sections were performed at a cold-water flow rate of 1.8 L/min (40% of full scale). The hot-water flow was varied to change the axial Reynolds number. The hot water flow rate was initially set to 40% of full scale. The tape heater control was then adjusted to 30°C and was increased by 5°C approximately every 10 minutes until the temperature had reached approximately 60°C. The cold and hot water loops were monitored for approximately 1.5 hours to ensure that both loops had reached steady state operation.

The rotation of the shaft was then started at approximately 420-rpm and the inlet and outlet temperatures of the cold and hot water loops were recorded using the data acquisition system. In all cases, the system was allowed to operate for 15 minutes after it had appeared to reach steady state before the measurements for the heat transfer analysis were performed. The thermocouples were then plugged into the multi-channel system and each temperature was recorded every 5 seconds for 90 seconds. The temperatures at these intervals were then averaged to estimate the temperature at the inlets and outlets. The surface temperature on each side of the test cylinder was then recorded using the thermal imaging camera. The motor speed was then increased to the next speed and the procedure was repeated until the desired speed range had been covered.

4.3 Data Reduction

The heat transfer across the surface of the cylinder was evaluated by determining both the heat transfer out of the hot water and the heat transfer into the cold water. The heat transfer out of the hot water was evaluated using

$$Q_{hot} = \dot{m}_h C_{p\bar{h}} (T_{hi} - T_{ho}), \tag{4.3}$$

where $\dot{m}_h$ is the hot water mass flow rate, T_{hi} and T_{ho} are the inlet and outlet temperatures at the water jacket and $C_{p\bar{h}}$ is the specific heat of the hot water evaluated at the average hot water temperature of the inlet and outlet. The heat transfer into the cold water was determined using

$$Q_{cold} = \dot{m}_c C_{p\bar{c}} (T_{co} - T_{ci}), \tag{4.4}$$

where $\dot{m}_c$ is the cold water mass flow rate, T_{ci} and T_{co} are the inlet and outlet temperatures of the cold water. The heat transfer out of the hot water was transferred into the cold water and conducted out of the ends of the test cylinder wall. It was thought that the heat conducted down the cylinder wall would be rejected to the ambient because Acetyl sleeves were included inside of the test cylinder. The heat transfer rate from the hot water to the cold water was estimated as

$$Q_{hot-cold} = Q_{hot} - Q_{cond,l} - Q_{cond,r}, \tag{4.5}$$

where $Q_{cond,l}$ and $Q_{cond,r}$ are the conduction heat transfer rates through the wall at the left and right sides of the water jacket. The heat transfer conducted through the wall was estimated from the temperature profiles measured along the surface of the test cylinder near the edges of the water jacket by

$$Q_{cond} = -kA\frac{\partial T}{\partial x}\bigg|_{jacket}, \tag{4.6}$$

where A is the cross-sectional area of the test cylinder and k is the thermal conductivity of the test cylinder. Four independent measurements of the surface temperature profiles were obtained from the camera for each case at steady state. The measurement locations are shown schematically in figure 4.9. The lines labeled 1 and 2 measure the axial surface temperature variation while the lines 3 and 4 measure the vertical variation. A typical set of axial and vertical profiles are shown in figure 4.10. The temperature was found to be uniform in the vertical direction during the experiment and it was concluded that the axial profiles were representative of the temperature distribution around the cylinder. The axial profiles were fit with second order polynomials using the least squares method. The temperature gradient was then estimated from the polynomial at the end of each paint strip nearest the water jacket. The conduction heat transfer along the test cylinder walls was typically 5W – 10W and accounted for less than 2% of the total heat transfer from the hot water during the experiments.

The energy balance for the smooth test cylinder results is shown in figure 4.11. The energy balance was found to be within ± 10% and this was thought to be reasonable.

The surface temperature of the test cylinder at the edge of the seal on the inside of the water jacket was estimated from the axial temperature profiles measured with the camera. This was done to estimate the temperature of the heat transfer surface. The polynomial curve fits were extrapolated from the edge of the paint strip nearest the water jacket to the edge of the seal lip inside the jacket as shown in figure 4.12. It was assumed

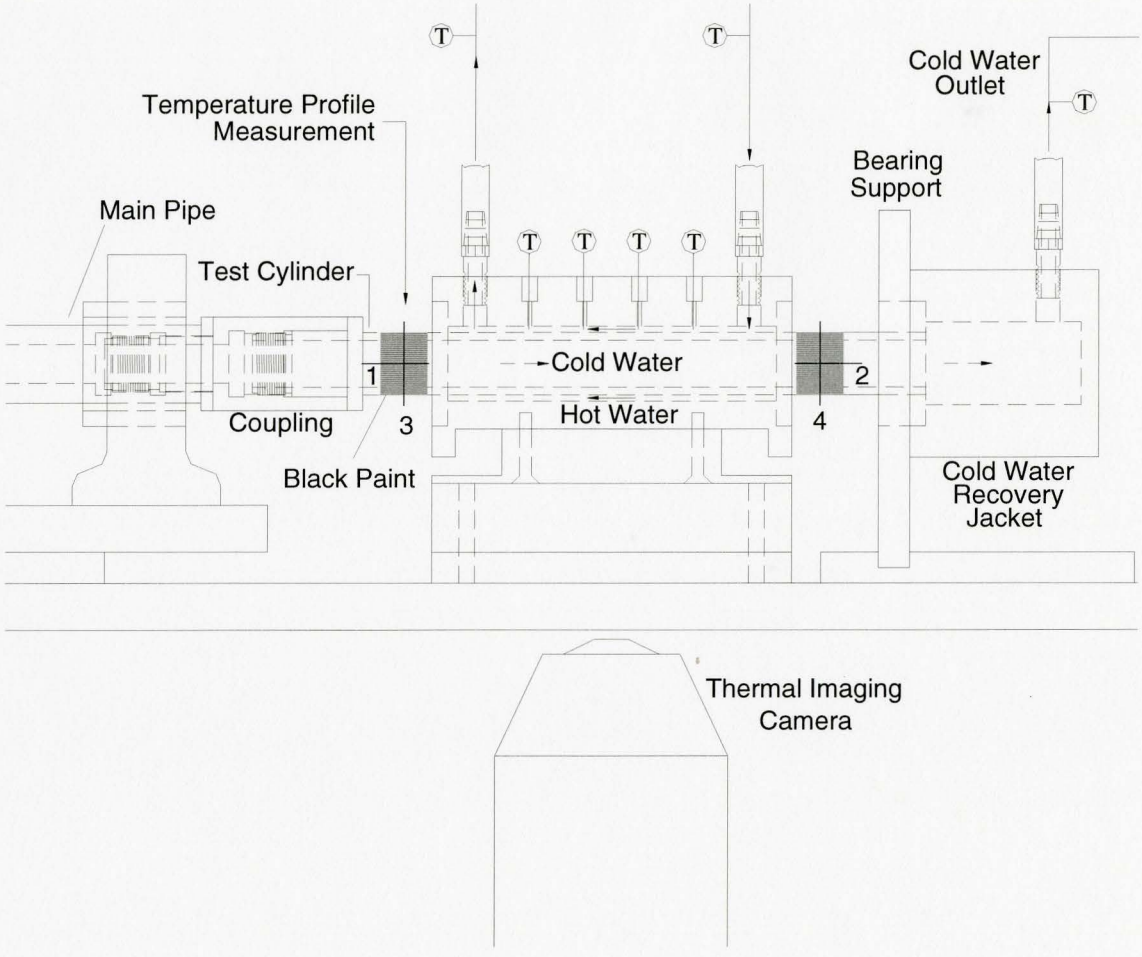

Figure 4.9: Schematic showing the locations of the surface temperature profiles.

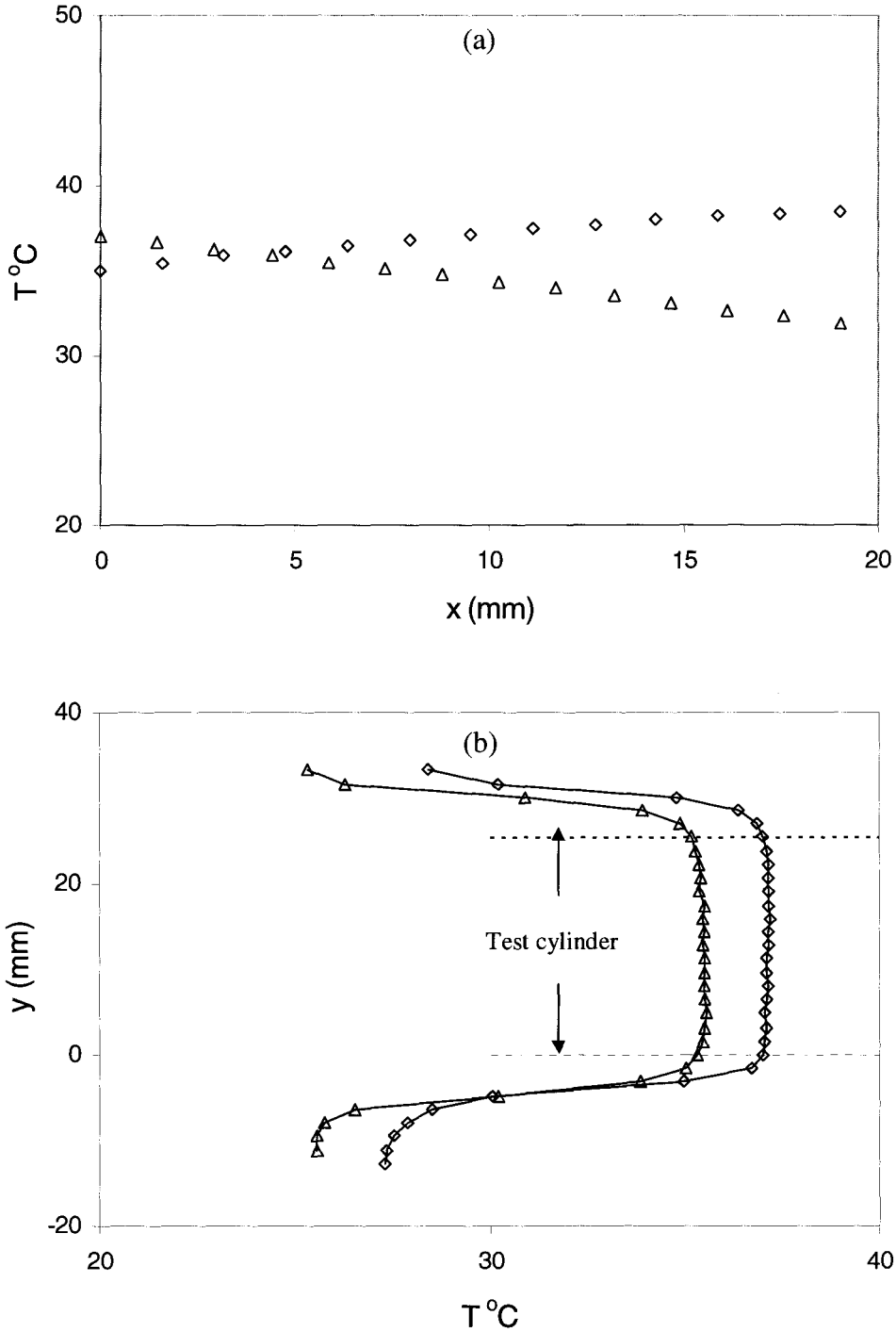

Figure 4.10: Typical temperature profiles measured on the black paint strips using the infrared camera for the smooth test section with a rotation speed of 418 rpm; (a) axial profiles, (b) vertical profiles (bottom of cylinder, y=0); ◊ left side, Δ right side.

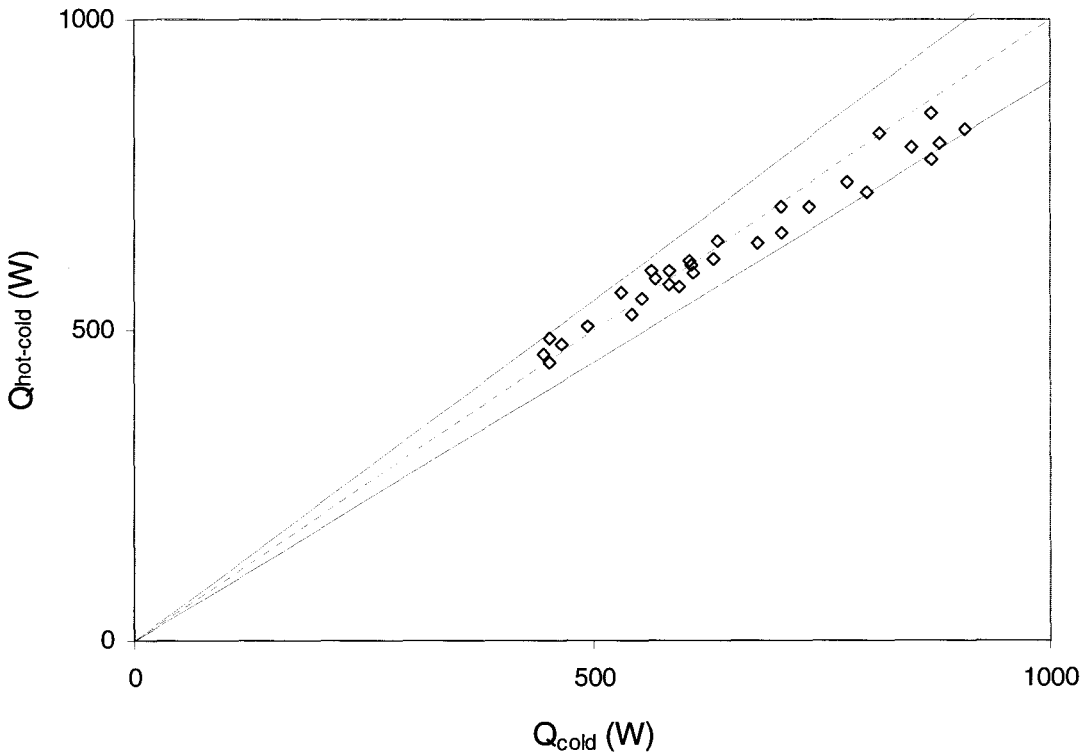

Figure 4.11: The energy balance for the tests with the smooth test cylinder. Solid lines indicate ±10%.

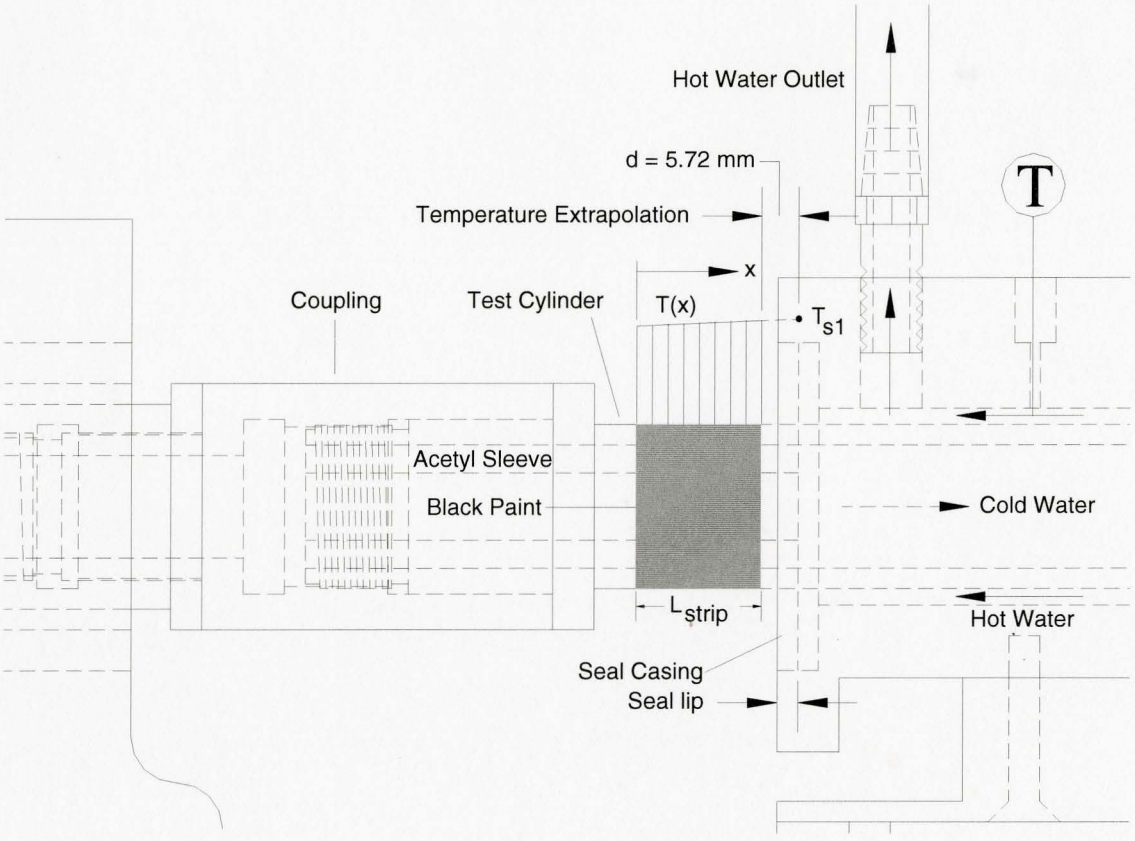

Figure 4.12: Schematic of the surface temperature profile on the test section.

that the conduction heat transfer along the wall of the test cylinder was adiabatic between the seal lip on the inside of the water jacket to the edge of the paint nearest the water jacket. The surface temperature T_{s1} is the extrapolated temperature and was estimated using

$$T_{s1} = T(L_{strip}) + \left(\left. \frac{\partial T}{\partial x} \right|_{jacket} \right) d, \tag{4.7}$$

where L_{strip} is the width of the paint strip and d is the distance from the edge of the paint to the inside of the seal lip. The same procedure was used to estimate the surface temperature on the other end of the test cylinder inside the water jacket. The extrapolated surface temperatures were typically 0.5°C to 0.9°C larger than the temperature measured at the edge of the paint.

The mean heat transfer coefficient on the outside of the test cylinder was then computed by (Incopera and DeWitt, 1996)

$$\bar{h} = \frac{Q_{cold}}{A \Delta T_{LM}}, \tag{4.8}$$

where A is surface area of the test cylinder in contact with the hot water and ΔT_{LM} is the log-mean temperature difference between the inlet and outlet of the jacket given by

$$\Delta T_{LM} = \frac{(T_{ho} - T_{s1}) - (T_{hi} - T_{s2})}{\ln\left(\frac{T_{ho} - T_{s1}}{T_{hi} - T_{s2}} \right)}. \tag{4.9}$$

Following Becker and Kaye (1962), the mean heat transfer coefficient was then used to compute the Nusselt number based on two gap heights for the test section given by

$$Nu = \frac{2\bar{h}\delta}{k_h}, \tag{4.10}$$

where δ is the gap height and k_h is the thermal conductivity of the hot water evaluated at the average temperature between the inlet and outlet of the water jacket. The variation of the Nusselt number was examined as a function of the modified Taylor number given by (Becker and Kaye, 1962)

$$Ta_m = \frac{\omega^2 r_m \delta^3}{\nu_h^2} \frac{1}{F_g}, \tag{4.11}$$

where ω is the rotation frequency, r_m is the average radius of the annular gap ν_h is the kinematic viscosity evaluated at the average temperature between the inlet and outlet of the water jacket and F_g is the geometric factor. Finally, the axial Reynolds number based on two gap heights for the flow in the annulus was computed from

$$\mathrm{Re}_x = \frac{2U\delta}{\bar{\nu}_h} = \frac{2\dot{m}_h}{\pi\rho\bar{\nu}_h(r_o + r_i)}, \tag{4.12}$$

where U is the mean axial velocity in the gap.

4.4 Experimental Uncertainty

The uncertainty of the measured and calculated quantities was estimated following Kline and McClintock (1953). The relative uncertainties of the important parameters in this investigation are summarized in table 4.1. The uncertainties of the fluid properties were estimated assuming the error in the temperature measurements was ±0.5°C, the same as the thermocouples. The dominant uncertainty in the mass flow rates

Table 4.1: The experimental uncertainty of important variables in this investigation.

PARAMETER	MAJOR SOURCE OF UNCERTAINTY	TYPICAL UNCERTAINTY
$\dot{m}_c$	Setting the flow meter.	± 3% (0.03 ± 0.0009 kg/s)
$\dot{m}_h$	Setting the rotameter.	± 1.8% - 3.8% (0.022 ± 0.00082 – 0.048 ± 0.00086 kg/s)
$\Delta T_c = T_{co} - T_{ci}$	Thermocouples.	± 0.71 °C
$\Delta T_h = T_{hi} - T_{ho}$	Thermocouples.	± 0.71 °C
ΔT_{LM}	Infrared camera.	± 1.1 °C
Q_{cold}	Temperature difference.	10% - 23%
Q_{hot}	Temperature difference.	10% - 32%
Ta_m	Misalignment.	21%
Re_x	Mass flow rate.	2% - 4%
Nu	Heat transfer rate.	15% - 20%

was from reading the scales on the meters during the experiments. The uncertainty in reading the rotameter scale in the hot-water loop and the flow meter scale in the cold-water loop were conservatively estimated at ± 0.5 and ± 1 scale division respectively. The uncertainty in the calibration of the rotameter and the flow meter was estimated to be less than 0.2% for each and was a negligible source of error. The uncertainty in the log-mean temperature difference was estimated by

$$u\Delta T_{LM} = \pm \frac{\sqrt{\delta T_s^2 + \delta T_T^2}}{\Delta T_{LM}}. \tag{4.13}$$

where δT_s = ± 1°C is the uncertainty of the surface temperature measurement using the camera and δT_T = ± 0.5°C is the uncertainty of the T-type thermocouples. The uncertainty of the heat transfer rates was typically 10% to 23% for the cold water and 10% to 32% for the hot water. The uncertainty in the heat transfer from the hot water

was larger than the uncertainty in the heat transfer to the cold water in several cases where the hot water flow rate was high and the temperature difference of the hot water across the jacket became small. The dominant source of uncertainty in the heat transfer rate was due to the temperature measurement. The large uncertainty in the Taylor number was due to its sensitivity to uncertainty in the gap height. The uncertainty of the gap height was a combination of the uncertainty of the radius of the test section, the bore diameter of the jacket and the misalignment between the jacket and the test cylinder after installation. The misalignment between the test section and the jacket was measured using a vernier scale with an accuracy of $\pm$ 0.0254 mm for each test cylinder after installation. The distance between the top surface of the test section and the top of the jacket on the left and right sides was never more than $\pm$ 0.13 mm. The uncertainty of the gap height was estimated at $\pm$ 0.18 mm. The uncertainty of the axial Reynolds number was 2% to 4% and the uncertainty of the gap size and mass flow rate were the largest contributing factors. Finally, the uncertainty in the Nusselt number was found to be 15% to 20%.

In all cases, the heat transfer to the cold water and the heat transfer from the hot water computed from the measurements agreed to within $\pm$ 10% that was lower than the estimated values from the uncertainty analysis. The uncertainty in the Nusselt number is likely less than that computed from the uncertainty analysis and it was thought that an uncertainty of $\pm$ 15% on the Nusselt number was more reasonable.

4.5 Experimental Results

The change of the Nusselt number with the modified Taylor number and axial Reynolds number for the smooth test cylinder for modified Taylor numbers of 10^6 to 5×10^7 is shown in figure 4.13. The Nusselt number increased by a factor of 2.5 over the modified Taylor number range and exhibited a log-linear dependence over most of the range. For modified Taylor numbers less than 3×10^6, the Nusselt number seemed to have a stronger Taylor number dependence than for higher modified Taylor numbers. Changes in the axial Reynolds number did not have a significant effect on the Nusselt number that was consistent with the results of Jakoby et al. (1998). A comparison of the results for the smooth test cylinder at an axial Reynolds number of 2080 to the results from Becker and Kaye (1962) and Jakoby et al. (1998) for axial Taylor Couette flow is shown in figure 4.14. The previous results were for air and so the Nusselt number was normalized by $\mathrm{Pr}^{1/3}$ following Arpaci and Kao (1997) to account for differences in the Prandtl number. The results obtained in the present study are in good agreement with the results of Jakoby et al. (1998) for an axial Reynolds number of 4000 and appear consistent with the results of Becker and Kaye (1962) for an axial Reynolds number of 2015 at lower Taylor numbers. The comparison indicated that the results obtained in this investigation were reasonable. The $Nu/\mathrm{Pr}^{1/3}$ results for the smooth test cylinder were fit using the least squares method in the form

$$\frac{Nu}{\mathrm{Pr}^{1/3}} = 0.65 Ta_m^{\,0.226}. \tag{4.14}$$

An axial Reynolds number dependence was not included because no evidence of an axial

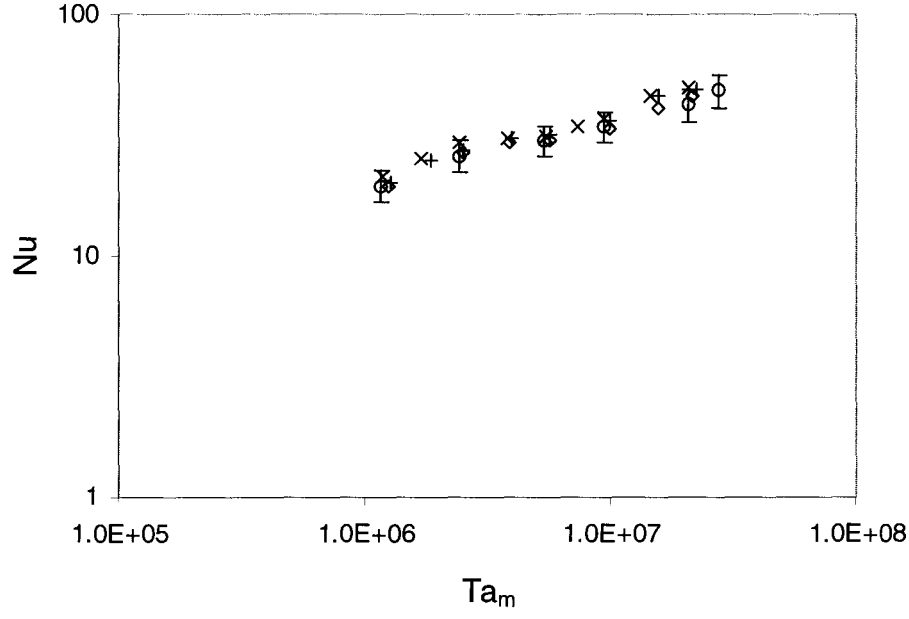

Figure 4.13: Change in the Nusselt number with modified Taylor number for the smooth cylinder. Re_x = o 950, ◊ 1240, + 1700, × 2080.

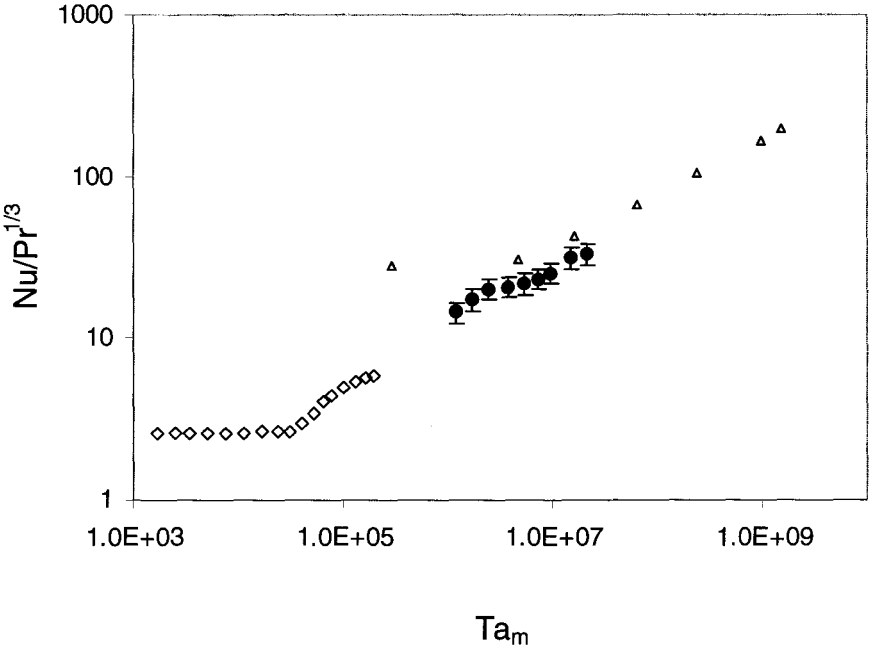

Figure 4.14: Change in the Nusselt number with modified Taylor number for the test cylinder with a smooth surface. Present study, Re_x = • 2080; ◊ Becker and Kaye (1962), Re_x = 2015; Δ Jakoby et al. (1998), Re_x = 4000.

Reynolds number dependence was found over the range of axial Reynolds numbers considered here.

The change in Nusselt number with modified Taylor number for the test section with axial grooves is shown in figure 4.15. The change in the Nusselt number with modified Taylor number and axial Reynolds number is similar to the smooth surface. The Taylor number dependence at the lower Taylor numbers appears to be larger in this case and it is not clear from the present investigation why this occurs. It could be because the angle of the mean flow relative to the axial grooves changes as the Taylor number increases. The angle of attack of the mean flow relative to the ribs was estimated as $\phi = \arctan\left(u_\theta / U\right)$ where u_θ is the speed of the outer surface of the test cylinder and U is the mean axial velocity of the flow. The angle of attack changed from 70° to 84° as the modified Taylor number increased for an axial Reynolds number of 2100. The angle of attack was found to be smaller, from 80° to 87°, for an axial Reynolds number of 920.

The change in Nusselt number with the modified Taylor number for the cylinder with cubic protrusions is shown in figure 4.16. The Nusselt number exhibited a similar trend to the previous test sections for the lower axial Reynolds number of 980. There is a different trend for the higher axial Reynolds number of 1950. In this case, the Nusselt number is relatively constant for modified Taylor numbers between 10^6 and 5×10^6. The Nusselt number increased at higher modified Taylor numbers and was similar to the lower axial Reynolds number. The change in the Nusselt number with the axial Reynolds number for a modified Taylor number of 1.1×10^6 is shown in figure 4.17. The Nusselt

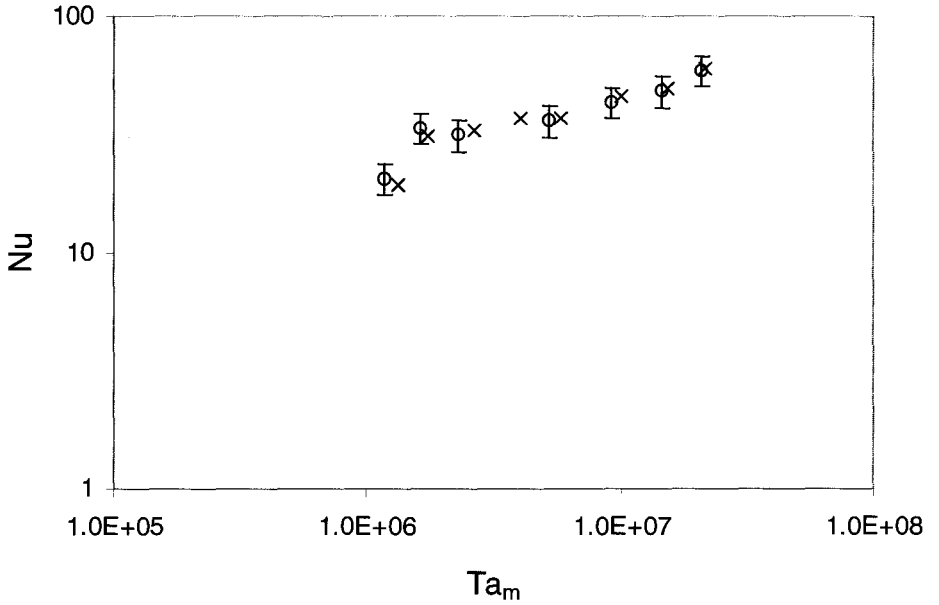

Figure 4.15: Change in the Nusselt number with modified Taylor number for the cylinder with axial grooves; Re_x = o 920, × 2100.

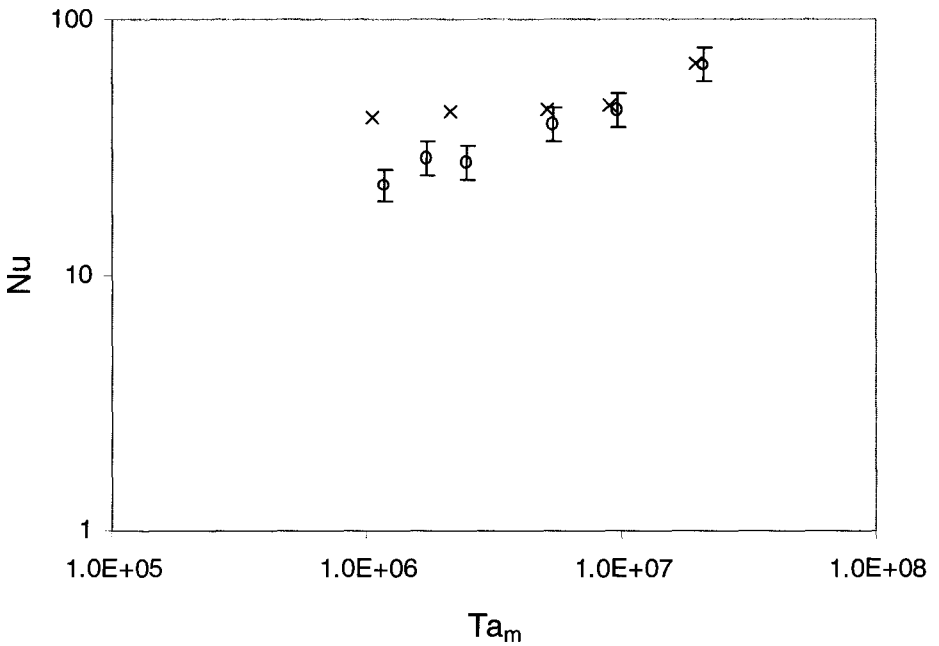

Figure 4.16: Change in the Nusselt number with modified Taylor number for the cubic protrusion cylinder. Re_x = o 980, × 1950.

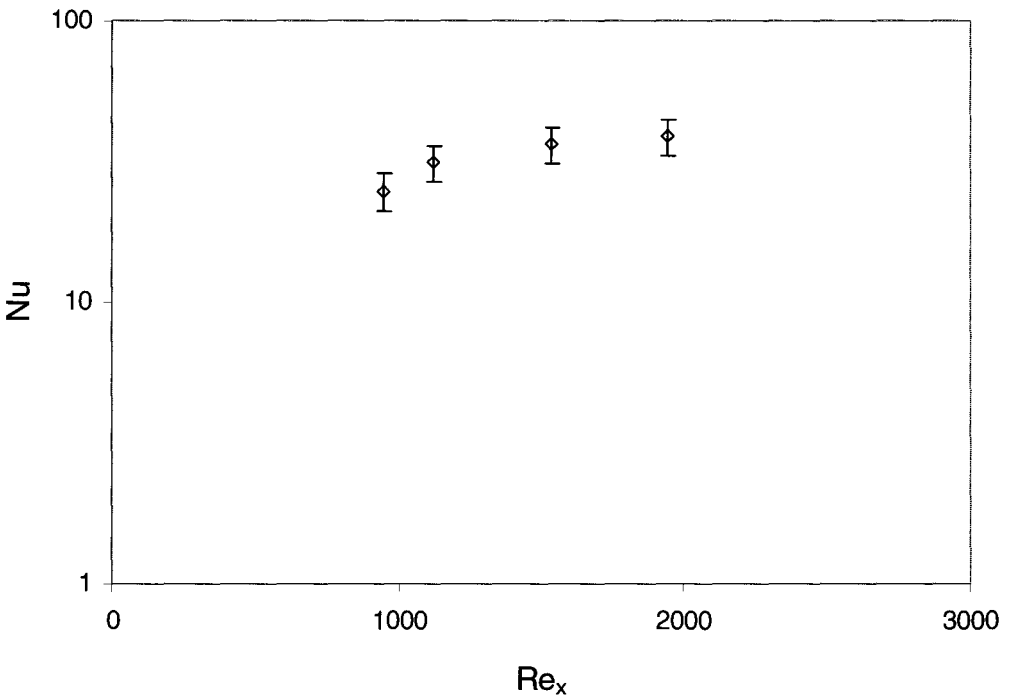

Figure 4.17: Change in the Nusselt number with axial Reynolds number for the cylinder with cubic protrusions at a modified Taylor number of 1.1×10^6.

number increased with the axial Reynolds number and the heat transfer results were found to be repeatable. The Nusselt number was normalized by $\mathrm{Pr}^{1/3}$ and a fit of the data using the least squares method is given by

$$\frac{Nu}{\mathrm{Pr}^{1/3}} = 10 Ta_m^{\,0.07}, \tag{4.15a}$$

for $10^6 \le Ta_m \le 9\times10^6$, when $\mathrm{Re}_x = 1950$ and

$$\frac{Nu}{\mathrm{Pr}^{1/3}} = 0.0152 Ta_m^{\,0.475}, \tag{4.15b}$$

for $Ta_m \ge 9\times10^6$.

The heat transfer enhancement that could be achieved using the axial grooves and the cubic protrusions was characterized by taking the ratio of the Nusselt number to that achieved from the smooth cylinder at similar modified Taylor numbers. The results are shown in figure 4.18. In figure 4.18a, it is clear that the test section with axial grooves enhanced the heat transfer by 5% to 35%. The enhancement increased with the modified Taylor number for each axial Reynolds number. In figure 4.18b, the surface with the cubic protrusions enhanced the heat transfer by 10% to 50% in a similar way to the surface with the axial grooves at an axial Reynolds number of 980. At an axial Reynolds number of 1950, the surface with cubic protrusions enhanced the heat transfer by nearly 100% at the lowest modified Taylor number of 10^6, which decreased to 35% at highest Taylor number.

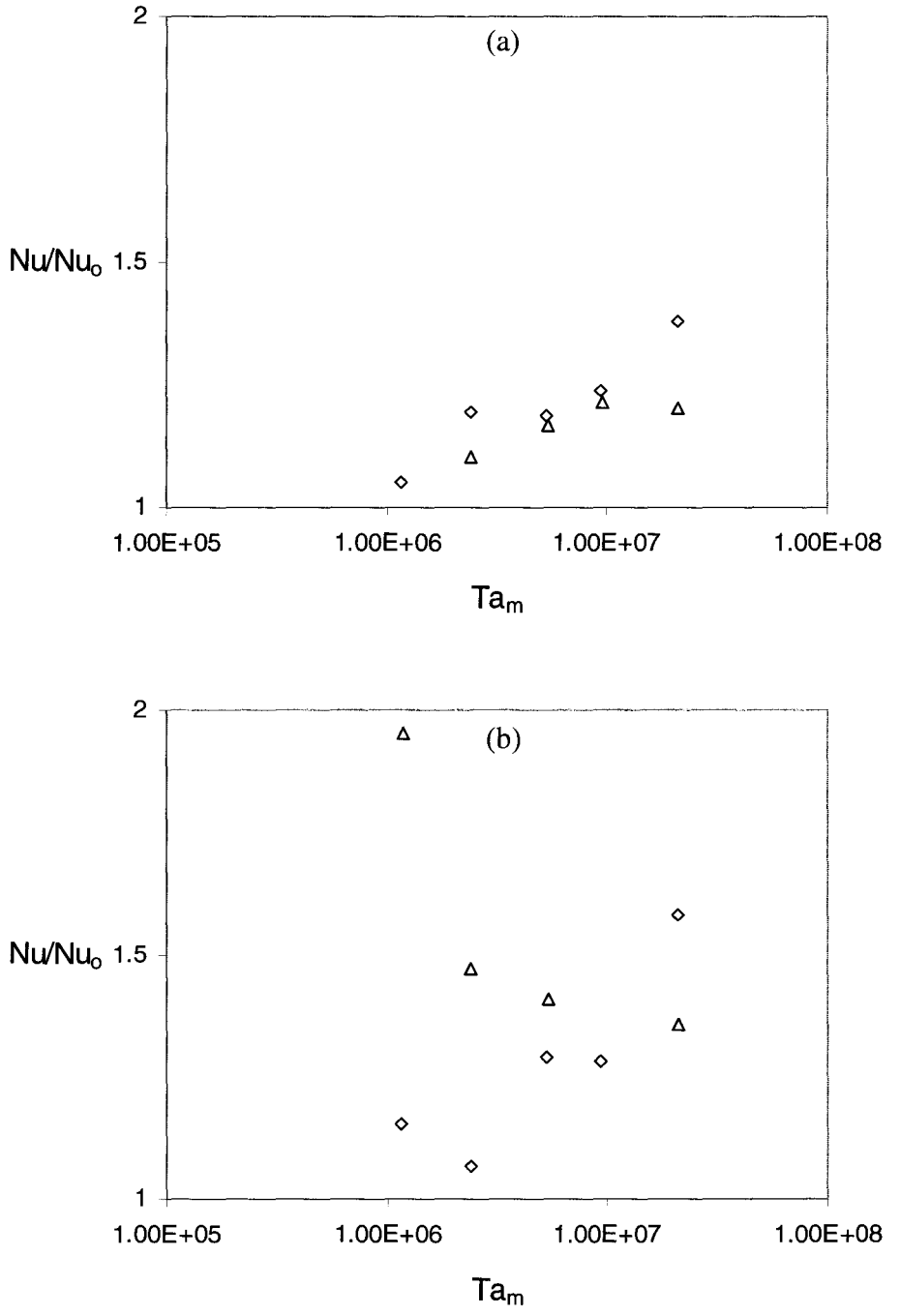

Figure 4.18: Ratio of the augmented surface Nusselt number to the smooth surface Nusselt number (Nu_0): (a) surface with axial grooves, Re_x = ◊ 920, Δ 2100; (b) surface with cubic protrusions, Re_x = ◊ 980, Δ 1950.

Chapter 5 Performance of the Proposed Anti-icing System

The performance of the proposed anti-icing system was first examined for a basic design where conduction through the polycrystalline graphite filler and the end wall of the heat pipe were used to heat the nose cone. A rotating heat pipe with a smooth exterior surface was used at the evaporator and its heat transfer coefficient was modeled using the correlation given in equation (4.14). The engine oil lubricant MIL-L-23699 was used as the working fluid. The effect of adding the heating channels in the condenser and passive heat transfer enhancement in the evaporator were considered later. The extended surface in the evaporator included inline three-dimensional cubic protrusions on the outside of the rotating heat pipe. An axial Reynolds number for the flow in the gap of 1950 was used so that the heat transfer coefficient could be modeled using equation (4.15).

In all cases, the continuous icing spectrum outlined by the FAA was used to model the atmospheric conditions. The liquid water content was evaluated assuming a mean effective drop diameter of 15 microns. The anti-icing system model results encompass a range of engine and air speeds typical of climbing, cruising and descent for a small turbo-fan powered aircraft outlined previously. The particular geometry used for the nose cone and the rotating heat pipe evaporator and condenser sections is given in figure 5.1 and table 5.1. The geometry is characteristic of an anti-icing system that could fit in a small turbo-fan engine.

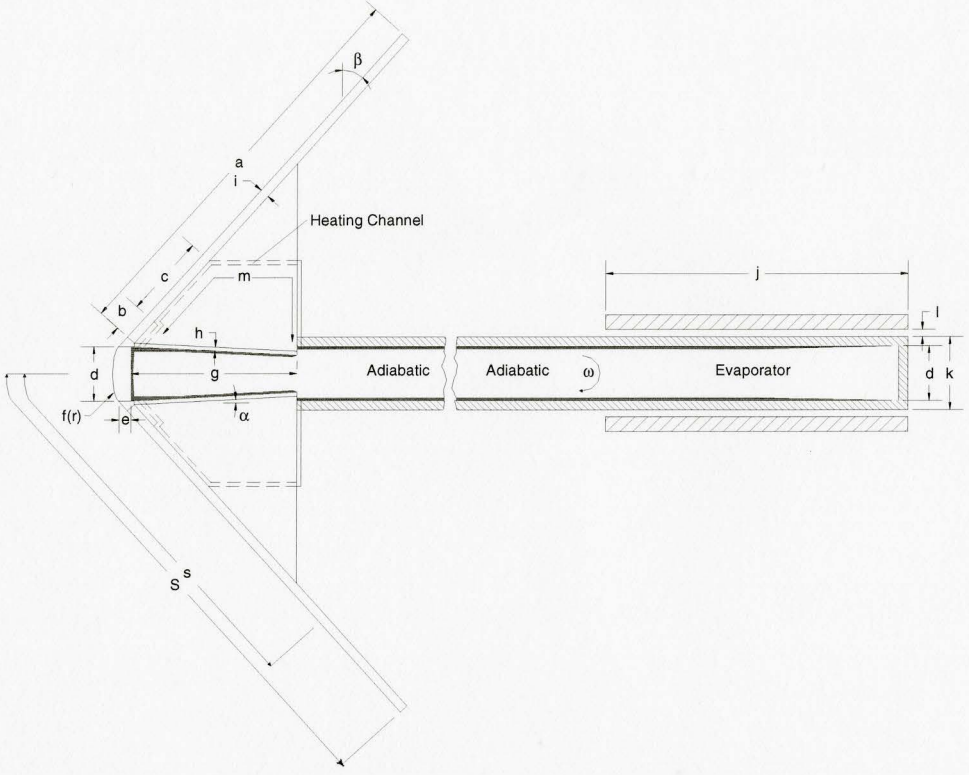

Figure 5.1: Anti-icing system geometry.

Table 5.1: Summary of dimensions used in the results.

DIMENSION	DESCRIPTION	VALUE	
		SI (mm)	Imperial (in.)
a	Length of nose cone shell.	142	5.6
b	Length of channel before contact.	10	0.39
c	Length of channel contact.	28.5	1.1
d	Major diameter of condenser.	19.05	0.75
e	End wall thickness at the junction.	4.25	0.17
f(r)	Heat pipe end wall thickness profile.	$f(r)=C_1\left(1-\frac{r^2}{C_2^2}\right)^{1/2}+C_3$ $f(0)=6.35mm, f\left(d/2\right)=e, f'\left(d/2\right)=-\tan(\beta)$	
g	Length of condenser.	57.15	2.25
h	Thickness of tapered fin.	1.27	0.05
i	Thickness of nose cone shell.	3.18	0.125
j	Length of evaporator.	101.6	4
k	Outer diameter of heat pipe.	25.4	1
l	Gap height in evaporator jacket.	2.54	0.1
m	Total length of one heating channel.	98.9	3.89
S,s	Arc-length and local coordinate.	S = 155.4	S = 6.1
α	Taper angle of condenser.	1° - 7°	
β	Half-angle of nose cone shell.	42°	

5.1 Baseline Performance

The performance of the baseline case was initially examined by considering the effect of the taper angle in the condenser. The taper angle in the condenser affects the performance of the system because a higher angle increases the centrifugal forces driving the liquid film thinning and reducing its thermal resistance. However, increasing the taper angle also reduces the heat transfer surface area and potentially the overall heat transfer. Following Song et al. (2003b), the effect of the taper angle of the wall on the total heat transfer was examined by varying this angle for a range of conditions. The results for two vapour temperatures are shown in figure 5.2. A taper angle of 3° provided the maximum heat transfer when water was the working fluid and so this taper angle was used throughout the investigations for water. When ethanol was the working fluid, the angle that maximized the heat transfer was 4° and this was used in subsequent computations for ethanol. The model suggests that the performance is relatively independent of taper angle for modest variations about these values.

The total heat transfer rate in the evaporator and condenser was then characterized as a function of the vapour temperature as shown in figure 5.3 for several engine rotation speeds at ambient temperatures of -5°C and -30°C and an airplane speed of 300 km/h. The intersection of the evaporator and condenser curves denoted by the darker curve fit represents the equilibrium point where an overall energy balance in the system is achieved. The procedure was repeated for ambient temperatures of -10°C and -20°C to cover the intermediate range of the icing conditions. The change in the heat transfer and the vapour temperature with the engine rotation speed for different ambient temperatures

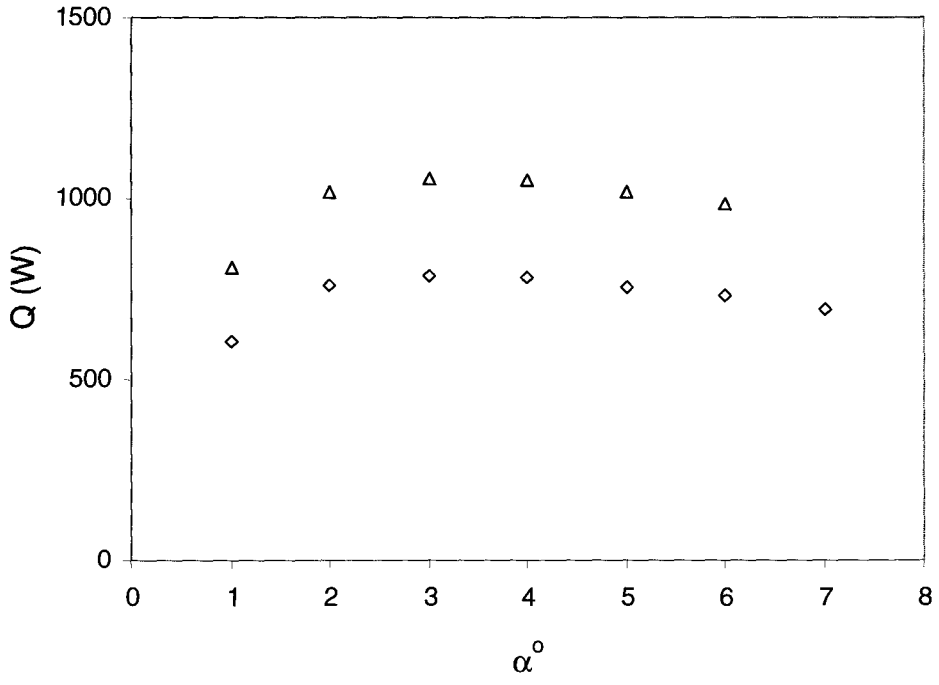

Figure 5.2: Heat transfer in the condenser for vapour temperatures of ◊ 30°C, Δ 50°C using water with 10 heating channels when ω = 5000 rpm, T_{inf} = -30°C and U_{plane} = 300 km/h.

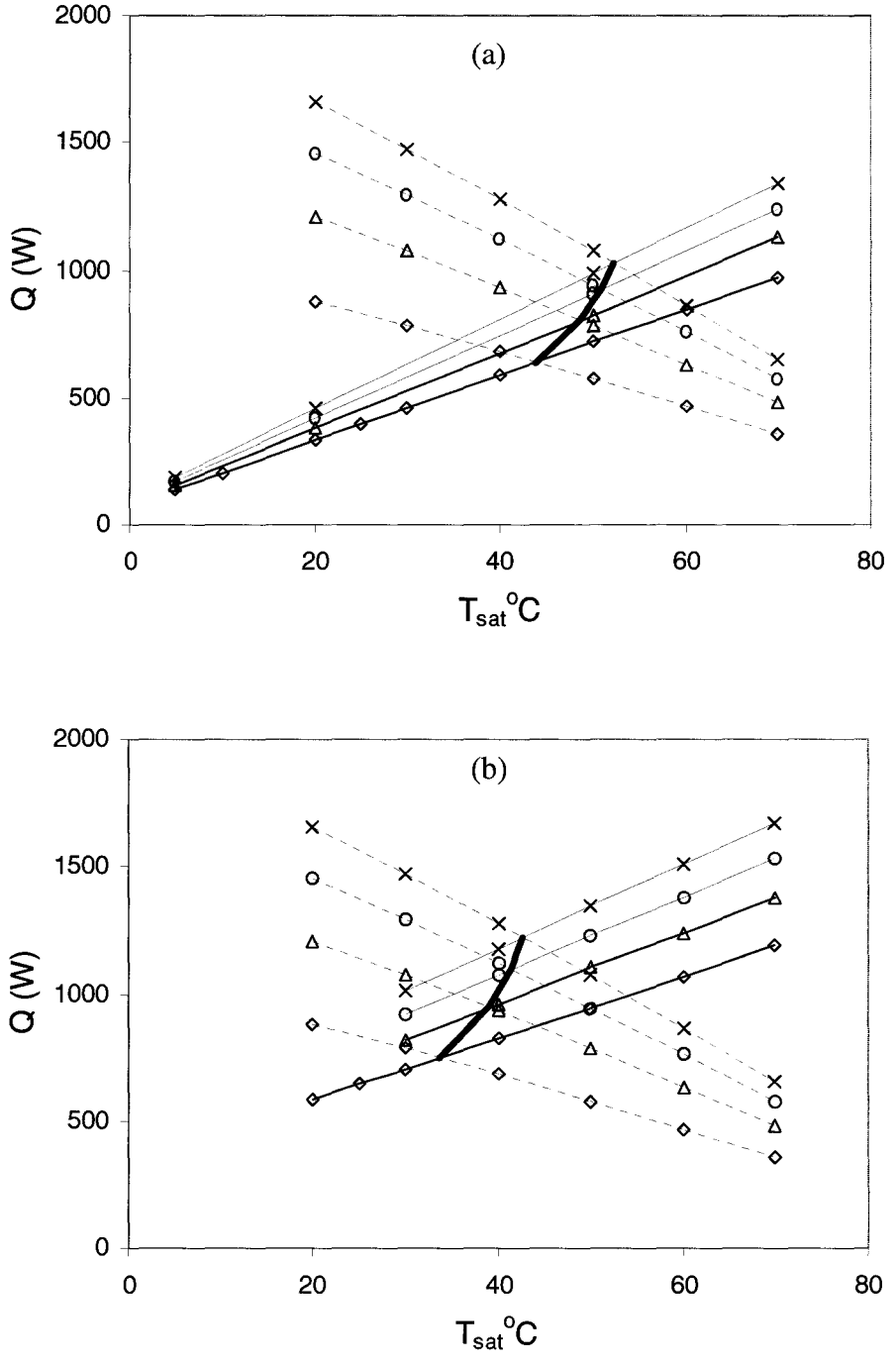

Figure 5.3: Heat transfer in the --- evaporator, — condenser for ambient temperatures of (a) -5°C, (b) -30°C and ω = ◊ 5000 rpm, Δ 10000 rpm, o 15000 rpm, × 20000 rpm when U_{plane} = 300 km/h.

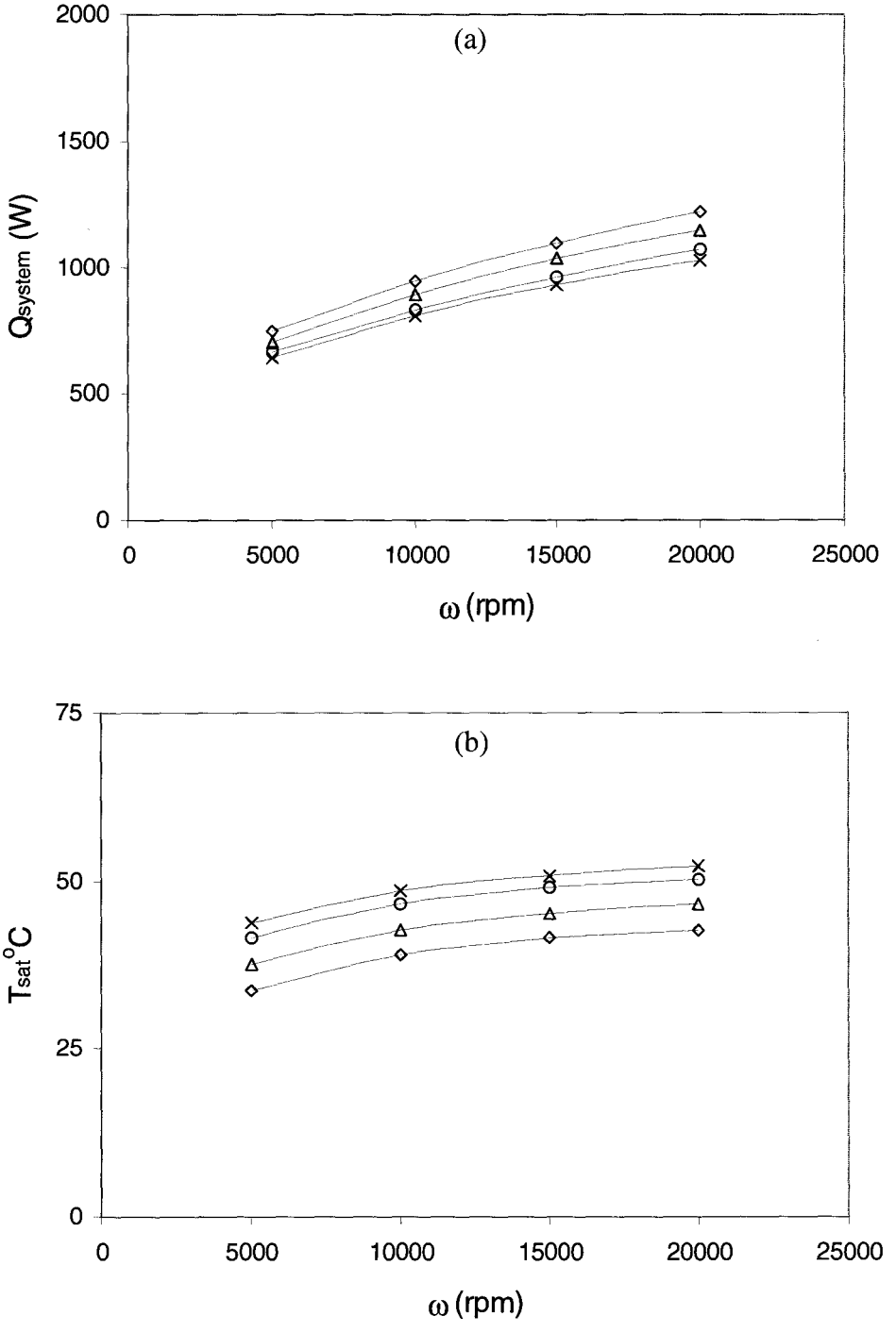

Figure 5.4: Change in (a) system heat transfer, (b) vapour temperature for T_{inf} = × -5°C, o -10°C, Δ -20°C, ◊ -30°C and U_{plane} = 300 km/h.

are shown in figure 5.4. The anti-icing system performance was evaluated at the vapour temperatures corresponding to the equilibrium points. It is clear that the heat transfer rate increased with engine speed and as the ambient temperature decreased, as expected.

The region of the nose cone that could be effectively heated by conduction was determined by examining the temperature profiles along the surface of the nose cone shown in figure 5.5. The temperature profiles are plotted as a function of s/S, or the local arclength from the pole of the nose cone relative to the total arclength of the nose cone along a meridian. As the ambient temperature decreased, the surface temperature decreased and the curves were shifted vertically. Over the first portion that corresponds to the region outside of the end wall of the heat pipe, the surface temperature typically decreased by up to 5°C. The temperature profile over the region in contact with the polycrystalline graphite filler decreased gradually compared to the rapid decrease over the remaining portion not in contact with the filler. The portion of the nose cone maintained above 0°C was used here as a first estimate of the region of the nose cone that could be anti-iced. The location where the surface temperature fell below 0°C moved from 75% of the arclength of the nose cone to half of the nose cone as the ambient temperature decreased from -5°C to -30°C.

The surface temperature of the nose cone for a range of engine speeds at an ambient temperature of -30°C is shown in figure 5.6. The surface temperature on the nose cone increased as the rotation speed increased because the overall heat transfer through the system increased. This was most prominent in the regions in contact with the

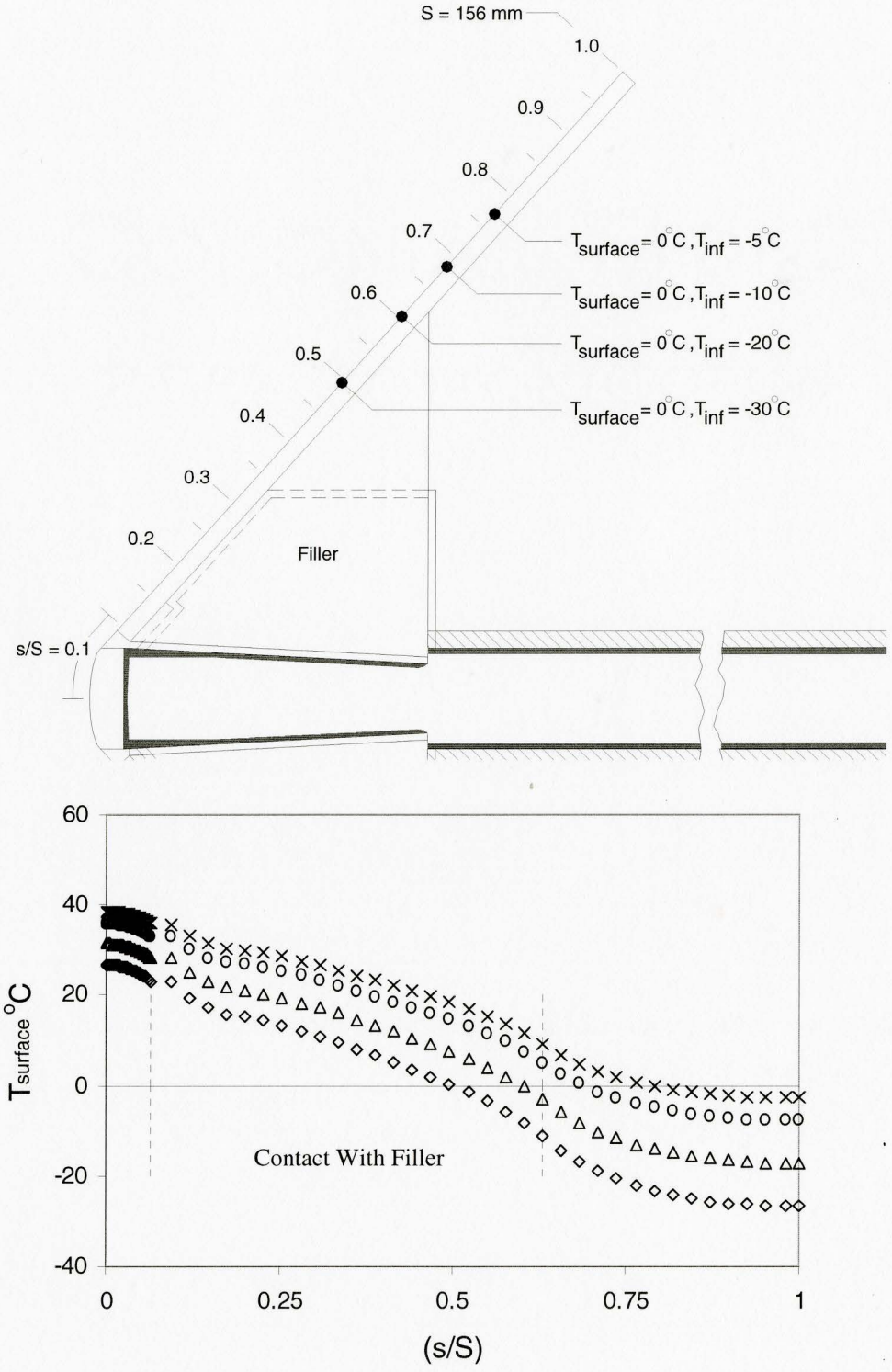

Figure 5.5: Surface temperature on the nose cone for T_{inf} = × -5°C, o -10°C, Δ -20°C, ◊ -30°C when ω = 5000 rpm and U_{plane} = 300 km/h, using water.

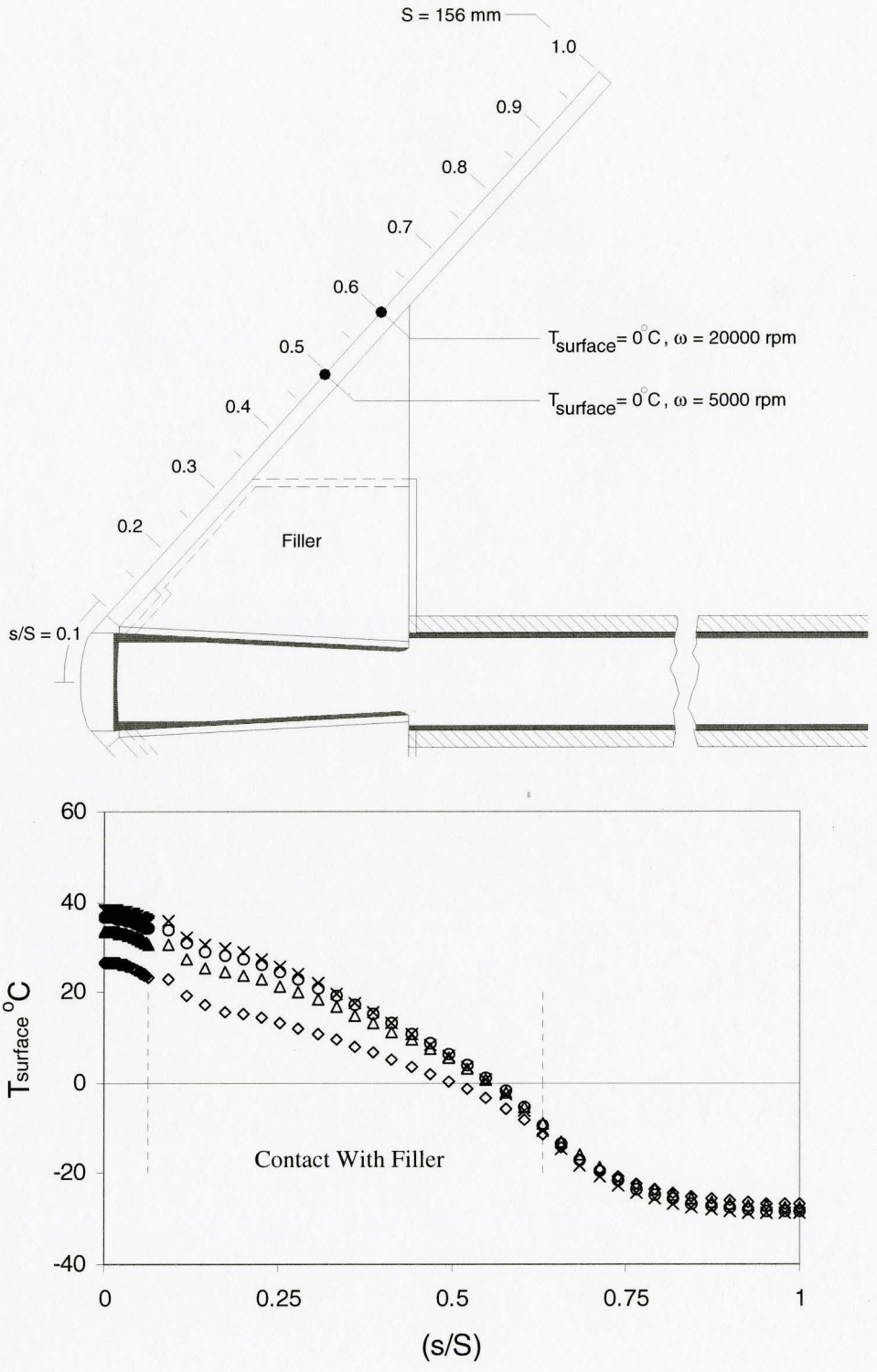

Figure 5.6: Surface temperature on the nose cone for ω = ◊ 5000 rpm, Δ 10000 rpm, o 15000 rpm, × 20000 rpm and U_{plane} = 300 km/h using water as the working fluid.

polycrystalline graphite and the end of the heat pipe. The arclength of the nose cone maintained above 0°C did not, however, increase that significantly as the engine speed increased.

The change in the heat transfer performance of the system when the engine speed was increased to 600 km/h is shown in figure 5.7 for ambient temperatures of -5°C and -30°C. The heat transfer rate through the system increased by about 10% when the airplane speed increased from 300 km/h to 600 km/h, in large part because the heat transfer coefficient of the flow over the nose cone increased. The heat transfer coefficient outside of the nose cone for these cases is shown in figure 5.8. The increase in the heat transfer coefficient increased the heat transfer through the system that decreased the temperature of the nose cone as shown in figure 5.9. This was particularly prominent for the lower engine rotation speeds. For example, at 5000 rpm, about 20% of the nose cone was maintained above 0°C when the ambient temperature was -30°C and the airplane speed was 600 km/h. The airplane speed had a smaller effect as the engine speed increased because the performance of the system improved and because the heat transfer from the nose cone to the ambient is increasingly determined by the rotation speed of the surface.

The heat transfer through the system when ethanol was used as the working fluid is shown in figure 5.10. The results for water are also included for comparison. The heat transfer rate was 35% to 45% smaller when ethanol was used. The ethanol causes a higher thermal resistance in the heat pipe because it has a smaller thermal conductivity than water so it requires a larger temperature difference across the films in the condenser.

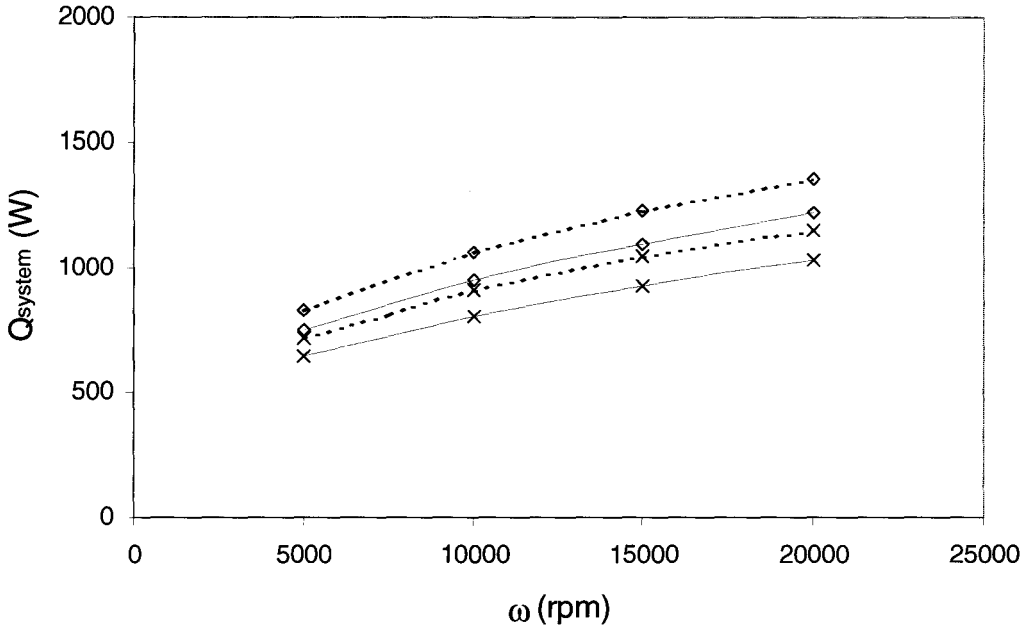

Figure 5.7: Heat transfer through the anti-icing system for U_{plane} = — 300 km/h, ---- 600 km/h when T_{inf} = × -5°C, ◊ -30°C using water as the working fluid.

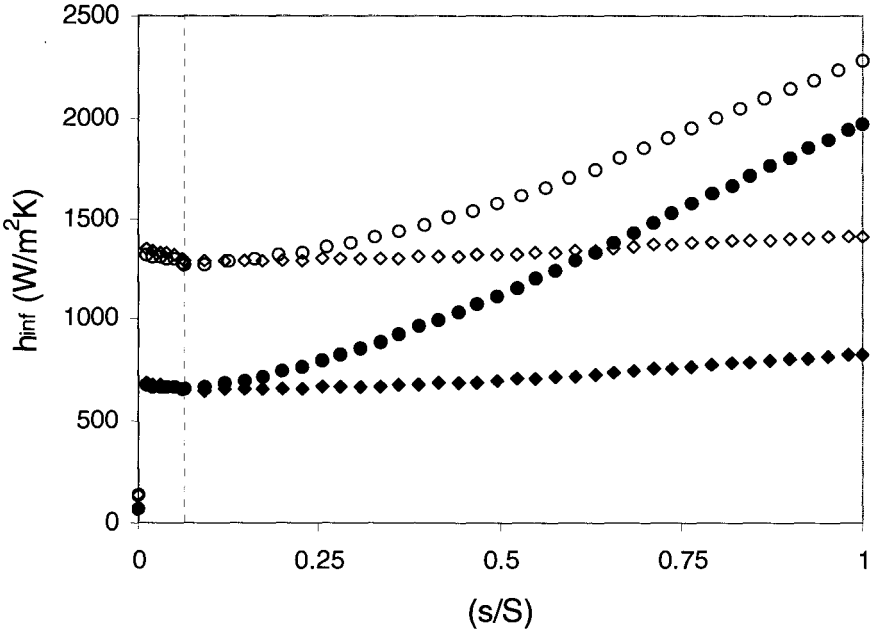

Figure 5.8: Heat transfer coefficient of the flow over the nose cone for U_{plane} = 300 km/h when ω = ♦ 5000 rpm, • 20000 rpm and for U_{plane} = 600 km/h when ω = ◊ 5000 rpm, o 20000 rpm and T_{inf} = -30°C.

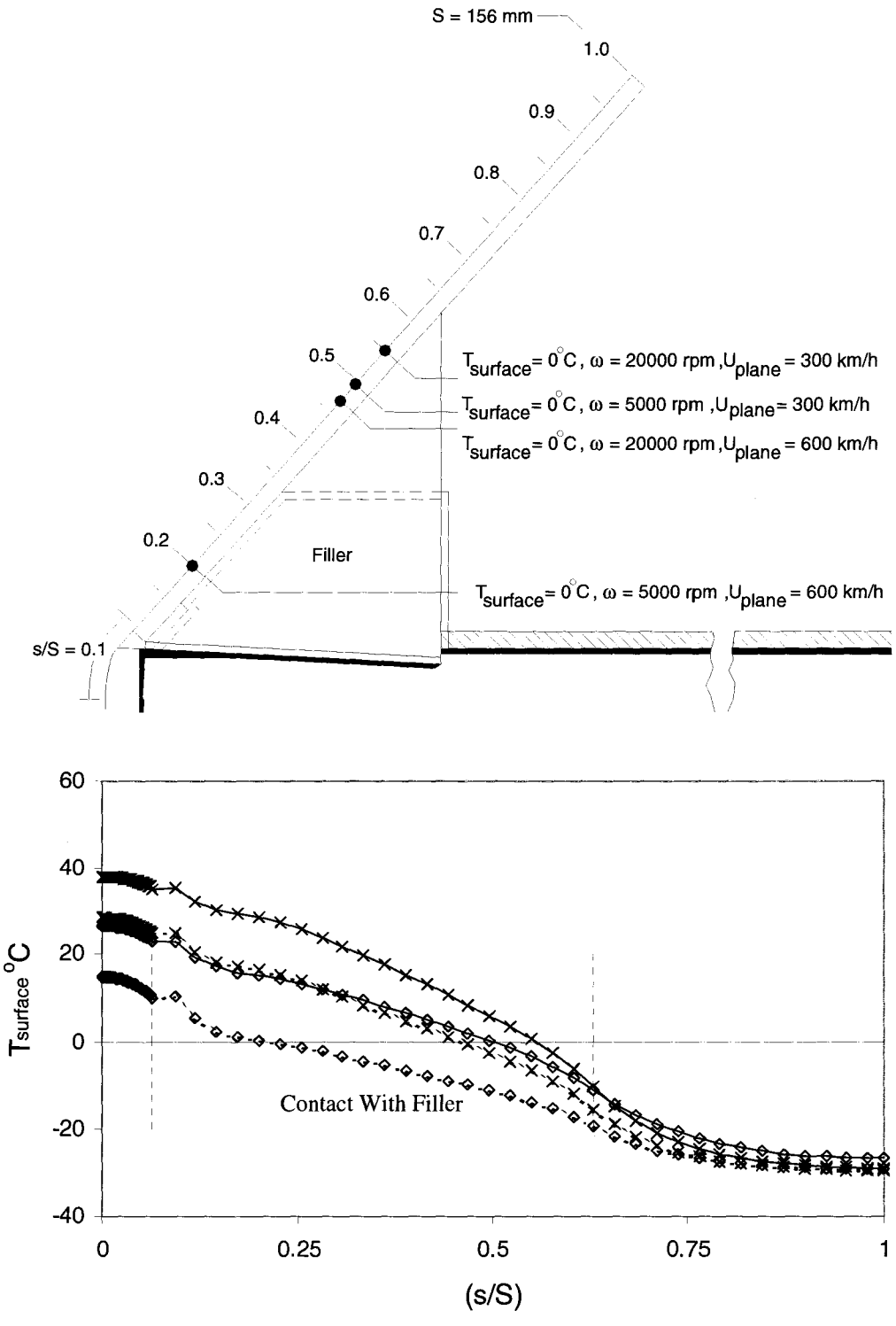

Figure 5.9: Surface temperature of the nose cone for U_{plane} = — 300 km/h, --- 600 km/h when ω = ◊ 5000 rpm, × 20000 rpm and T_{inf} = - 30°C using water as the working fluid.

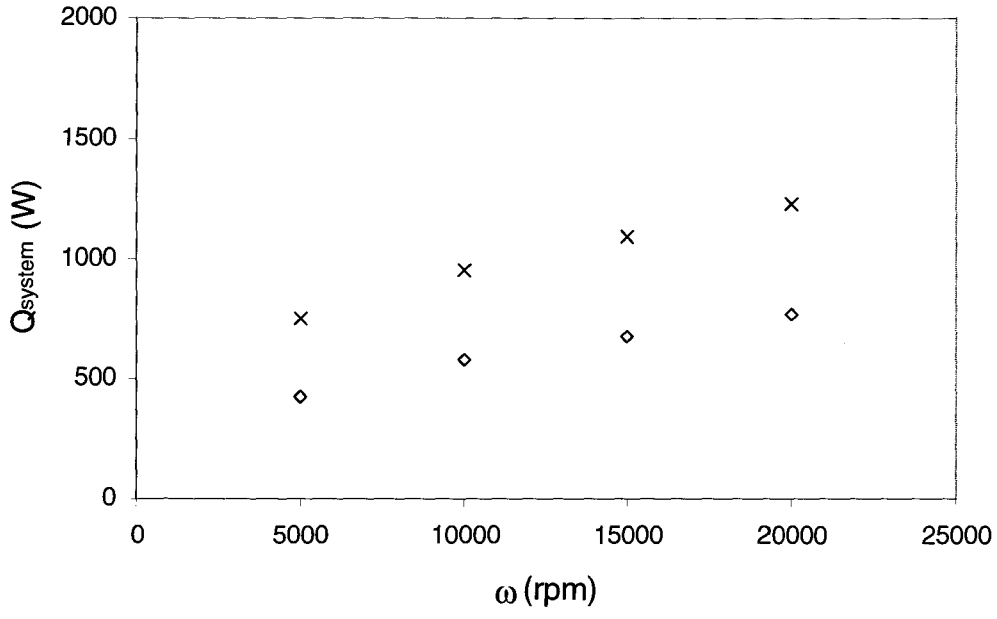

Figure 5.10: Comparison of the heat transfer through the anti-icing system when × water and ◊ ethanol were used as the working fluid for T_{inf} = -30°C and U_{plane} = 300 km/h.

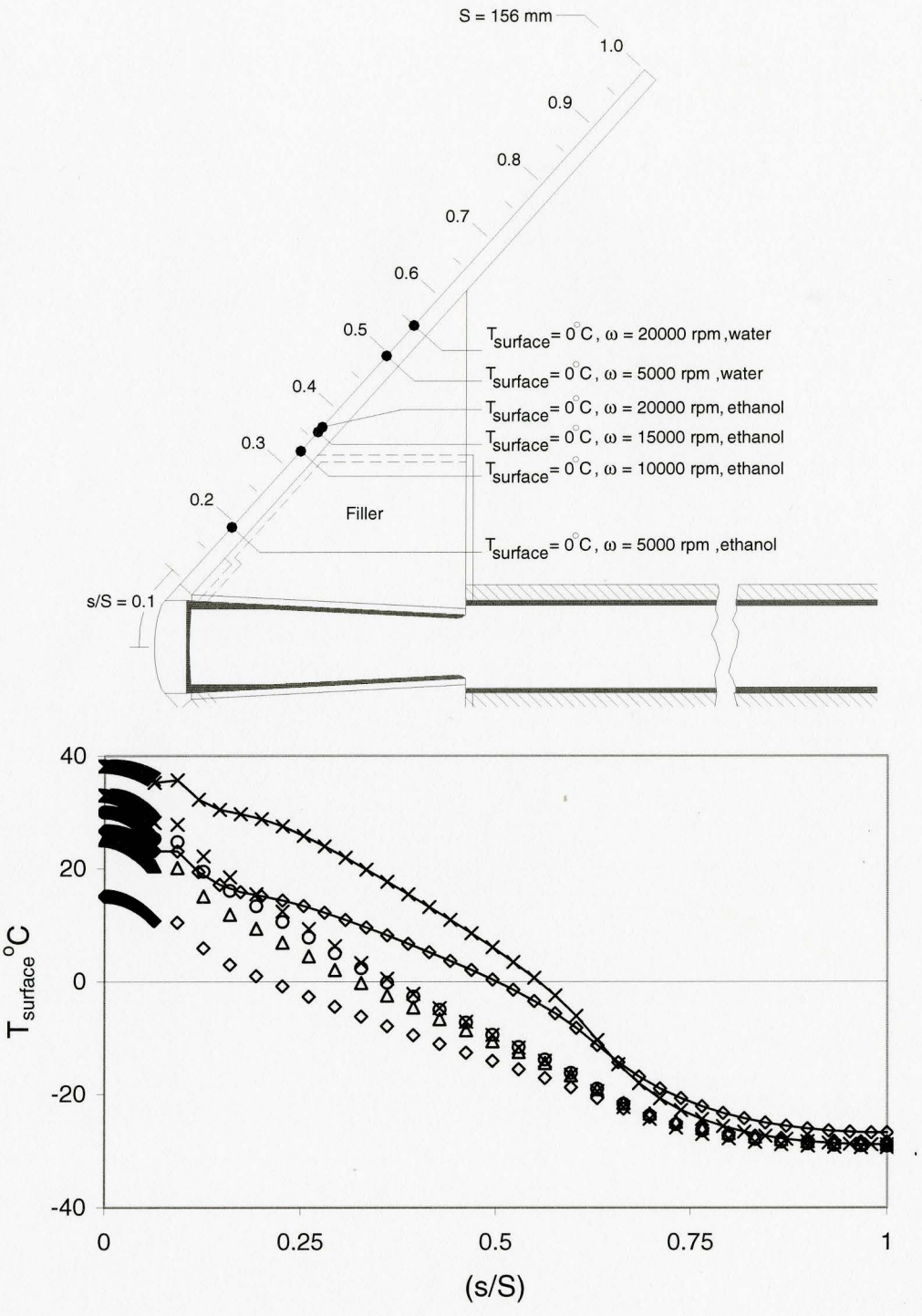

Figure 5.11: Surface temperature of the nose cone when ethanol was the working fluid for ω = ◊ 5000 rpm, Δ 10000 rpm, o 15000 rpm × 20000 rpm and for water as the working fluid at ω = —◊—5000 rpm, —×— 20000 rpm when T_{inf} = -30°C and U_{plane} = 300 km/h.

In this case the vapour temperature increased by 9°C to 6°C as the engine speed was increased using ethanol instead of water. The temperature profiles on the nose cone surface for these cases are shown in figure 5.11. The portion of the surface of the nose cone maintained above 0°C decreased by about 50% for an engine speed of 5000 rpm and by about 35% for an engine speed of 20000 rpm when ethanol was used as the working fluid instead of water. Despite this, approximately 25% of the arclength along the nose cone surface was maintained above 0°C using ethanol. Ethanol would be advantageous in this low temperature application because it would not freeze during start-up.

The performance of the condenser section can be understood further by examining how the heat transfer is distributed throughout the region. The heat transfer distribution for typical cases is summarized in figure 5.12 and table 5.2 for the both water and ethanol as the working fluid. Although the total heat transfer rate through the system was about 40% smaller when ethanol was used as the working fluid, it is clear that the distribution of heat transfer throughout the condenser design is similar for both working fluids. The results show that 80% to 95% of the total condensation heat transfer occurred on the tapered wall of the rotating heat pipe. The majority of this heat was conducted directly to the nose cone shell through the polycrystalline graphite filler. This suggests that polycrystalline graphite or a similar composite does provide an effective means to heat the nose cone in the practical application. A small amount of heat transfer occurred from the nose cone into the tapered wall of the condenser for the cases investigated here. This is undesirable because it inhibits the condensation heat transfer on the tapered wall but the effect was small in this design. The condenser performance could be marginally

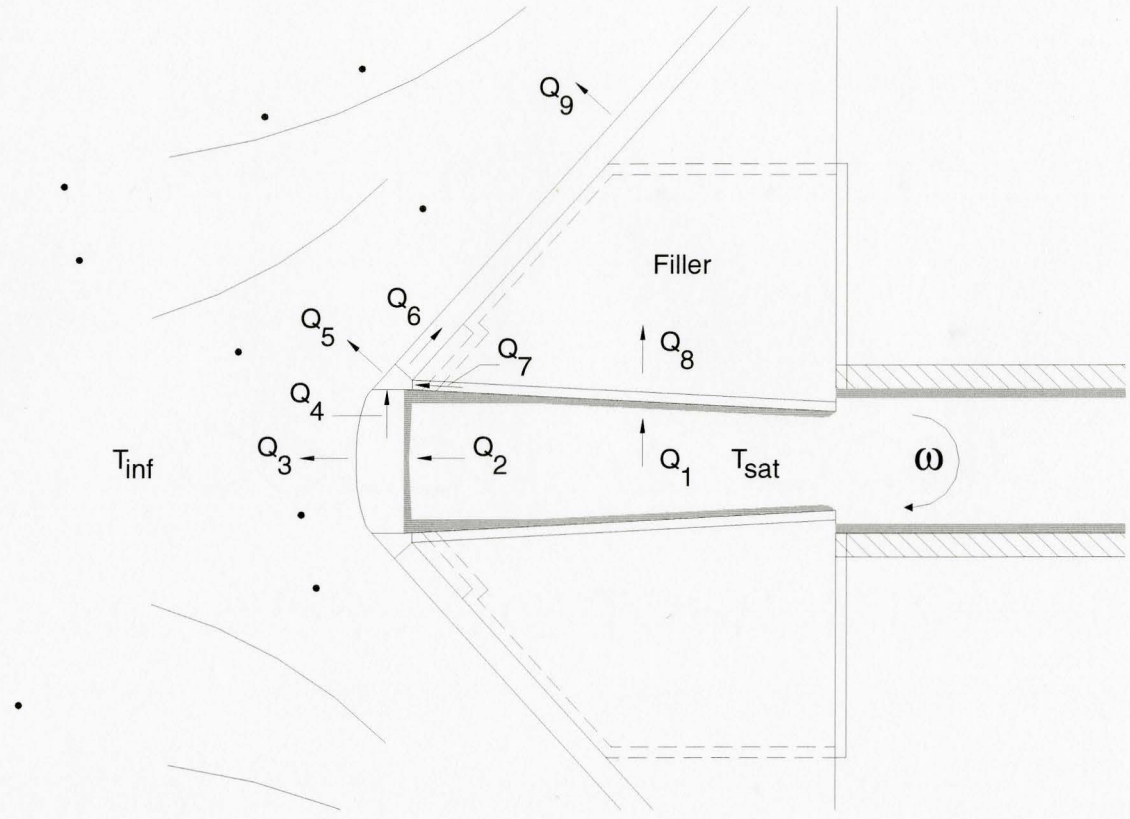

Figure 5.12: Schematic of heat transfer distribution in the condenser.

Table 5.2: Distribution of heat transfer in the condenser for T_{inf} = -30°C and U_{plane} = 300 km/h.

HEAT TRANSFER (W)	WATER		ETHANOL	
	5000 rpm	20000 rpm	5000 rpm	20000 rpm
Q_1	665 (89%)	1141 (94%)	348 (82%)	663 (87%)
Q_2	83 (11%)	79 (6%)	78 (18%)	101 (13%)
Q_3	11	13	9	12
Q_4	72	65	69	88
Q_5	11	14	8	12
Q_6	41	43	39	49
Q_7	-19	-20	-19	-24
Q_8	685	1161	368	688
Q_9	723	1195	410	741
Q_{SYSTEM}	**749**	**1220**	**426**	**764**

improved by insulating the tapered wall from the nose cone. The condensation heat transfer on the end wall of the heat pipe was comparatively small and almost all of this heat was transferred along the nose cone by conduction. Thus the tip of the nose cone was heated sufficiently without significant heat losses to the flow over the nose cone in this region.

The distribution of mass flow in the condenser is shown in figure 5.13. The total mass flow in the condenser was 0.3 g/s to 0.5 g/s using water as the working fluid and 0.4 g/s to 0.75 g/s using ethanol. The ethanol films were thicker because its latent heat of vapourization was significantly less than that of water. Consequently more mass had to be condensed to balance the heat transfer to the nose cone. The film thickness on the end wall was 2 μm to 7 μm for water and 5 μm to 13 μm for ethanol and the thickness was relatively constant over the radius of the end wall. The film thickness on the tapered wall increased rapidly over the first 15% of the condenser length and then remained fairly constant until it reached the pool because the thermal resistance increased with the film thickness. In this case the maximum film thickness was 10 μm to 40μm for water and 25 μm to 50 μm for ethanol as the working fluid. Both films decrease in thickness and thermal resistance as the engine speed increased because the centrifugal driving forces increased.

5.2 Effect of Heating Channels

The results suggest that a significant portion of the front of the nose cone could be maintained above 0°C during continuous icing using conduction with water or ethanol as

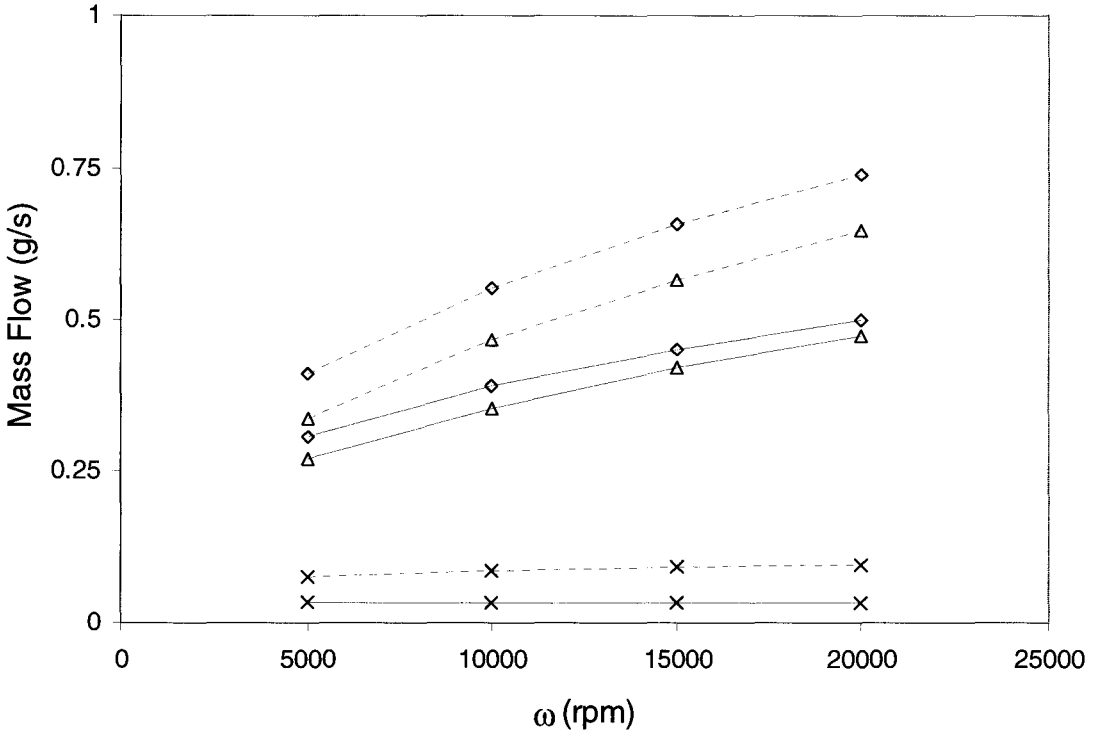

Figure 5.13: Mass flow from the × end wall of heat pipe, the Δ tapered wall and the ◊ total mass flow in the condenser region for —— water and ---- ethanol as the working fluid for T_{inf} = -30°C and U_{plane} = 300 km/h.

the working fluid in the rotating heat pipe. It was thought that adding heating channels to the inside of the nose cone surface could extend this region further. The heating channels were brought into contact with the nose cone at an arclength of approximately s/S = 0.16 and remained in contact with the nose cone until s/S = 0.33 in an attempt to maintain the first one-third of the nose cone above 0°C under all continuous icing conditions.

The hydraulic diameter of the proposed heating channels had to be large enough to ensure they did not cause too large a pressure drop that would increase the pool depth in the condenser and reduce its performance. Initial calculations were performed to estimate the potential designs of the heating channel system. The effect of the hydraulic diameter of the heating channels on the length of the condenser covered by the pool for the case of 10 channels is shown in figure 5.14. A hydraulic diameter of 0.9mm minimized the length of the condenser covered by the pool when the taper angle was 2° to 7° and was slightly smaller at 0.8 mm when the taper angle was 1°. Increases in the hydraulic diameter beyond these values caused the pool height to increase because the difference in the radius between the pool and the channel outlet driving the flow decreased. The hydraulic diameter that minimized the length of the condenser covered by the pool also changed depending on the number of heating channels in the nose cone as shown in figure 5.15. This hydraulic diameter decreased as the number of channels increased from 5 to 500 because the mass flow rate per channel decreased.

The heat transfer performance of the system was evaluated for designs with 10, 50 and 100 heating channels when water was used as the working fluid for an engine rotation speed of 5000 rpm, an ambient temperature of -30°C and an airplane speed of

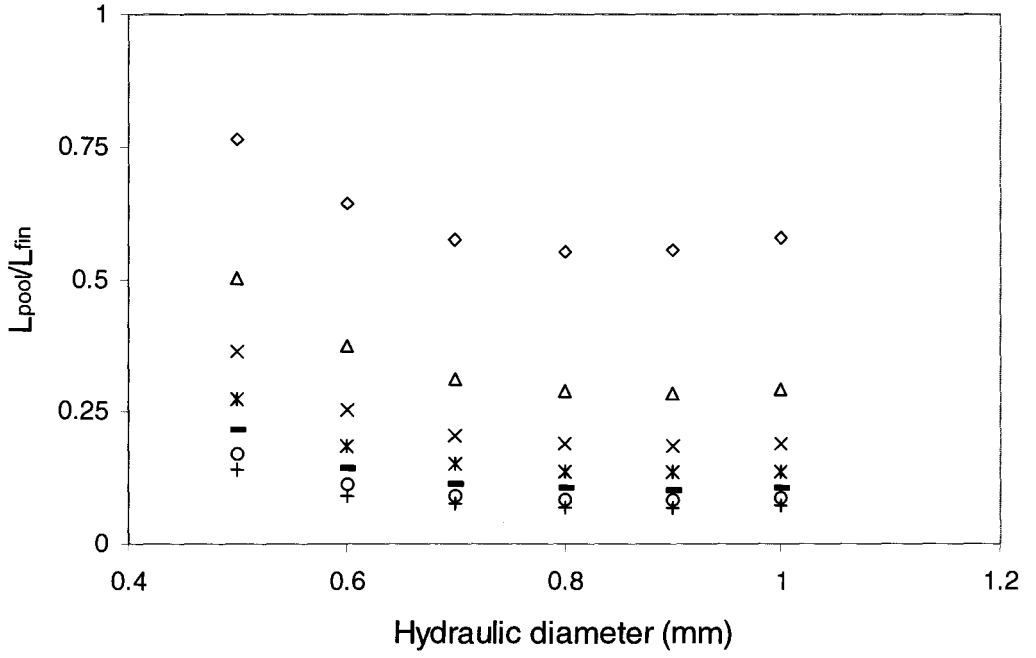

Figure 5.14: Length of the condenser covered by the pool using water and 10 heating channels for taper angles of α = ◊ 1°, Δ 2°, × 3°, * 4°, – 5°, o 6°, + 7° when ω = 5000 rpm, T_{sat} = 30°C, T_{inf} = -30°C and U_{plane} = 300 km/h.

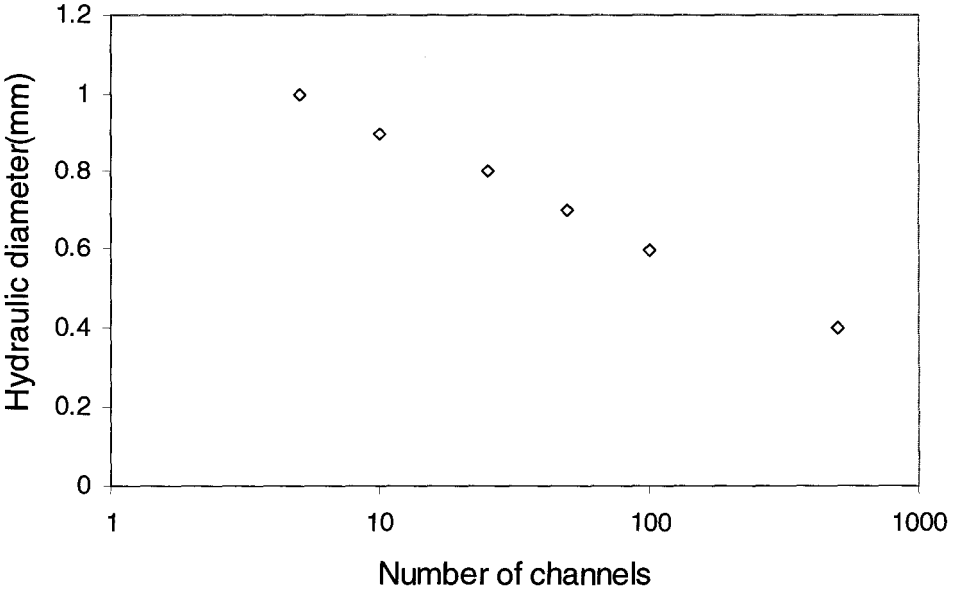

Figure 5.15: Hydraulic diameter corresponding to minimum pool coverage in the condenser using water for ω = 5000 rpm, T_{sat} = 30°C, T_{inf} = -30°C and U_{plane} = 300 km/h.

600 km/h. The heat transfer rate through the system and the vapour temperature did not change significantly as the number of heating channels was increased. An additional 35W to 50W of heat was transfer to the nose cone from the channels over the engine speed range. The channels accounted for approximately 5% of the total heat transfer through the system. The effect of the number of heating channels on the temperature of the nose cone surface is shown in figure 5.16. The use of 10 channels extended the location where the nose cone surface temperature fell below 0°C from $s/S = 0.2$ to 0.25 while both 50 and 100 heating channels extended this location to $s/S = 0.28$.

The use of more heating channels should result in a more uniform surface temperature around the circumference of the nose cone. The temperature would be uniform beyond a certain number of channels. The nose cone shell between the heating channels was analyzed as such. The thermal resistance of the conduction heat transfer across the nose cone relative to the heat transfer to the flow over the nose cone is characterized by the Biot number given by

$$Bi = \frac{h L/2}{k}, \tag{5.1}$$

where h is the heat transfer coefficient, k is the thermal conductivity of the nose cone. Here, L is the distance between adjacent heating channels given by

$$L = \frac{2\pi R}{N}. \tag{5.2}$$

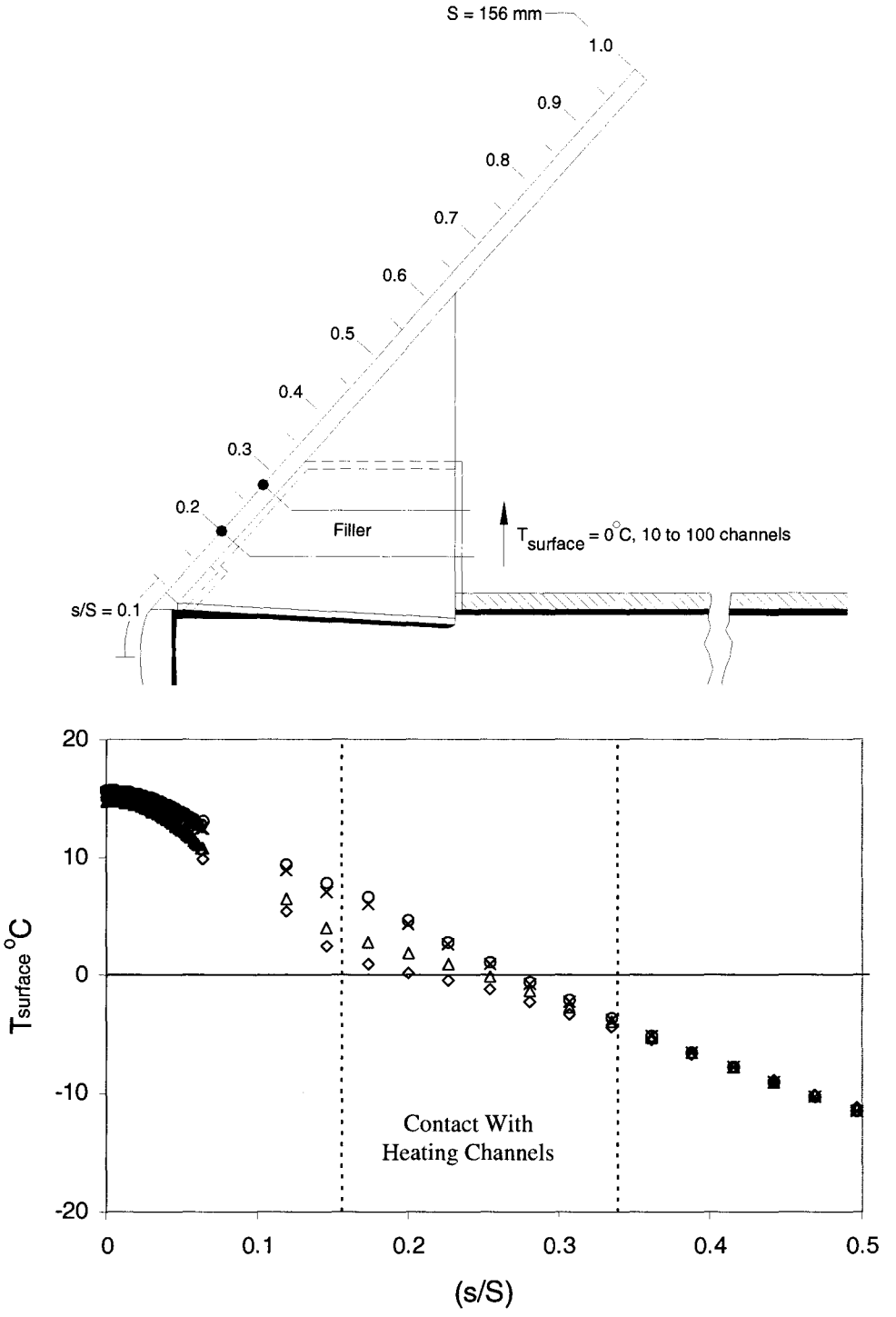

Figure 5.16: Surface temperature of the nose cone using water and ◊ 10 insulated channels, Δ 10 channels, × 50 channels, o 100 channels; ω = 5000 rpm, T_{inf} = -30°C when U_{plane} = 600 km/h.

where R is the local radius of the nose cone and N is the number of heating channels. In this case, $R \leq 40\,\text{mm}$ so for typical conditions in this application the Biot number is given by

$$Bi \sim O\left(\frac{1}{N}\right). \tag{5.3}$$

The temperature variation in the nose cone between two heating channels is less than 5% when the Biot number is on the order of 0.1, and this is true for cases where 10 or more channels are used.

The temperature variation of the fluid along the heating channels is shown in figure 5.17. The temperature did not vary significantly over the length of the channel in contact with the nose cone indicating that the heating channel flow tended to retain its thermal energy rather than transfer it to the nose cone.

The temperature of the nose cone with heating channels when ethanol was the working fluid is shown in figure 5.18. In this case, the addition of the heating channels extended the arclength of the nose cone maintained above 0°C by 10% from $s/S = 0.19$ to 0.23 when 10 channels were used and by 20%, to $s/S = 0.26$ for both 50 and 100 channels. The heat transfer in the heating channels was smaller when ethanol was used instead of water because of the smaller thermal conductivity of ethanol.

The results show that the use of heating channels should increase the arclength of the nose cone that is maintained above 0°C, however this increase was quite modest particularly when ethanol was used. The reason for this was not

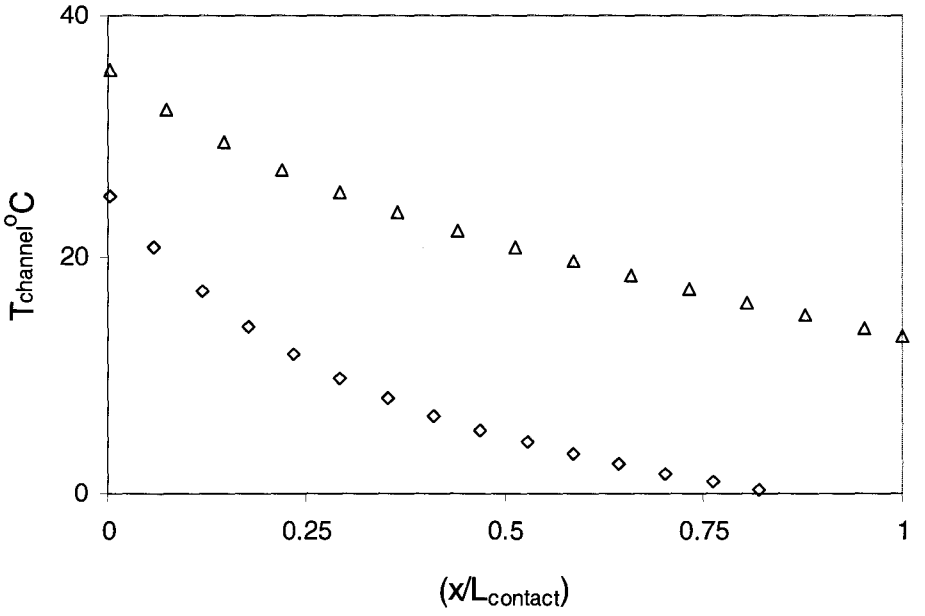

Figure 5.17: Temperature of the water flow in the heating channels for the case of 10 channels at ω = ◊ 5000 rpm, Δ 20000 rpm for T_{inf} = -30°C and U_{plane} = 600 km/h.

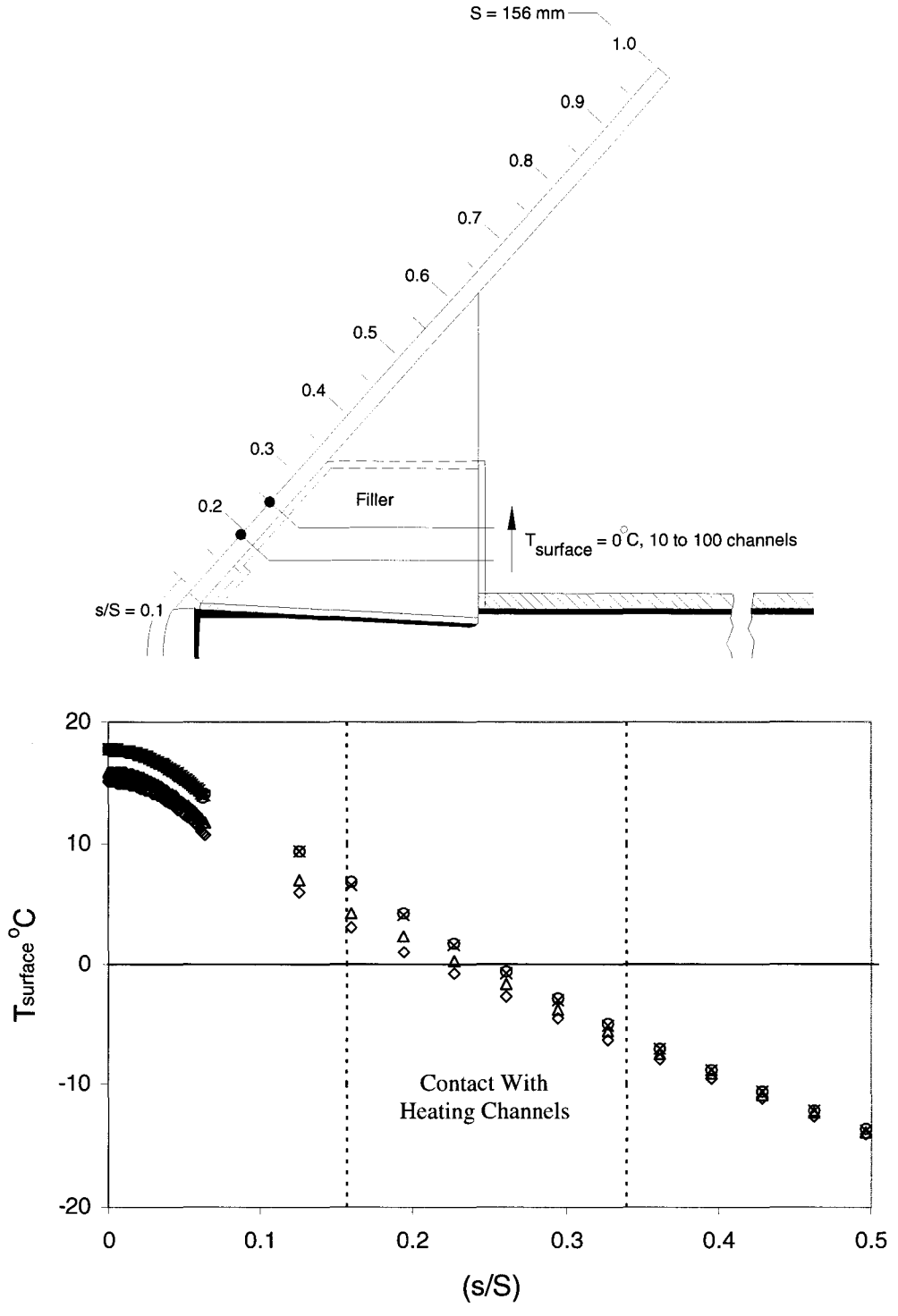

Figure 5.18: Surface temperature of the nose cone using ethanol and ◊ 10 insulated channels and Δ 10, × 50, o 100 active channels for T_{inf} = -30°C and U_{plane} = 300 km/h.

that the heat transfer coefficient of the channel flow was smaller than the heat transfer coefficient of the flow over the nose cone. In this case, the heat transfer coefficient of the heating channel flow was on the order of 20000 W/m^2K for water and 3500 W/m^2K for ethanol. The heating channels were ineffective because the contact area that they made with the nose cone was small and created a high thermal resistance between the condensate and the nose cone. One possible modification to the heating channel design could be to loop the heating channels multiple times on the nose cone surface to increase the contact area. It is not clear whether the increase in the system performance would merit the complexity and cost that would be likely incurred in manufacturing serpentine heating channels in the nose cone.

5.3 Effect of Heat Transfer Enhancement in the Evaporator

The effect of using passive heat transfer augmentation on the outside of the rotating heat pipe in the evaporator was considered for the case where cubic protrusions would be added to the surface. The same array geometry for the cubes was chosen so that the experimental results could be used in the heat transfer model. The higher axial Reynolds number case of 1950 was evaluated so that the heat transfer enhancement would be the greatest for the range considered in this investigation.

The predicted effect of adding the cubic protrusions to the outside surface of the rotating heat pipe on the system heat transfer for the case of water or ethanol as working fluids is shown in figure 5.19. The heat transfer increased modestly over the engine speed range and was slightly greater for water. The temperature profiles on the surface of

the nose cone for these cases are shown in figure 5.20. The surface temperatures increased over the region in contact with the polycrystalline graphite filler and the arclength of the nose cone maintained above 0°C was extended by a similar distance to that found when heating channels were used. The increase in this distance was smaller when ethanol was used as the working fluid instead of water.

5.4 Summary of Performance

A summary of the heat transfer performance of the anti-icing system is given in figure 5.21 using water or ethanol as the working fluid. The system was characterized using the simple thermal resistance network shown. In most cases, the thermal resistance of a particular heat transfer process or component varied over its geometry and so its equivalent thermal resistance was computed using

$$\frac{1}{R_{eq}} = \sum_i \frac{1}{R_i} = \sum_i \frac{\Delta T_i}{Q_i}. \tag{5.4}$$

Here, R_{eq} is the equivalent resistance, R_i is the thermal resistance imposed by an individual discrete control volume i, and ΔT_i and Q_i are the characteristic temperature difference and heat transfer rate through the control volume. Representative values of each resistance are provided in the figure for engine rotation speeds of 5000 rpm and 20000 rpm and airplane speeds of 300 km/h and 600 km/h.

The thermal resistance of the flow over the rotating heat pipe in the current evaporator design was relatively large compared to the resistance of the heat pipe wall and the evaporator film inside the heat pipe when water was the working fluid. In the

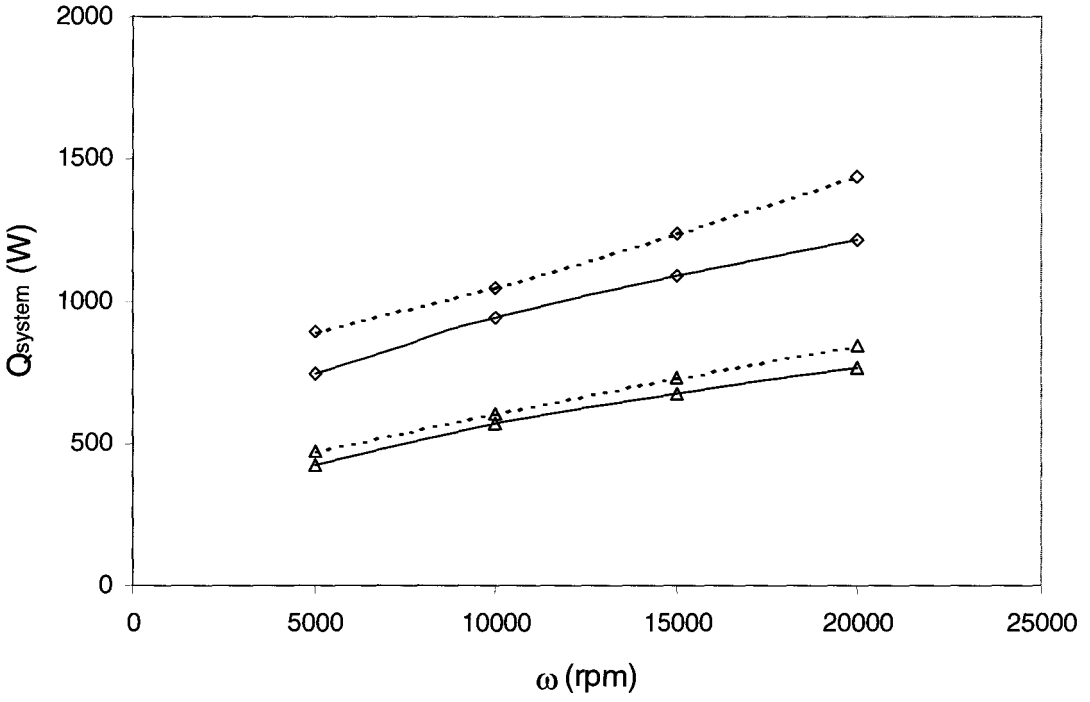

Figure 5.19: System heat transfer performance using a — smooth surface and a ---- surface with cubic protrusions in the evaporator for ◊ water and Δ ethanol for T_{inf} = -30°C and U_{plane} = 300 km/h.

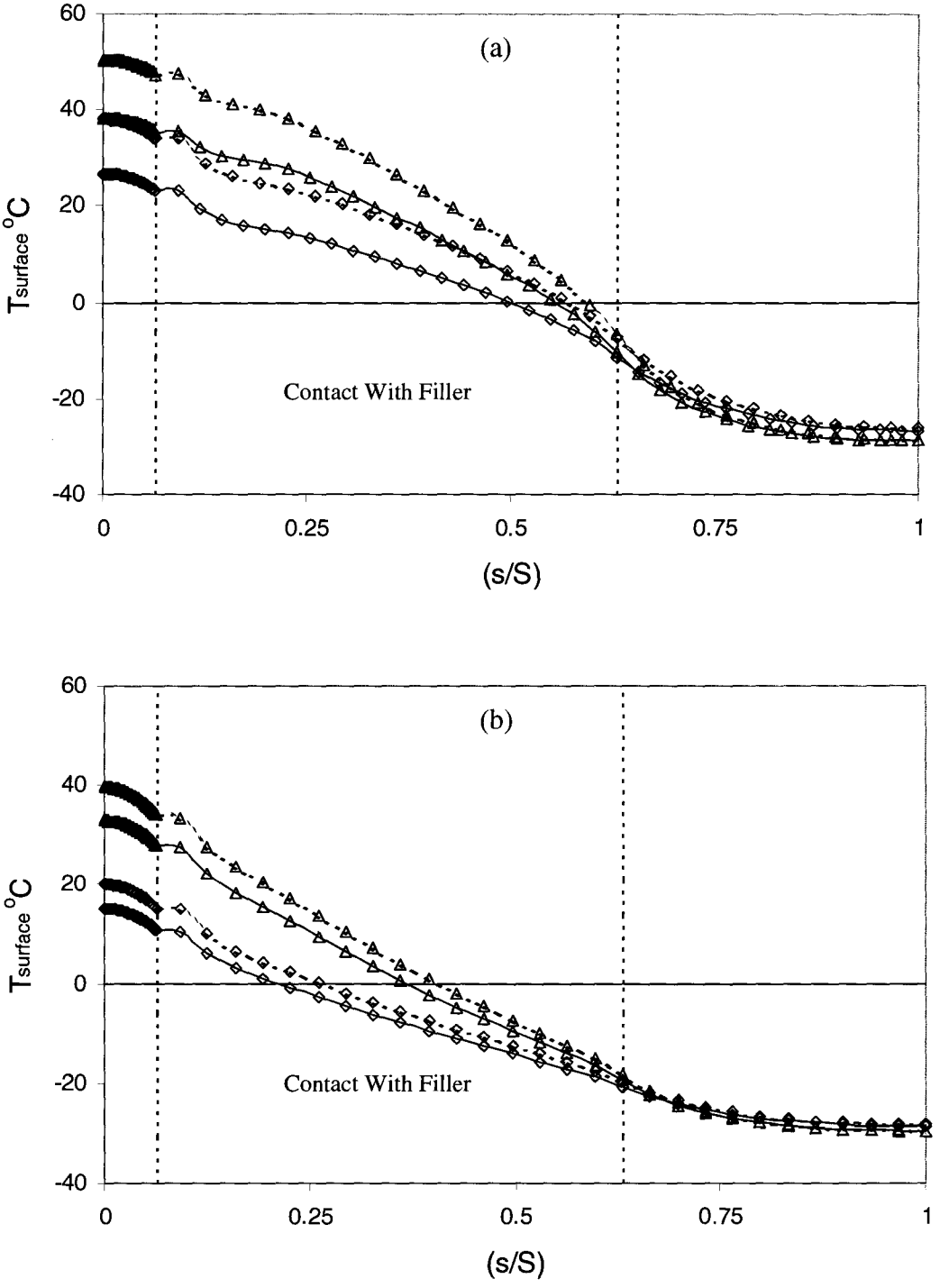

Figure 5.20: Temperature of the nose cone surface using (a) water and (b) ethanol as the working fluid with — no enhancement and ---- enhancement at ω = ◊ 5000 rpm, Δ 20000 rpm for U_{plane} = 300 km/h and T_{inf} = -30°C.

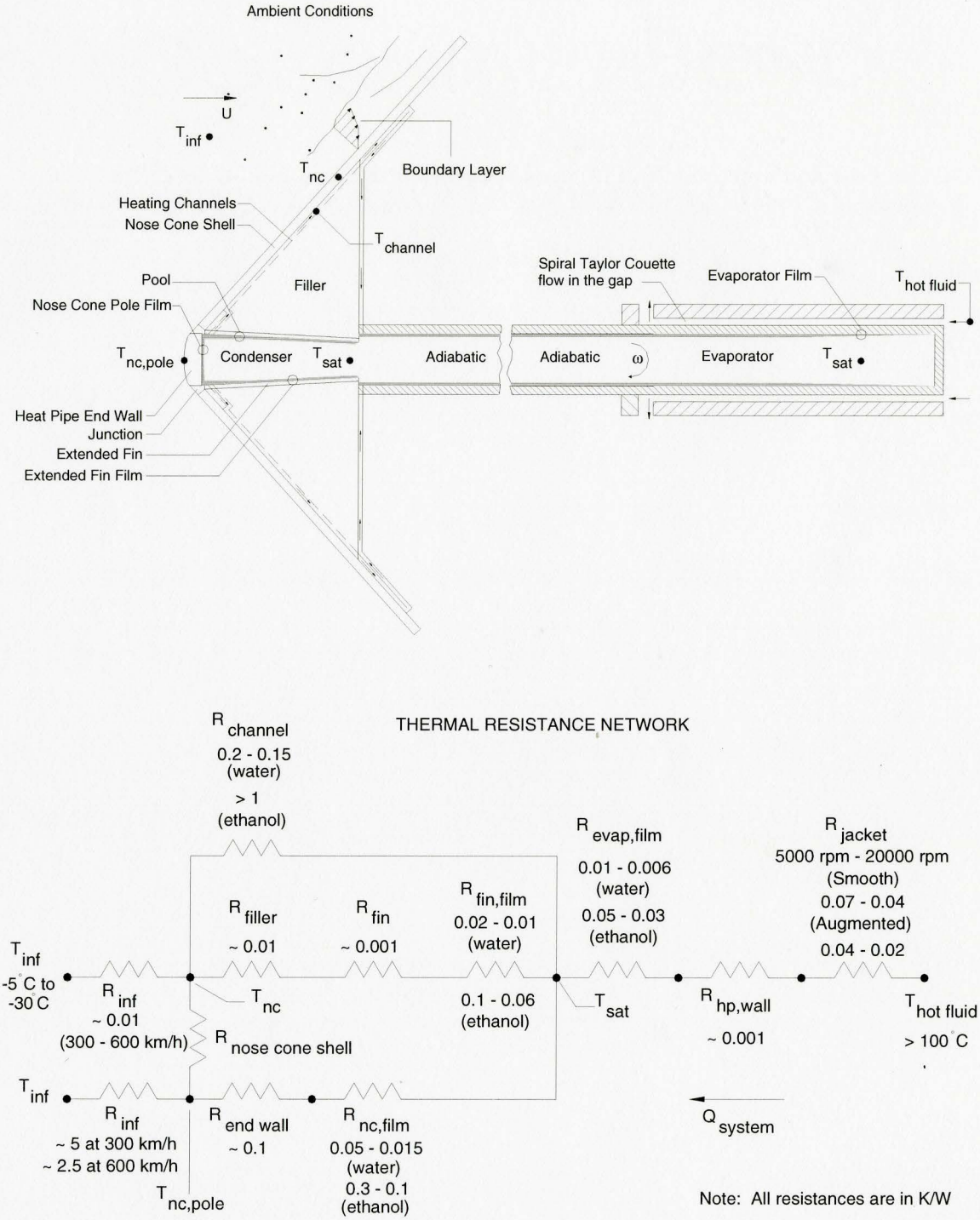

Figure 5.21: Thermal resistance representation of the anti-icing system.

case when ethanol was used as the working fluid, the film had a similar thermal resistance to the flow over the outside of the heat pipe. Since ethanol is more likely to be the working fluid in the practical application, it would be also be useful to consider the use of heat transfer enhancement on the inside of the rotating heat pipe.

The condenser end of the thermal resistance diagram consists of three basic pathways through which the heat is transferred to the flow over the nose cone. The upper path represents the heating channels where a high thermal resistance due to a small contact area inhibited the heat transfer through this path. The middle path represents the heat transfer through the condensate film on the tapered wall, the filler material and the flow over the nose cone over the nose cone shell region. This was found to be the dominant heat transfer path of the system with the lowest thermal resistances. The resistance of the condensate film and the filler material were similar on the order of 0.01 K/W when water was the working fluid. It is important to note that the thermal resistance of the condensate film increased about one order in magnitude when ethanol was used instead of water. Another heat transfer path exists along the tapered wall of the condenser however this was neglected here because this path could be insulated in the practical application. Finally, the bottom path characterizes the heat transfer through the condensate film on the end wall of the heat pipe, the end wall and the flow over the outside surface of the nose cone over this region. In this case the thermal resistance of the film was relatively small when water was the working fluid and again, an increase by a factor of 10 occurred when ethanol was used. The end wall of the heat pipe imposed a relatively high resistance however the flow over the nose cone in this region was the

dominant thermal resistance. This high resistance was why the majority of the condensation heat transfer into the end wall was conducted up the nose cone along a path of lower thermal resistance. This occurrence worked to the benefit of the system. As with the inside of the heat pipe in the evaporator, the use of heat transfer enhancement on the condensation surfaces would also be useful since ethanol is a more likely working fluid in the practical application and would impose a significant thermal resistance.

Chapter 6 Conclusions

The performance of a novel aero-engine nose cone anti-icing system that uses a rotating heat pipe was examined in this investigation. The heat pipe would transport waste heat from the engine to the nose cone and maintain its surface temperature over a critical region above freezing to prevent ice accumulation. The primary advantage of this system is that it would reduce or eliminate the use of compressor bleed air currently used to anti-ice the nose cone.

A preliminary evaporator design that would transport heat from the engine to the rotating heat pipe consisted of a stationary jacket that surrounded the heat pipe with a thin annular gap. Fluid heated by the engine was passed through the gap to provide the heat source. Passive heat transfer enhancement using surface roughness on the outside of the rotating heat pipe in the evaporator was examined experimentally. The condenser design was an integral part of the nose cone. The condensation surfaces consisted of a tapered wall emanating from the inside of the nose cone and the relatively flat central region on the inside of the nose cone used as the end wall of the heat pipe. A high conductivity polycrystalline graphite filler material encased the rotating heat pipe condenser for conduction heat transfer from the condenser to the nose cone shell. A modified condenser design was also considered where a series of heating channels were used to pump the rotating heat pipe condensate along the inside surface of the nose cone to provide additional anti-icing capacity.

The anti-icing system was modeled numerically. Individual heat transfer models were formulated for each heat transfer process or component and were coupled together by the boundary conditions and solved iteratively. The performance was estimated using water and ethanol as working fluids during continuous icing conditions for a typical geometry and range of airplane and engine speeds found in practice for a small turbo-fan engine.

The predicted heat transfer rate through the proposed anti-icing system was 600W to 1700 W using water as the working fluid and 400W to 750 W using ethanol. The ethanol had a lower thermal conductivity, specific heat and latent heat of vapourization compared to water. Consequently, ethanol imposed a higher thermal resistance during evaporation and condensation in the rotating heat pipe. Despite this, alcoholic fluids such as ethanol are attractive in this application because of the low temperature operating environment and the fact that they would not freeze and cause complications during the start-up of the anti-icing system. The heat transfer through the system increased with engine rotation speed because the film thickness in the evaporator and condenser decreased due to the increase in the driving forces in the films. The heat transfer also increased with airplane speed due to higher convection and water droplet impingement on the nose cone.

The nose cone surface temperature was maintained above 0°C for approximately 50% to 75% (70 mm to 110 mm) of the surface arclength measured from the pole of the nose cone at an airplane speed of 300 km/h during continuous icing at an ambient temperature of -30°C without heating channels using water as the working fluid.

Approximately 20% to 30% (30 mm – 45 mm) of the surface arclength was maintained above 0°C using ethanol under similar conditions. The portion of the nose cone maintained above 0°C decreased significantly when the airplane speed was increased to 600 km/h. At an ambient temperature of -30°C, this arclength decreased from 50% of the nose cone arclength to 20% using water as the working fluid. In this case, the heating channels were brought into contact with the nose cone to extend the arclength maintained above 0°C. The use of 10 channels extended this length to 25% while 50 and 100 channels extended it to 28%. The heating channels were found to be an ineffective method of delivering significant amounts of heat to the nose cone. It was not possible to make the contact area with the nose cone large enough due to the small mass flow rate of working fluid in the rotating heat pipe. The heating channel performance using ethanol was even less because of its lower thermal conductivity.

The use of passive heat transfer enhancement in the evaporator increased the system heat transfer rate modestly. The arclength of the nose cone maintained above 0°C was extended by a similar amount to that achieved using the heating channels.

The performance of the anti-icing system was summarized using a thermal resistance network to represent the key resistances throughout the system. The evaporator was found to impose one of the higher thermal resistances in the system that could significantly inhibit the heat transfer into the rotating heat pipe. The use of passive heat transfer enhancement decreased this thermal resistance, however, it was still relatively large compared to the other resistances. The evaporator and condenser films had a low thermal resistance when water was used as the working fluid. However, an

increase nearly an order in magnitude occurred using ethanol. This was a result of much thicker films due to the lower thermal conductivity of ethanol. In the condenser, the dominant heat transfer was through the tapered wall and the polycrystalline graphite filler. The remaining heat was transferred into the tip of the nose cone at the end wall of the heat pipe. Although this heat transfer was small, the tip was effectively maintained well above freezing under all icing conditions. The heating channels had an order of magnitude higher thermal resistance than the other components and heat transfer processes in the system.

In conclusion, the rotating heat pipe was demonstrated to be a promising thermal management device in aero-engine nose cone anti-icing. The evaporator design for heat exchange with the engine is a critical component and requires further optimization. The use of high conductivity composite materials was shown to be an excellent strategy for heat transfer from the heat pipe to the nose cone.

Chapter 7 Recommendations

Several recommendations are made here on further development of the proposed anti-icing system. The evaporator design must be improved as it imposed a relatively high thermal resistance the system. The passive heat transfer augmentation results showed that the thermal resistance could be reduced moderately, however, a reduction by an order of magnitude over the entire operating range would be desirable.

The significant reduction in the system performance using ethanol as the working fluid instead of water raised concern about the choice of working fluid for the rotating heat pipe. Since pure water could not be used in the practical application it is prudent to find a better alternative working fluid than ethanol. One concern with the choice of working fluid is its chemical interaction with the material used to fabricate the rotating heat pipe and the possible generation of non-condensable gases in the heat pipe over time. The presence of a non-condensable gas was found to significantly inhibit the performance of the rotating heat pipe (Daniels and Williams, 1978). One should be cognizant of this effect in the selection process of the working fluid.

In the condenser, the heating channels were found to be very ineffective. It is recommended that a standard rotating heat pipe condenser encased in polycrystalline graphite or another composite type of material be used to heat the nose cone. In general, the thermal resistances of the films were larger than the solids. The use of passive heat transfer enhancement has been considered on the inside surface of rotating heat pipes. For example Marto and Wagenseil (1979) experimentally investigated using fins in the

condenser and found that the condenser heat transfer increased by up to 100% for cylindrical heat pipes. The use of enhanced surfaces inside the heat pipe may prove to be beneficial for certain working fluids like ethanol and further investigation for future designs is recommended.

The heat transfer due to the non-homogeneous flow of air and water droplets over the outside of the nose cone and the effect of the impacting droplets is the poorest modeled heat transfer process in the current anti-icing system. The lack of information available in the open literature on ice accretion to aero-engine nose cones was noted before. It would be prudent to characterize the droplet trajectories and the collection efficiency over the nose cone surface either experimentally or using more advanced computational techniques outlined in the literature review. Moreover, the evaporation of the impacting water droplets would result in a mass transfer boundary layer over the outside surface that was not considered here. It is recognized that characterizing the flow and heat transfer over the nose cone in icing environments would be an expensive and complex endeavour. If a computational approach were taken, it would involve at the very least, a solution of the potential flow field, a Lagrangian particle tracking computation for the droplets and a far more advanced thermodynamic analysis of the water interaction with the surface of the nose cone. This type of analysis is becoming commonplace in aircraft icing calculations and is required for more accurate heat load calculation. Using an experimental approach and studying ice accretion to rotating nose cones in an icing tunnel would also be very useful and would provide a base of knowledge to compare modeling results with.

Bibliography

Afzal, N., and Hussain, T., 1984, "Mixed Convection Over a Horizontal Plate," *Journal of Heat Transfer,* vol. 106, pp. 240-241.

Al-Khalil, K.M., Keith, T.G. Jr., and DeWitt, K.J., 1990, "Thermal Analysis of Engine Inlet Anti-Icing Systems," *Journal of Propulsion,* vol. 6, No. 5, pp. 628-634.

Al-Khalil, K.M., Keith, T.G. Jr., and DeWitt, K.J., 1997, "Icing Calculations on a Typical Commercial Jet Engine Inlet Nacelle," *Journal of Aircraft,* vol. 34, No. 1, pp. 87-93.

Andereck, D.C., Liu, S.S., and Swinney, H.L., 1986, "Flow Regimes in a Circular Couette System with Independently Rotating Cylinders," *Journal of Fluid Mechanics,* vol. 164, pp. 155-183.

Arpaci, V.S., and Kao, S.-H., 1997, "Microscales of Rotating Turbulent Flows," *International Journal of Heat and Mass Transfer,* vol. 40, No. 16, pp. 3819-3826.

Astill, K.N., 1964, "Studies of the Developing Flow Between Concentric Cylinders with the Inner Cylinder Rotating," *Journal of Heat Transfer*, vol. 86, pp. 383-392.

Axcell, B.P., and Thianpong, C., 2001, "Convection to Rotating Disks with Rough Surfaces in the Presence of an Axial Flow," *Experimental Thermal and Fluid Science,* vol. 25, pp. 3-11.

Ballback, L.J., 1969, "The Operation of a Rotating Wickless Heat Pipe," M.Sc. Thesis Monterey California Naval Post-graduate School (AD 701674).

Becker, K.M., and Kaye, J., 1962, "Measurements of Diabatic Flow in an Annulus with an Inner Rotating Cylinder," *Journal of Heat Transfer,* vol. 84, pp. 97-105.

Beckett, P.M., Hudson, P.C., and Poots, G., 1973, "Laminar Film Condensation Due to a Rotating Disk," *Journal of Engineering Mathematics,* vol. 7, No. 1, pp. 63-73.

Bjorklund, I.S., and Kays, W.M., 1959, "Heat Transfer Between Concentric Rotating Cylinders," *Journal of Heat Transfer,* vol. 81, pp. 175-186.

Bourgault, Y., Boutanios, Z., and Habashi, W.G., 2000, "Three-Dimensional Eulerian Approach to Droplet Impingement Simulation Using FENSAP-ICE, Part 1: Model, Algorithm, and Validation," *Journal of Aircraft,* vol. 37, No. 1, pp. 95-103.

Brown, J.M., Raghunathan, S., Watterson, J.K., Linton, and A.J., Riordon, D., 2002, "Heat Transfer Correlation for Anti-icing Systems," *Journal of Aircraft,* vol. 39, No. 1, pp. 65-70.

Butuzov, A.I., and Rifert, V.F., 1972, "An Experimental Study of Heat Transfer During Condensation of Steam at a Rotating Disk," *Heat Transfer – Soviet Research,* vol. 4, No. 6, pp. 150-153.

Carpenter, E.F. and Colburn, A.P., "The Effect of Vapour Velocity on Condensation Inside Tubes," Proceedings of General Discussion on Heat Transfer, London (Institute of Mechanical Engineers, London), 11-13 September, 1951.

Cebeci, T., and Fassi, K., 2003, "Aircraft Icing," *Annual Review of Fluid Mechanics,* vol. 35, pp. 11-21.

Chandrasekhar, S., 1962, "The Stability of Spiral Flow Between Rotating Cylinders," *Proceedings of the Royal Society A,* vol. 265, pp. 188-197.

Chang, M.H., and Chen, C.K., 2002, "The Stability of the Narrow-Gap Taylor-Couette System with an Axial Flow," *ACTA Mechanica,* vol. 156, pp. 131-143.

Chung, D.D.L. *Carbon Fiber Composites.* Newton, MA.: Butterworth-Heinemann, 1994.

Churchill, S.W., "Combined Free and Forced Convection Around Immersed Bodies," in Hewitt, G.F. (Ed.) *Heat Exchanger Design Handbook*, Washington D.C.: Hemisphere, 1990.

Chyu, M.K., Hsing, Y., Natarajan, V., and Chiou, J.S., 1996, "Effects of Perpendicular Flow Entry on Convective Heat(Mass) Transfer From Pin-Fin Arrays," *Transactions of the ASME HTD*, National Heat Transfer Conference, vol. 329, volume 7, pp. 45-52.

Chyu, M.K., Hsing, Y.C., Shih, T.I.-P., and Natarajan, V., "Heat Transfer Contributions of Pins and End-wall in Pin-Fin Arrays: Effects of Thermal Boundary Conditions Modeling," *ASME paper 98-GT-175.*

Chyu, M.K., and Natarajan, V., 1991, "Local Heat/Mass transfer Distributions on the Surface of a Wall-Mounted Cube," *Journal of Heat Transfer,* vol. 113, pp. 851-857.

Chyu, M.K., and Natarajan, V., 1996, "Heat Transfer on the Base Surface of Three-Dimensional Protruding Elements," *International Journal of Heat and Mass Transfer,* vol. 39, No. 14, pp. 2925-2935.

Cober, S. G., Isaac, G. A., and Strapp, W.J., 2001, "Characterizations of Aircraft Icing Environments that Include Supercooled Large Drops," *Journal of Applied Meteorology,* vol. 40, pp. 1984-2002.

Coles, D., 1965, "Transition in Circular Couette Flow," *Journal of Fluid Mechanics,* vol. 21, pp. 385-425.

Cornish, R.J., 1933, "Flow of Water Through Fine Clearances with Relative Motion of the Boundaries," *Proceedings of the Royal Society, A,* vol. 140, pp. 227-240.

Crespo, J.S., and Marques, F., 1993, "Spiral Vortices Between Concentric Cylinders," *Applied Scientific Research,* vol. 51, pp. 55-59.

Daniels, T.C., and Al-Baharnah, N.S., 1980, "Temperature and Heat Load Distribution in Rotating Heat Pipes," *AIAA Journal,* vol. 18, No. 2, pp. 202-207.

Daniels, T.C., and Al-Jumaily, F.K., 1975, "Investigation of the Factors Affecting the Performance of a Rotating Heat Pipe," *International Journal of Heat and Mass Transfer,* vol. 18, pp. 961-973.

Daniels, T.C., and Williams, R.J., 1978, "Experimental Temperature Distribution and Heat Load Characteristics of Rotating Heat Pipes," *International Journal of Heat and Mass Transfer,* vol. 21, pp. 193-201.

DiPrima, R.C., 1960, "The Stability of a Viscous Fluid Between Rotating Cylinders with an Axial Flow," *Journal of Fluid Mechanics,* vol. 9, pp. 621-631.

Dong, Y.H., Lu, X.Y., and Zhuang, L.X., 2002, "An Investigation of the Prandtl Number Effect on Turbulent Heat Transfer in Channel Flows by Large Eddy Simulation," *ACTA Mechanica,* vol. 159, pp. 39-51.

Edwards, D.K., Denny, V.E., and Mills, A.F. *Transfer Processes.* 2nd ed. Washington, D.C.: Hemisphere, 1979.

Edwards, F.J., and Sheriff, N., 1961, "The Heat Transfer and Friction Characteristics for Forced Convection Air Flow over a Particular Type of Rough Surface," *International Developments in Heat Transfer,* P.3, Series A, ASME, New York, 415-425.

El-Shaarawi, M.A.I., and Al-Jamal, K., 1992, "Forced Convection About a Rotating Sphere," *Applied Energy,* vol. 43, pp. 221-238.

Eschweiler, J.C., Benton, A.M., and Prechshot, G.W., 1967, "Boiling and Convective Heat Transfer at High Accelerations," *Chemical Engineering Progress Symposium Series,* vol. 63, pp. 66-72.

Espig, H., and Hoyle, R., 1965, "Waves in a Thin Liquid Layer on a Rotating Disk," *Journal of Fluid Mechanics,* vol. 22, pp. 671-677.

Espig, H., and Hoyle, R., 1968, "The Transfer of Heat from Condensing Steam to a Cold Rotating Disk," Proceeding of the Institute of Mechanical Engineers, vol. 182, part 3H, pp. 406-412.

Faghri, A., Gogineni, S., and Thomas, S., 1993, "Numerical Analysis of Vapour Flow in an Axially Rotating Heat Pipe," *International Journal of Heat and Mass Transfer,* vol. 36, No. 9, pp. 2293-2303.

Fox, R.W., McDonald, A.T. *Introduction to Fluid Mechanics.* New York, NY: John Wiley & Sons, Inc., 1992.

Gao, N., 2000, *Heat Transfer Enhancement in Impinging Round Jets.* Masters Thesis, McMaster University, Hamilton, Ontario, Canada.

Garimella, S.V., and Eibeck, P.A., 1990, "Heat Transfer Characteristics of an Array of Protruding Elements in Single Phase Forced Convection," *International Journal of Heat Transfer,* vol. 33, No. 12, pp. 2659-2669.

Garrett, S.J., and Peake, N., 2002, "The Stability and Transition of the Boundary Layer on a Rotating Sphere," *Journal of Fluid Mechanics,* vol. 456, pp. 199-218.

Gazley, C., 1958, "Heat Transfer Characteristics of the Rotational and Axial Flow Between Concentric Cylinders," *Transactions of the ASME,* vol. 80, pp. 79-90.

Gray, V.H., 1969, "The Rotating Heat Pipe," *ASME paper no. 69-HT-19.*

Han, J.C., Glicksman, L.R., and Rohsenow, W.M., 1978, "An Investigation of Heat Transfer and Friction for Rib-Roughened Surfaces," *International Journal of Heat and Mass Transfer,* vol. 21, pp. 1143-1156.

Han, J.-C., and Zhang, Y.M., 1992, "Effect of Uneven Wall Temperature on Local Heat Transfer in a Rotating Square Channel with Smooth Walls and Radial Outward Flow," *Journal of Heat Transfer,* vol. 114, pp. 850-858.

Han, J.-C., Zhang, Y.M., and Kalkuehler, K., 1993, "Uneven Wall Temperature Effect on Local Heat Transfer in a Rotating Two-Pass Square Channel with Smooth Walls," *Journal of Heat Transfer,* vol. 115, pp. 912-920.

Harley, C., and Faghri, A., 1995, "Two-Dimensional Rotating Heat Pipe Analysis," *Journal of Heat Transfer,* vol. 117, pp. 202-208.

Hartnett, J.P., Deland, E.C., 1961, "The Influence of Prandtl Number on the Heat Transfer From Rotating Non-isothermal Disks and Cones," *Journal of Heat Transfer,* vol. 83, pp. 95-96.

Hossain, M.A., and Takhar, H.S., 1997, "Radiation-Conduction Interaction in Mixed Convection Along Rotating Bodies," *Heat and Mass Transfer,* vol. 33, pp. 201-208.

Hughes, T.H., and Reid, W.H., 1968, "The Stability of Spiral Flow Between Rotating Cylinders," *Philosophical Transactions of the Royal Society A,* vol. 263, pp. 57-91.

Hunt, J.C.R., Abell, C.J., Peterka, J.A., and Woo, H., 1978, "Kinematical Studies of the Flows Around Free or Surface-Mounted Obstacles; Applying Topology to Flow Visualization," *Journal of Fluid Mechanics,* vol. 86, pp. 179-200.

Hwang, G.J., and Jen, T.C., 1990, "Convective Heat Transfer in Rotating Isothermal Ducts," *International Journal of Heat and Mass Transfer,* vol. 33, No. 9, pp. 1817-1828.

Hwang, G.J., and Kuo, C.R., 1997, "Experimental Studies and Correlations of Convective Heat Transfer in a Radially Rotating Serpentine Passage," *Journal of Heat Transfer*, vol. 119, pp. 460-466.

Incopera, F.P., and DeWitt, D.P. *Introduction to Heat Transfer.* 3rd ed. John Wiley & Sons, Inc., 1996.

Jacobi, A.M., and Shah, R.K., 1995, "Heat Transfer Surface Enhancement through the use of Longitudinal Vortices: A Review of Recent Progress," *Experimental Thermal and Fluid Science,* vol. 11, pp. 295-309.

Jakoby, R., Kim, S., and Wittig, S., 1998, "Correlations of the Convective Heat Transfer in Annular Channels with Rotating Inner Cylinder," *ASME paper no. 98-GT-97.*

Jubran, B.A., Hamdan, M.A., and Abdualh, R.M., 1993, "Enhanced Heat Transfer, Missing Pin, and Optimization for Cylindrical Pin Fin Arrays," *Journal of Heat Transfer,* vol. 115, pp. 576-583.

Kalinin, E.K., and Dreitser, G.A., 1998, "Heat Transfer Enhancement in Heat Exchangers," *Advances in Heat Transfer,* vol. 31, pp. 159-332.

Kaye, J., and Elgar, E.C., 1958, "Modes of Adiabatic and Diabatic Fluid Flow in an Annulus with an Inner Rotating Cylinder," *Transactions of the ASME,* vol. 80, pp. 753-765.

Kind, R.J., Potapczuk, M.G., Feo, A., Golia, C., and Shah, A.D., 1998, "Experimental and Computational Simulation of In-Flight Icing Phenomena," *Progress in Aerospace Science*, vol. 34, pp. 257-345.

Kline, S.J., and McClintock, F.A., 1953, "Describing Uncertainties in Single-Sample Experiments," *Mechanical Engineering*, vol. 75, pp. 3-8.

Kobayashi, R., 1994, "Review: Laminar-to-Turbulent Transition of Three-Dimensional Boundary Layers on Rotating Bodies," *Journal of Fluids Engineering,* vol. 116, pp. 200-211.

Kobayashi, R., Arai, T., and Nakajima, M., 1988, "Boundary Layer Transition and Separation on Spheres Rotating in Axial Flow," *Experimental Thermal and Fluid Science,* vol. 1, pp. 99-104.

Kobayashi, R., and Izumi, H., 1983, "Boundary Layer Transition on a Rotating Cone in Still Fluid," *Journal of Fluid Mechanics,* vol. 26, No. 4, pp. 354-359.

Kobayashi, R., Kohama, Y., and Kurosawa, M., 1983, "Boundary Layer Transition on a Rotating Cone in Axial Flow," *Journal of Fluid Mechanics,* vol. 127, pp. 341-352.

Koh, J.C.Y., and Price, J.F., 1967, "Non-similar Boundary Layer Heat Transfer of a Rotating Cone in Forced Flow," *Journal of Heat Transfer,* vol. 89, pp. 139-145.

Kohama, Y., 1984, "Behaviour of Spiral Vortices on a Rotating Cone in Axial Flow," *ACTA Mechanica,* vol. 51, pp. 105-117.

Kohama, Y., 1985, "Flow Structures Formed by Axisymmetric Spinning Bodies," *AIAA Journal,* vol. 23, No. 9, pp. 1445-1447.

Kohama, Y., and Kobayashi, R., 1983a, "Behaviour of Spiral Vortices on Rotating Axisymmetric Bodies," *Report of Institute of High Speed Mechanics, Tohoku University, Japan,* vol. 47, pp. 27-38.

Kohama, Y., and Kobayashi, R., 1983b, "Boundary Layer Transition and the Behaviour of Spiral vortices on Rotating Spheres," *Journal of Fluid Mechanics,* vol. 137, pp. 153-164.

Kreith, F., 1968, "Convection Heat Transfer in Rotating Systems," *Advances in Heat Transfer,* vol. 5, pp. 129-251.

Kreith, F., Roberts, L.G., Sullivan, J.A., and Sinha, S.N., 1963, "Convection Heat Transfer and Flow Phenomena on Rotating Spheres," *International Journal of Heat and Mass Transfer,* vol. 6, pp. 881-895.

Krueger, E.R., and DiPrima, R.C., 1964, "The Stability of a Viscous Fluid Between Rotating Cylinders with an Axial Flow," *Journal of Fluid Mechanics,* vol. 19, pp. 528-538.

Kuo, C.R., and Hwang, G.J., 1996, "Experimental Studies and Correlations of Radially Outward and Inward Air-Flow Heat Transfer in a Rotating Square Duct," *Journal of Heat Transfer,* vol. 118, pp. 23-30.

Kuzay, T.M., and Scott, C.J., 1977, "Turbulent Heat Transfer Studies in Annulus with Inner Cylinder Rotation," *Journal of Heat Transfer,* vol. 99, pp. 12-19.

Lee, Y.N., and Minkowycz, W.J., 1989, "Heat Transfer Characteristics of the Annulus of Two Coaxial Cylinders with One Cylinder Rotating," *International Journal of Heat and Mass Transfer,* vol. 32, No. 4, pp. 711-722.

Li, H.M., Liu, C.Y., and Damodaran, M., 1993, "Analytical Study of the Flow and Heat Transfer in a Rotating Heat Pipe," *Heat Recovery Systems and CHP,* vol. 13, No. 2, pp. 115-122.

Ligrani, P.M., Oliveira, M.M., and Blaskovich, T., 2003, "Comparison of Heat Transfer Augmentation Techniques," *AIAA Journal,* vol. 41, No. 3, pp. 337-362.

Lin, C.K., Kline, S.J., and Johnston, J.P., 1966, "An Experimental Study of Turbulent Boundary Layer on Rough Walls," Report MD-15, Department of Mechanical Engineering, Stanford University.

Magai, V.K. *Enhancement of the Efficiency of Modern Heat Exchangers.* Leningrad: Energiya, 1980.

Maron, D.M., and Cohen, S., 1991, "Hydrodynamics and Heat/Mass Transfer near Rotating Surfaces," *Advances in Heat Transfer,* vol. 21, pp. 141-183.

Marto, P.J., 1984, "Rotating Heat Pipes," in: Metzger, D.E., and Afgan, N.H. (Eds.), *Heat and Mass Transfer in Rotating Machinery*, Hemisphere, Washington, D.C.

Marto, P.J., and Wagenseil, L.L., 1979, "Augmenting the Condenser Heat-Transfer Performance of Rotating Heat Pipes," *AIAA Journal*, vol. 17, No. 6, pp. 647-652.

Maudgal, V.K., and Sunderland, J.E., 1996, "Forced Convection Heat Transfer from Staggered Pin Fin Arrays," *Transactions of the ASME HTD*, National Heat Transfer Conference, vol. 329, volume 7, pp. 35-44.

Merte, H. Jr., and Clark, J.A., 1961, "Pool Boiling in an Accelerating System," *Journal of Heat Transfer,* vol. 83, pp. 233-241.

Meseguer, A., and Marques, F., 2000, "Axial Effects in the Taylor-Couette Problem: Spiral-Couette and Spiral-Poiseuille Flows," *Physics of Rotating Fluids,* vol. 549, pg. 118.

Metzger, D.E., Berry, R.A., and Bronson, J.P., 1982, "Developing Heat Transfer in Rectangular Ducts with Staggered Arrays of Short Pin Fins," *Journal of Heat Transfer,* vol. 104, pp. 700-706.

Metzger, D.E., Fan, C.S., and Haley, S.W., 1984, "Effects of Pin Shape and Array Orientation on Heat Transfer and Pressure Loss in Pin Fin Arrays," *Journal of Engineering for Gas Turbines and Power,* vol. 106, pp. 252-257.

Mitrovic, B.M., Le, P.M., and Papavassiliou, D.V., 2004, "On the Prandtl or Schmidt Number Dependence of the Turbulent Heat or Mass Transfer Coefficient," *Chemical Engineering Science,* vol. 59, pp. 543-555.

Mori, Y., Fukada, T., and Nakayama, W., 1971, "Convective Heat Transfer in a Rotating Radial Circular Pipe (2^{nd} report)," *International Journal of Heat and Mass Transfer,* vol. 14, pp. 1807-1824.

Mori, Y., and Nakayama, W., 1968, "Convective Heat Transfer in Rotating Radial Circular Pipes (1^{st} report)," *International Journal of Heat and Mass Transfer,* vol. 11, pp. 1027-1040.

Morris, W.D., and Ghavami-Nasr, G., 1991, "Heat Transfer Measurements in Rectangular Channels with Orthogonal Mode Rotation," *Journal of Turbomachinery,* vol. 113, pp. 339-345.

Mueller, T.J., 1961, "On Separation, Re-attachment and Re-development of Turbulent Boundary Layers," Ph.D. Thesis, University of Illinois.

Nandapurkar, S.S., and Beatty, K.O. Jr., 1960, "Condensation on a Horizontal Rotating Disc," *A.I.Ch.E. Chemical Engineering Progress*, No. 30, pp. 129-137.

Okamoto, S., Seo, S., Nakso, K., and Kawai, I., 1993, "Turbulent Shear Flow and Heat Transfer over the Repeated Two-Dimensional Square Ribs on Ground Plane," *Journal of Fluids Engineering,* vol. 115, pp. 631-637.

Ozturk, A., and Ece, M.C., 1995, "Unsteady Forced Convection Heat Transfer From a Translating and Spinning Body," *Journal of Energy Resourced Technology,* vol. 117, pp. 318-323.

Panton, R.L. *Incompressible Flow.* 2nd ed. New York, NY: John Wiley & Sons Inc., 1996.

Patankar, S.V. *Numerical Heat Transfer and Fluid Flow.* Hemisphere, 1980.

Pedraza, D.F., and Klemens, P.G., 1993, "Effective Conductivity of Polycrystalline Graphite," *Carbon,* vol. 31, No. 6, pp. 951-956.

Pfitzer, H., and Beer, H., 1992, "Heat Transfer in an Annulus Between Independently Rotating Tubes with Turbulent Axial Flow," *International Journal of Heat and Mass Transfer,* vol. 35, No. 3, pp. 623-633.

Politovich, M.K., 2003, "Predicting In-Flight Aircraft Icing Intensity," *Journal of Aircraft,* vol. 40, No. 4, pp. 639-644.

Polkowski, J.W., 1984, "Turbulent Flow Between Coaxial Cylinders with the Inner Cylinder Rotating," *Journal of Engineering for Gas Turbines and Power,* vol. 106, pp. 128-135.

Ponnappan, R., He, Q., and Leland, J.E., 1998, "Test Results of Water and Methanol High-Speed Rotating Heat Pipes," *Journal of Thermophysics and Heat Transfer,* vol. 12, No. 3, pp. 391-397.

Ponnappan, R., and Leland, J.E., 1994, "Rotating Heat Pipe for Cooling of Rotors in Advanced Generators," AIAA 94-2033 in: 6th AIAA/ASME Joint Thermo-physics and Heat Transfer Conference.

Ponnappan, R., and Leland, J.E., 1995, "High Speed Rotating Heat Pipe for Aircraft Applications," SAE 951437, in: Aerospace Atlantic Conference.

Ponnappan, R., and Leland, J.E., 1998, "Rotating Heat Pipe for High Speed Motor/Generator Cooling," SAE paper no. 981287.

Reed, H.L., and Saric, W.S., 1989, "Stability of Three-Dimensional Boundary Layers," *Annual Review of Fluid Mechanics,* vol. 21, pp. 235-284.

Salzberg, F. and Kezios, S.P., 1965, "Mass Transfer form a Rotating Cone in Axisymmetric Flow," *Journal of Heat Transfer,* vol. 87, pp. 469-476.

Schlichting, H. *Boundary Layer Theory.* New York, NY: McGraw-Hill Book Co. Inc., 1955.

Schwarz, K.W., Springett, B.E., and Donnelly, R.J., 1964, "Modes of Instability in Spiral Flow Between Rotating Cylinders," *Journal of Fluid Mechanics,* vol. 20, pp. 281-289.

Sickmann, J., 1962, "The Calculation of the Thermal Laminar Boundary Layer on Rotating Sphere," *Z. Angew. Math. Phys.,* vol. 13, pg. 468.

Snyder, H.A., 1962, "Experiments on the Stability of Spiral Flow at Low Axial Reynolds Numbers," *Proceedings of the Royal Society A,* vol. 265, pp. 198-214.

Song, F., Ewing, D., and Ching, C.Y., 2003b, "Fluid Flow and Heat Transfer Model for High-Speed Rotating Heat Pipes," *International Journal of Heat and Mass Transfer,* vol. 46, pp. 4393-4401.

Song, F., Ewing, D., and Ching, C.Y., 2004, "Experimental Investigation on the Heat Transfer Characteristics of Axial Rotating Heat Pipes," *International Journal of Heat and Mass Transfer*, vol. 47, pp. 4721-4731.

Song, F., Home, D., Robinson, T., Ewing, D., and Ching, C.Y., 2003a, "Experimental Investigation of High-Speed Rotating Heat Pipes," IMECE2003-43432 in: 2003 ASME International Mechanical Engineering Congress & Exposition.

Soong, C.Y., and Chyuan, C.H., 1998, "Similarity Solutions of Mixed Convection Heat and Mass Transfer in Combined Stagnation and Rotation-Induced Flows over a Rotating Disk," *Heat and Mass Transfer,* vol. 34, pp. 171-180.

Sparrow, E.M., and Gregg, J.L., 1959a, "Heat Transfer From a Rotating Disk to Fluids of Any Prandtl Number," *Journal of Heat Transfer,* vol. 81, pp. 249-250.

Sparrow, E.M., and Gregg, J.L., 1959b, "A Theory of Rotating Condensation," *Journal of Heat Transfer,* vol. 81, pp. 113-120.

Sparrow, E.M., and Gregg, J.L., 1960, "The Effect of Vapour Drag on Rotating Condensation," *Journal of Heat Transfer,* vol. 82, pp. 71-72.

Sparrow, E.M., and Ramsey, J.W., 1978, "Heat Transfer and Pressure Drop for a Staggered Wall-Attached Array of Cylinders with Tip Clearance," *International Journal of Heat and Mass Transfer,* vol. 21, pp. 1369-1377.

Streby, M.A., Ponnappan, R., Leland, J.E., and Beam, J.E., 1996, "Design and Testing of a High Speed Rotating Heat Pipe," IEEE paper no. 96301.

Sutherland, W.A., 1967, "Improved Heat-Transfer Performance with Boundary-Layer Turbulence Promoters," *International Journal of Heat and Mass Transfer,* vol. 10, pp. 1589-1599.

Tabrizi, A.H., and Johnson, W.S., 1989, "Surface-Blowing Anti-Icing Technique for Aircraft," *Journal of Aircraft,* vol. 26, No. 4, pp. 354-359.

Tahat, M.A., Babus'Haq, R.F., and Probert, S.D., 1994, "Forced Steady-State Convections from Pin-Fin Arrays," *Applied Energy,* vol. 48, pp. 335-351.

Taylor, G.I., 1923, "Stability of a Viscous Liquid Contained Between Two Rotating Cylinders," *Philosophical Transactions A,* vol. 223, pp. 289-343.

Tien, C.L., 1960, "Heat Transfer by Laminar Flow From a Rotating Cone," *Journal of Heat Transfer,* vol. 82, pp. 252-253.

Tien, C.L. and Campbell, D.T., 1963, "Heat and Mass Transfer from Rotating Cones," *Journal of Fluid Mechanics,* vol. 17, pp. 105-112.

Tieng, S.M., and Yan, A.C., 1993, "Experimental Investigation on Convective Heat Transfer of Heated Spinning Sphere," *International Journal of Heat and Mass Transfer,* vol. 36, No. 3, pp. 599-610.

Ting, J-M., Lake, M.L., and Duffy, D.R., 1995, "Composites Based on Thermally Hyper-Conductive Vapour Grown Carbon Fiber," *Journal of Materials Research,* vol. 10, No. 6, pp. 1478-1484.

Torii, S., and Yang, W.-J., 1998, "Thermal Transport in Turbulent Couette Flows in Concentric Annuli for Various Prandtl Numbers," *Numerical Heat Transfer, Part A,* vol. 34, pp. 537-552.

Ulucakli, M.E., and Merte, H. Jr., 1990, "Nucleate Boiling with High Gravity and Large Subcooling," *Journal of Heat Transfer,* vol. 112, pp. 451-457.

Wang, C.S., and Greif, R., 1981, "The Effect of Impingement on Heat Transfer in Rotating Condensation," *International Journal of Heat and Mass Transfer,* vol. 24, No. 7, pp. 1097-1104.

Wang, T.Y., 1993, "Convection Heat Transfer from a Rotating or Non-rotating Axisymmetric Body," *International Journal of Heat and Fluid Flow,* vol. 14, No. 4, pp. 333-340.

Webb, R.L., Eckert, E.R.G., and Goldstein, R.J., 1971, "Heat Transfer and Friction in Tubes with Repeated-Rib Roughness," *International Journal of Heat and Mass Transfer,* vol. 14, pp. 601-617.

Wu, D. and Peterson, G.P., 1991, "A Review of Rotating and Revolving Heat Pipes," ASME paper No. 91-HT-24.

Yang, W.-J., Zhang, N., and Chiou, J., 1992, "Local Heat Transfer in a Rotating Serpentine Flow Passage," *Journal of Heat Transfer,* vol. 114, pp. 354-361.

Yanniotis, S., and Kolokotsa, D., 1996, "Experimental Study of Water Vapour Condensation on a Rotating Disc," *International Communications in Heat and Mass Transfer,* vol. 23, No. 5, pp. 721-729.

Appendix A Condensation in the Rotating Heat Pipe

The important assumptions used to model the film condensation process on the tapered wall of the rotating heat pipe are examined in more detail here. The vapour shear stress, momentum drag and the flow regime of the film are considered. The flow regime of the film is examined in two parts. In the first part the distribution of the film around the periphery of the wall is examined. The second part considers whether the film flow in the axial direction is laminar or turbulent.

Vapour Shear Stress. Following Song et al. (2003b), the ratio of the vapour shear stress at the liquid-vapour interface to the driving force in the liquid film along the wall is given by

$$R_1 = \frac{\tau_{v,\delta}}{\rho_l \omega^2 r \left(\sin\alpha - \cos\alpha \frac{d\delta}{dx} \right) \delta}, \tag{A.1}$$

where $\tau_{v,\delta}$ is the vapour shear stress at the free surface of the film, ρ is the density, ω is the engine rotation frequency, r is the local radius, α is the taper angle of the fin, δ is the film thickness and the subscript l refers to the liquid phase and v refers to the vapour phase. Following Daniels and Al-Jumaily (1975) and Song et al. (2003b), it was assumed that $d\delta/dx \ll \tan\alpha$ over the majority of the film for the case of a tapered condenser wall. Neglecting the pressure gradient contribution, the vapour shear stress ratio simplifies to

$$R_1 = \frac{\tau_{v,\delta}}{\rho_l \omega^2 r \sin\alpha \delta}. \tag{A.2}$$

Following Daniels and Al-Jumaily (1975) and Song et al. (2003b), the vapour shear stress was estimated using

$$\tau_{v,\delta} = \frac{1}{2} f \rho_v u_v^2, \tag{A.3}$$

where u_v is the mean velocity of the vapour flow and f is the friction factor given by

$$f = \frac{16}{\mathrm{Re}_v}, \tag{A.4}$$

for laminar flow when $\mathrm{Re}_v = {u_v D}/{\nu_v} < 2000$, and

$$f = \frac{0.0791}{\mathrm{Re}_v^{1/4}}, \tag{A.5}$$

for turbulent flow when $\mathrm{Re}_v > 2000$. The liquid film thickness was estimated using the conservation of mass of the liquid and vapour flow in the condenser and the velocity profile of the liquid film. The total mass flow rate entering the condenser section is given by (Daniels and Al-Jumaily, 1975)

$$\dot{m} = \frac{Q}{h_{fg}}, \tag{A.6}$$

where Q is the heat transfer rate of the system and h_{fg} is the latent heat of vapourization. The conservation of mass at a given plane across the condenser cross-section is given by

$$\dot{m} = \dot{m}_l + \dot{m}_v \tag{A.7}$$

Neglecting the vapour shear stress, a first estimate of the liquid film thickness is found from the velocity profile given by

$$\delta_l = \left(\frac{3\nu_l \dot{m}_l}{2\pi\rho_l \omega^2 R^2 \sin\alpha} \right)^{1/3}. \quad \text{(A.8)}$$

In this application, the vapour flow would impose a positive shear stress on the liquid film and would accelerate the liquid film along the wall. Neglecting the vapour shear stress in the formulation of the film thickness leads to an under prediction of the liquid film velocity at the interface and thus an over prediction of the shear stress yielding a conservative estimate. Thus, matching the shear stress at the interface was not evaluated here. The ratio R_1 was estimated as a function of the parameter $m^* = \dot{m}_l / \dot{m}_v$, in order to characterize how the ratio would vary along the length of the film. The results are shown in figure A.1 for typical heat transfer rates found in this application of 500W to 2000W using water and ethanol as the working fluids evaluated at 40°C. A 25.4 mm diameter condenser with a 2° taper angle rotating at a nominal speed of 5000 rpm was used. The results show that the vapour shear stress should be negligible for both fluids. The ratio R_1 was relatively large for $\dot{m}_l < \dot{m}_v$ because the vapour velocity in this case would be high while the liquid film is thin. This would occur over the initial portion of the condenser film. The ratio then decreases rapidly for $\dot{m}_l > \dot{m}_v$, remaining relatively constant because the vapour velocity continually decreases as more mass is condensed thus increasing the driving force in the liquid film. The ratio R_1 decreased as the rotation speed increased because the driving force in the film increased.

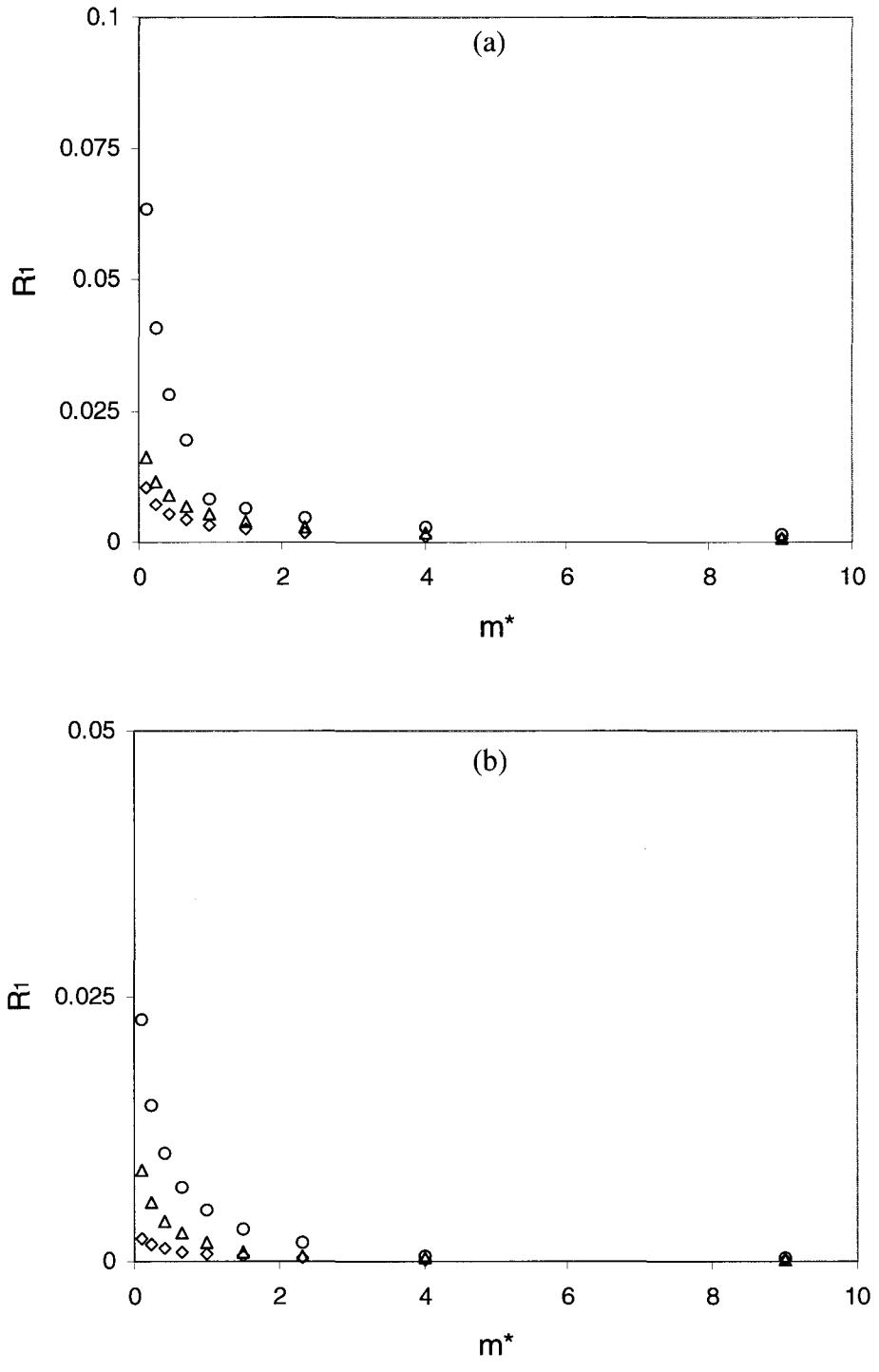

Figure A.1: The ratio R_1; (a) water, (b) ethanol; Q = ◊ 500W, Δ 1000W, o 2000W.

Momentum Drag. When the vapour condenses, it decelerates to the velocity of the liquid film and thus a drag force is imposed at the interface of the film due to the influx of momentum. This momentum drag force was compared to the driving force in the liquid film along the wall using

$$R_2 = \frac{\tau_{v,MD}}{\rho_l \omega^2 r \sin\alpha\delta}, \tag{A.9}$$

where τ_{MD} is the momentum drag. Assuming a one dimensional vapour flow, the momentum drag is given by (Daniels and Al-Jumaily, 1975)

$$\tau_{v,MD} = \left[\frac{d\dot{\Gamma}_l}{dx}\right]\left[u_v \cos\alpha - u_{l,\delta}\right], \tag{A.10}$$

where $\dot{\Gamma}_l$ is the mass flow rate of the liquid film per unit periphery. In the proposed condenser design, the length scale of the condenser is similar to the radius and thus assuming $d/dx \sim O(1/R)$, a first order estimate of the momentum drag is given by

$$\tau_{v,MD} \approx \frac{\dot{m}_l}{2\pi R^2}\left(u_v \cos\alpha - u_{l,\delta}\right), \tag{A.11}$$

where $u_{l,\delta}$ is the liquid velocity at the interface. The ratio R_2 is shown in figure A.2 for the same conditions used to characterize R_1. The momentum drag was found to be on the order of 0.1 to 1 and represents an important contribution to the overall momentum transfer in the liquid film. The momentum drag was larger for water than ethanol because the water film was thinner, owing to its higher thermal conductivity, and hence the driving forces were smaller. The momentum drag increased rapidly over the initial formation of the film where the influx of momentum due to condensation was dominant.

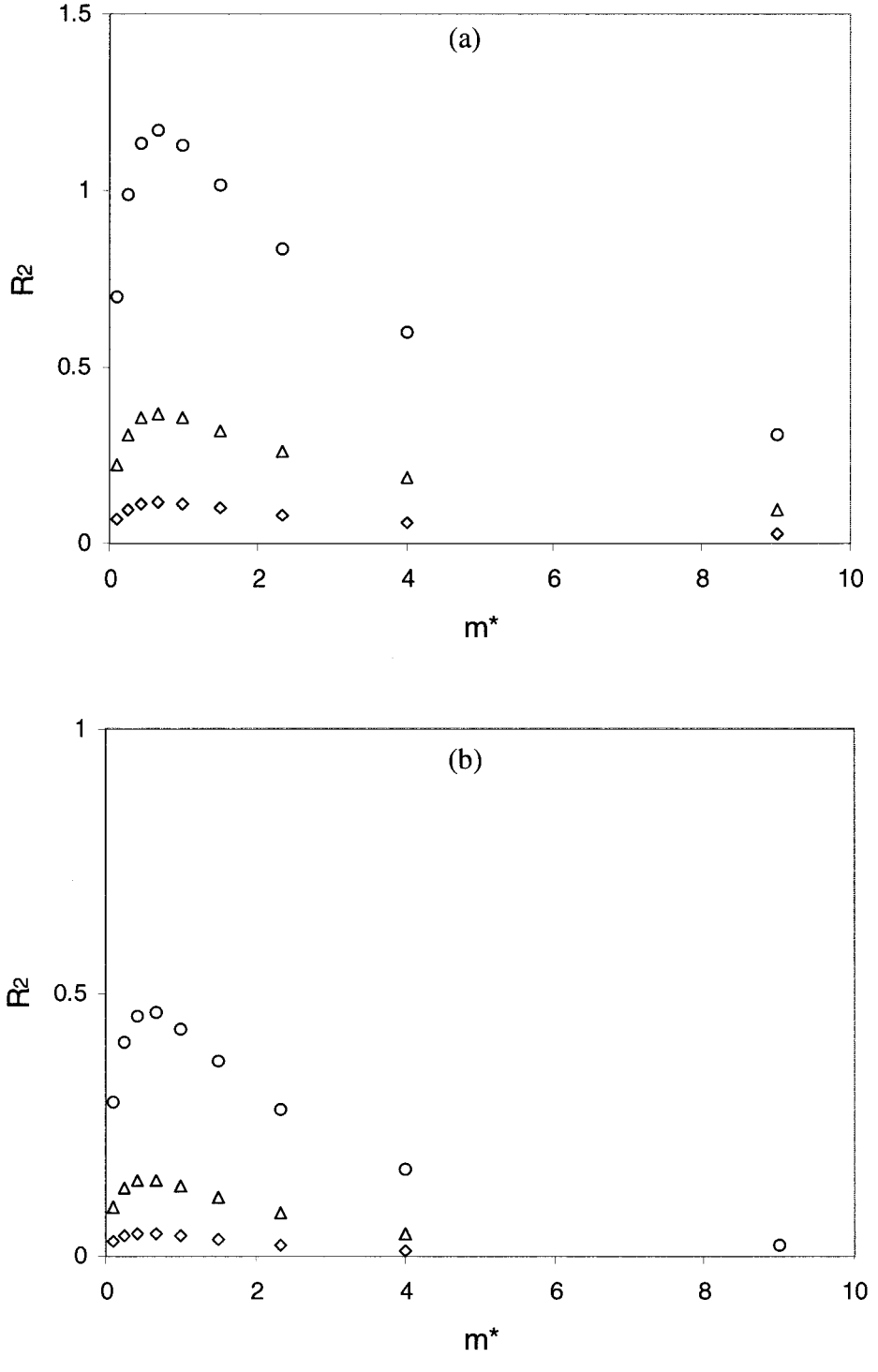

Figure A.2: The ratio R_2; (a) water, (b) ethanol; Q = ◊ 500W, Δ 1000W, o 2000W.

The momentum drag then decreased rapidly for $\dot{m}_l > \dot{m}_v$ because the difference between the velocity of the vapour and liquid decreases as well as the amount of condensation. The momentum drag also decreased as the rotation speed was increased.

Peripheral Film Distribution. Following Wu and Peterson (1991), the important parameters required to determine the liquid film flow regime around the periphery of the rotating heat pipe are the Froude number given by

$$Fr = \frac{\omega^2 R}{g}, \tag{A.12}$$

and the film rotational Reynolds number defined by

$$\mathrm{Re}_{\omega,l} = \frac{\omega \bar{\delta}^2}{\nu_l}, \tag{A.13}$$

where $\bar{\delta}$ is the average film thickness around the periphery. The boundary for the onset of solid body rotation in the liquid film is shown in figure A.3. Physically, when the heat pipe rotates the viscous shear rate at the wall draws the film against gravity. Clearly for low rotation speeds pooling will tend to occur in the bottom of the heat pipe whereas at high rotation speeds the film exhibits solid body rotation depending on the thickness. The Froude number was on the order of 350 – 5600 while the Reynolds number was on the order of 1 indicating that the film would be in solid body rotation in this application.

Axial Film Flow Regime. Following Carpenter and Colburn (1951), the liquid film is laminar for Reynolds numbers $\mathrm{Re}_{x,l} = {u_{l,\delta}\delta}/{\nu_l} < 240$. The Reynolds number was on the order of 1 to 10 for typical rotation speeds of 5000 rpm to 20000 rpm indicating that the film should be laminar in this application.

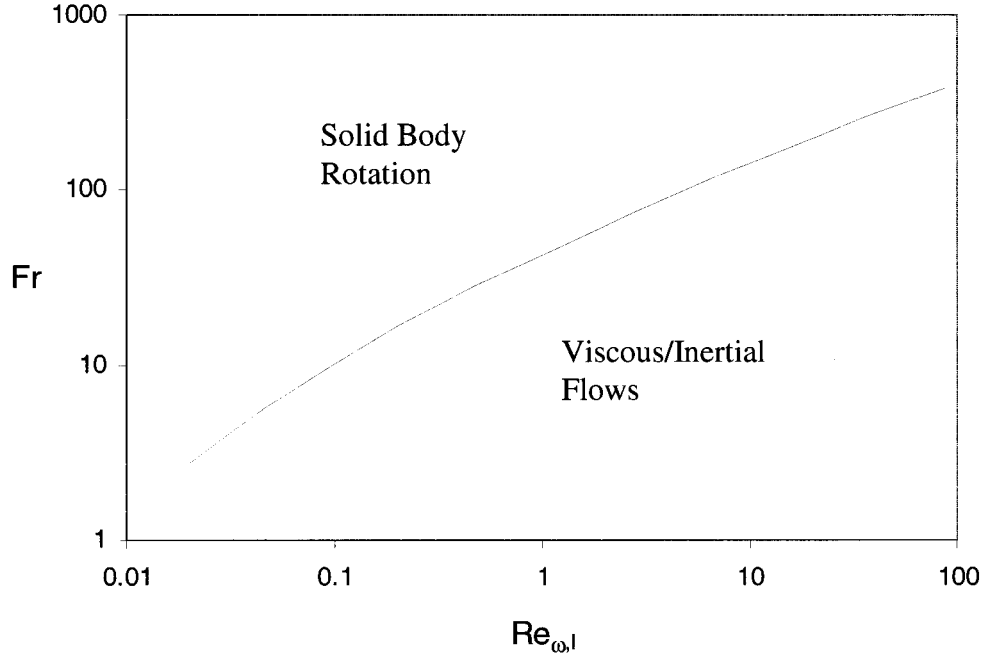

Figure A.3: Onset of solid body rotation in the condensate film from Wu and Peterson (1991).

Appendix B

B.1 Temperature Field in the End-wall of the Heat Pipe

The two dimensional form of Laplace's equation in cylindrical coordinates has the form

$$\frac{\partial^2 T}{\partial r^2}+\frac{1}{r}\frac{\partial T}{\partial r}+\frac{\partial^2 T}{\partial z^2}=0. \tag{B.1.1}$$

Following Anderson et al. (1984), the coordinate transformation $m=r$, $n=z/f(r)$, produces a grid with equal spacing in the radial direction and even spacing in the normal direction where $f(r)$ is the thickness of the nose cone as a function of the radius. The partial derivatives are given by

$$\frac{\partial}{\partial r}=\frac{\partial}{\partial m}-n\frac{f'}{f}\frac{\partial}{\partial n}, \tag{B.1.2}$$

$$\frac{\partial^2}{\partial r^2}=\frac{\partial^2}{\partial m^2}-2\frac{f'}{f}n\frac{\partial^2}{\partial m\partial n}+\left[2\left(\frac{f'}{f}\right)^2-\frac{f''}{f}\right]n\frac{\partial}{\partial n}+\left(\frac{f'}{f}\right)^2 n^2\frac{\partial^2}{\partial n^2}, \tag{B.1.3}$$

$$\frac{\partial^2}{\partial z^2}=\frac{1}{f^2}\frac{\partial^2}{\partial n^2}, \tag{B.1.4}$$

Substituting into Laplace's equation yields the heat equation in the new coordinate system given by

$$m\frac{\partial^2 T}{\partial m^2}+\frac{\partial T}{\partial m}+\left[mn^2\left(\frac{f'}{f}\right)^2+m\left(\frac{1}{f}\right)^2\right]\frac{\partial^2 T}{\partial n^2}-\left[2mn\left(\frac{f'}{f}\right)\right]\frac{\partial^2 T}{\partial m\partial n} + \left[2mn\left(\frac{f'}{f}\right)^2-mn\left(\frac{f''}{f}\right)-n\left(\frac{f'}{f}\right)\right]\frac{\partial T}{\partial n}=0 \quad \text{(B.1.5)}$$

Each partial differential for the interior nodal points was discretized using (Anderson et al. 1984),

$$\frac{\partial T}{\partial m}\approx\frac{T_{p+1,q}-T_{p-1,q}}{2\Delta m}, \quad \text{(B.1.6)}$$

$$\frac{\partial T}{\partial n}\approx\frac{T_{p,q+1}-T_{p,q-1}}{2\Delta n}, \quad \text{(B.1.7)}$$

$$\frac{\partial^2 T}{\partial m^2}\approx\frac{T_{p+1,q}-2T_{p,q}+T_{p-1,q}}{(\Delta m)^2}, \quad \text{(B.1.8)}$$

$$\frac{\partial^2 T}{\partial n^2}\approx\frac{T_{p,q+1}-2T_{p,q}+T_{p,q-1}}{(\Delta n)^2}, \quad \text{(B.1.9)}$$

$$\frac{\partial^2 T}{\partial m\partial n}\approx\frac{T_{p+1,q+1}-T_{p+1,q-1}-T_{p-1,q+1}+T_{p-1,q-1}}{4\Delta m\Delta n}. \quad \text{(B.1.10)}$$

The nodal equations were found by substituting the partial derivative approximations in to the transformed equation.

The nodal equations for the nodes on the outside boundary exposed to the atmosphere and the inside boundary exposed to the condensing film on the end wall of the heat pipe and pool were derived following Incopera and DeWitt (1996), using an energy balance method. The heat transfer modes for the half control volumes on either edge used to compute the energy balance are shown in figure 3.4. Beginning with the

edge exposed to the condensing film, the energy balance for the control volume is given by

$$q_1 + q_2 - q_3 - q_4 - q_5 = 0. \quad \text{(B.1.11)}$$

The conduction heat transfer modes in the r and z directions are given by

$$q_r = -kA_p \frac{\partial T}{\partial r}, \quad \text{(B.1.12)}$$

$$q_z = -kA_p \frac{\partial T}{\partial z}, \quad \text{(B.1.13)}$$

where A_p is the projected area of a given control volume surface normal to the direction. The projected area in the radial direction of the bottom surface of each control volume was estimated by

$$A_p = 2\pi\left(r - \frac{\Delta r}{2}\right)\left(\frac{\Delta z_{r-\Delta r} + \Delta z_r}{2}\right) = \left(\frac{\pi}{2}\right)\left(m - \frac{\Delta m}{2}\right)\Delta n\left(f(p) + f(p-1)\right), \quad \text{(B.1.14)}$$

while similarly at the top surface was estimated by

$$A_p = 2\pi\left(r + \frac{\Delta r}{2}\right)\left(\frac{\Delta z_r + \Delta z_{r+\Delta r}}{2}\right) = \left(\frac{\pi}{2}\right)\left(m + \frac{\Delta m}{2}\right)\Delta n\left(f(p+1) + f(p)\right). \quad \text{(B.1.15)}$$

The projected area in the r or m direction of the curved control volume surface following the body contours inside the solid was computed from

$$A_p = 2\pi\left|f_r'\right| r\Delta r = 2\pi\left|f'(p)\right| m\Delta m, \quad \text{(B.1.16)}$$

while in the z or n direction was computed from

$$A_p = 2\pi r\Delta r = 2\pi m\Delta m. \quad \text{(B.1.17)}$$

The convection heat transfer across the condensate film and into the surface was determined from

$$q_{conv} = q_5 = 2\pi r \Delta r \frac{k_{nc,film}}{\delta}\left(T_{sat} - T_{r,0}\right) = 2\pi m \Delta m \frac{k_{nc,film}}{\delta}\left(T_{sat} - T_{p,q}\right). \quad \text{(B.1.18)}$$

In this case, q_4 was neglected because it was assumed that a sufficient number of nodes in the z direction would cause the projected area in the radial direction of this curved surface to be very small. Substituting the heat transfers into the energy balance gives the nodal equation. For nodes in contact with the pool instead of the film, the convection heat transfer was neglected by setting $q_2 = 0$, and the nodal equations were modified to reflect this.

The energy balance for the control volume on the outside face exposed to the ambient is given by

$$q_1 + q_2 + q_3 - q_4 - q_5 = 0. \quad \text{(B.1.19)}$$

The heat transfer from the surface to the atmosphere was modeled as a combination of effects due to forced convection and the impacting sub-cooled water droplets. The convection heat transfer was computed from

$$q_{conv} = h_{conv} A_s \left(T_{p,q} - T_{\inf}\right), \quad \text{(B.1.20)}$$

where h_{conv} is the convection heat transfer coefficient and A_s is the surface area of the control volume exposed to the atmosphere approximated using

$$A_s \approx 2\pi r \Delta r \sqrt{1 + f'(r)^2} = 2\pi m \Delta m \sqrt{1 + f'(p)^2}. \quad \text{(B.1.21)}$$

The heat advected from the surface to the impinging droplets was estimated using

$$q_{adv} = 2\pi \rho_{LWC} U C_p r \Delta r \left(T_{r,z=f} - T_{\inf}\right) = 2\pi \rho_{LWC} U C_p m \Delta m \left(T_{p,q} - T_{\inf}\right), \quad \text{(B.1.22)}$$

and the total heat transfer from the surface was computed from

$$q_5 = q_{conv} + q_{adv}. \tag{B.1.23}$$

An effective heat transfer coefficient $h_{\inf}$ representing the effects due to forced convection and advection from the impinging droplets was thus defined using

$$h_{\inf} \equiv h_{conv} + \frac{\rho_{LWC} U C_p}{\sqrt{1+f'(p)^2}}. \tag{B.1.24}$$

The conduction heat transfer modes and the nodal equations were determined using the same procedure as before.

At the interface with the junction, the temperature was assumed constant at T_j through the thickness. This boundary condition was incorporated by solving the temperature field only up to the row of nodes below this boundary. For this row of nodes, references to temperatures $T_{p+1,q-1}$, $T_{p+1,q}$, $T_{p+1,q+1}$ in the nodal equations were set equal to T_j and the products with the respective transport coefficients were combined with the source term. The temperature field was solved using the matrix inversion method.

B.2 Heat Transfer Analysis for the Junction

The energy balance for the junction region is shown in figure B.2.1, is given by

$$q_{endwall-j} + q_{fin-j} - q_{j-\inf} - q_{j-nc,shell} = 0. \tag{B.2.1}$$

The heat transfer from the end wall of the heat pipe to the junction was determined by summing the heat contributions from each control surface along the interface using the

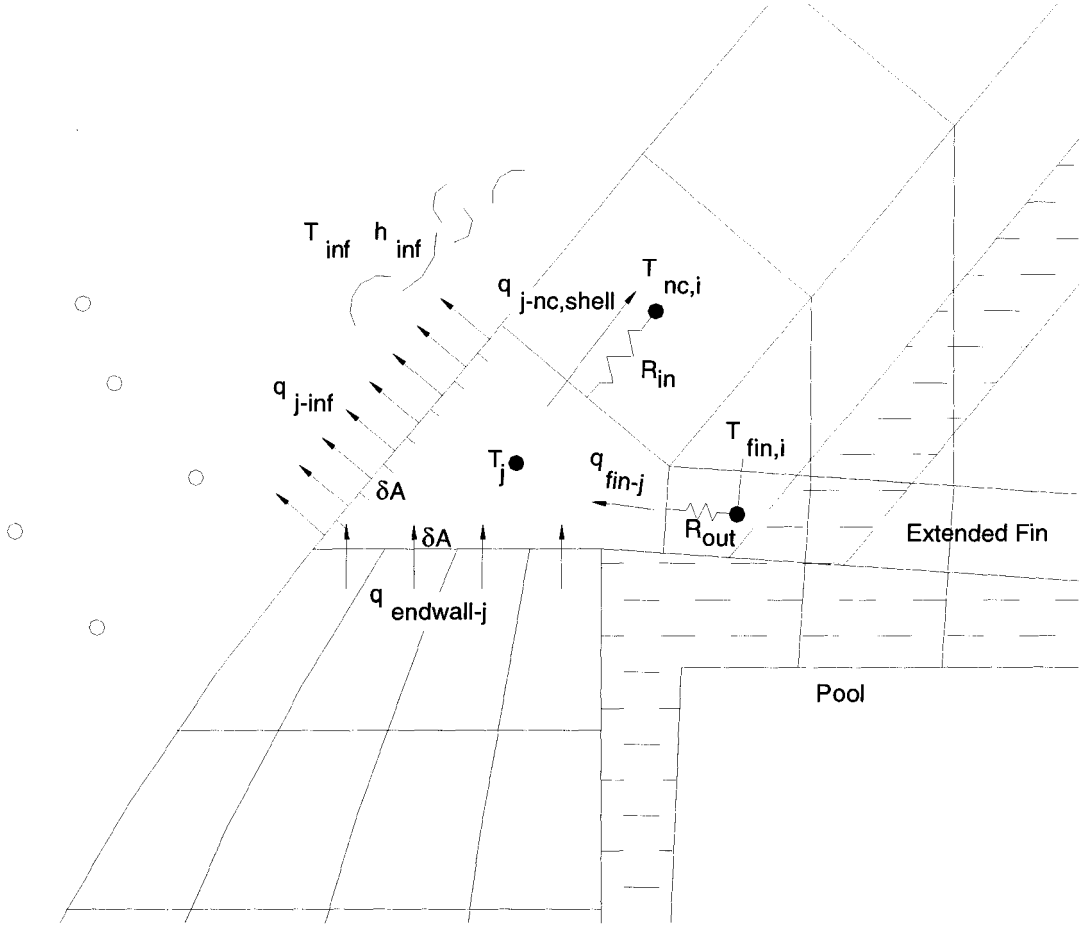

Figure B.2.1: Heat transfer modes in the junction region.

two dimensional temperature field results. The heat transfer rate from one control surface is given by

$$q_{endwall-j} = \sum \delta q_{endwall-j} = \sum -k\delta A \frac{\partial T}{\partial r}. \qquad \text{(B.2.2)}$$

The temperature gradient was evaluated using the two-dimensional model. The conduction heat transfer at the fin-junction interface and the nose cone shell-junction interface were estimated using Fourier's conduction law using the temperature gradients from the nose cone shell and extended fin temperature profiles. The convection heat transfer to the atmosphere was evaluated by discretizing the length of the exposed surface of the junction into small control surfaces and summing the individual contributions computed from

$$q_{j-\text{inf}} = \sum \delta q_{j-\text{inf}} = \sum h_{\text{inf}} \delta A\left(T_j - T_{\text{inf}}\right). \qquad \text{(B.2.3)}$$

B.3 Numerical Solutions

A schematic of the important quantities used to compute the solution of the heat transfer in the condenser are shown in figure B.3.1. The computer algorithm that was used is outlined schematically in figure B.3.2. Figure B.3.2a is the main computer algorithm and figure B.3.2b is a sub-algorithm used to compute the height of the pool that balances the condensation mass flow rate and the total mass flow in the heating channels. Note that the *i* sub-script refers to the center of the discrete control volume while the *j* sub-script refers to the face of the control volume.

The evaporator film thickness was solved using a similar shooting method to the condensate films. A schematic of the computer algorithm used to solve the film and heat transfer is given in figure B.3.3.

q_1 = Heat transfer across nose cone pole film.
q_2 = Nose cone pole convection to ambient.
q_3 = Nose cone pole to junction conduction.
q_4 = Heat transfer across the fin film.
q_5 = Fin to junction conduction.
q_6 = Fin to filler conduction.
q_7 = Convection to ambient from the junction.
q_8 = Junction to nose cone shell conduction.
q_9 = Filler to nose cone shell conduction.
q_{10} = Channel to nose cone shell convection.
q_{11} = Nose cone shell to ambient convection.
$\dot{m}_1$ = Total mass flow condensed on nose cone pole.
$\dot{m}_2$ = Total mass flow condensed on fin.
$\dot{m}_3$ = Total mass flow in the heating channels.
δ_1 = Nose cone pole film profile.
δ_2 = Fin film profile.
$h_{channel}$ = Heating channel heat transfer coefficient.
h_{inf} = Nose cone surface heat transfer coefficient.
$T_{channel}$ = Heating channel temperature distribution.
T_j = Junction temperature.
T_{inf} = Ambient air temperature.
$T_{ncshell}$ = Nose cone shell temperature distribution.
T_{fin} = Extended fin temperature distribution.
T_{ncpole} = Thicker pole region temperature distribution.
T_{sat} = Vapour saturation temperature.

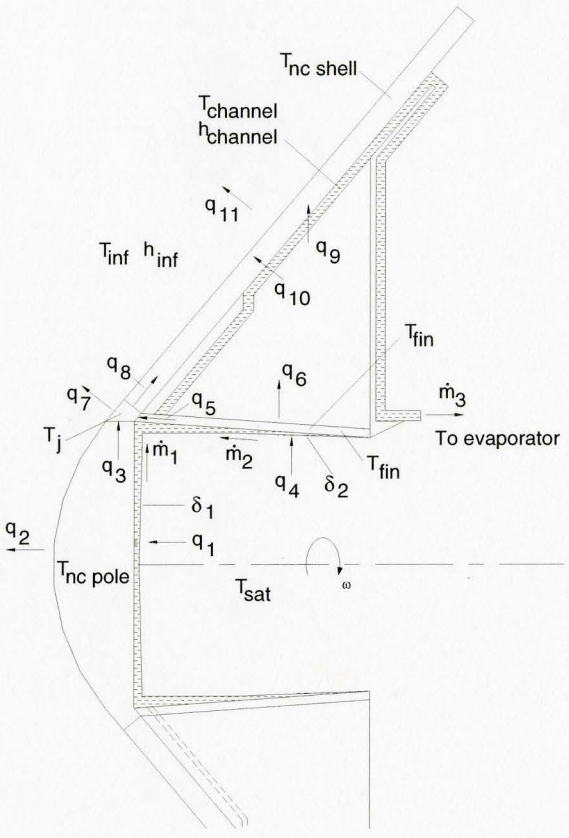

Figure B.3.1: The heat transfer modes, temperatures, mass flow rates and film distributions used in the computer algorithm to determine the overall condenser hydraulic and thermal equilibrium.

(a)

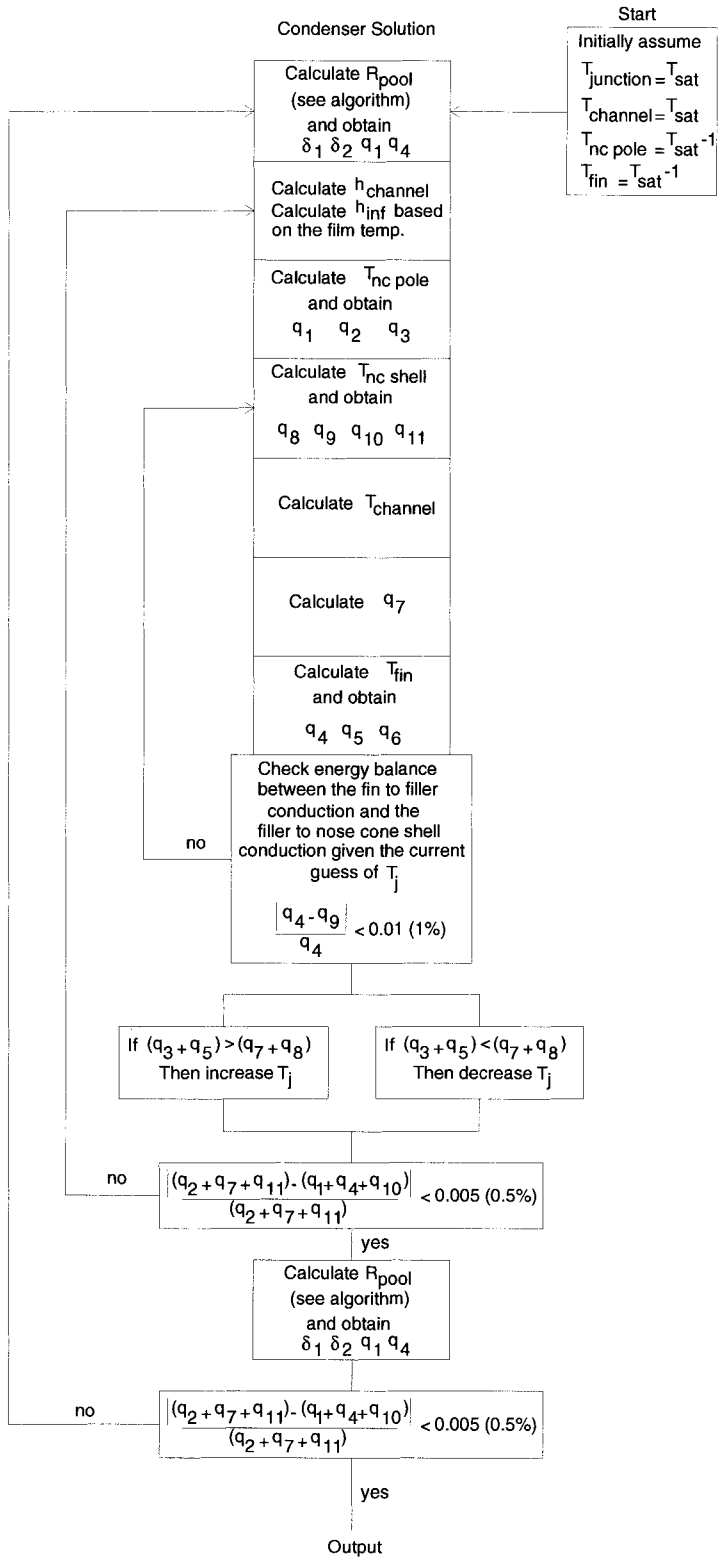
Condenser Solution
Start
Initially assume
$T_{junction} = T_{sat}$
$T_{channel} = T_{sat}$
$T_{nc\ pole} = T_{sat}^{-1}$
$T_{fin} = T_{sat}^{-1}$
Calculate R_{pool} (see algorithm) and obtain $\delta_1\ \delta_2\ q_1\ q_4$
Calculate $h_{channel}$ Calculate h_{inf} based on the film temp.
Calculate $T_{nc\ pole}$ and obtain $q_1\ q_2\ q_3$
Calculate $T_{nc\ shell}$ and obtain $q_8\ q_9\ q_{10}\ q_{11}$
Calculate $T_{channel}$
Calculate q_7
Calculate T_{fin} and obtain $q_4\ q_5\ q_6$
Check energy balance between the fin to filler conduction and the filler to nose cone shell conduction given the current guess of T_j
$\frac{|q_4 - q_9|}{q_4} < 0.01\ (1\%)$
no
If $(q_3 + q_5) > (q_7 + q_8)$ Then increase T_j
If $(q_3 + q_5) < (q_7 + q_8)$ Then decrease T_j
no
$\frac{|(q_2 + q_7 + q_{11}) - (q_1 + q_4 + q_{10})|}{(q_2 + q_7 + q_{11})} < 0.005\ (0.5\%)$
yes
Calculate R_{pool} (see algorithm) and obtain $\delta_1\ \delta_2\ q_1\ q_4$
no
$\frac{|(q_2 + q_7 + q_{11}) - (q_1 + q_4 + q_{10})|}{(q_2 + q_7 + q_{11})} < 0.005\ (0.5\%)$
yes
Output

(b)

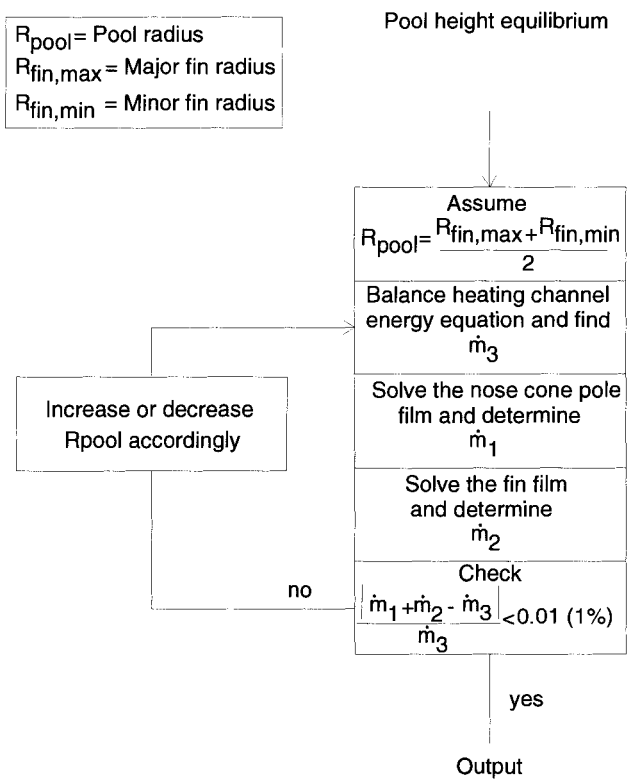

Figure B.3.2: (a) the main algorithm used to determine overall thermal and mass flow rate equilibrium of the aero-engine condenser, (b) the algorithm used to compute the equilibrium pool radius (height).

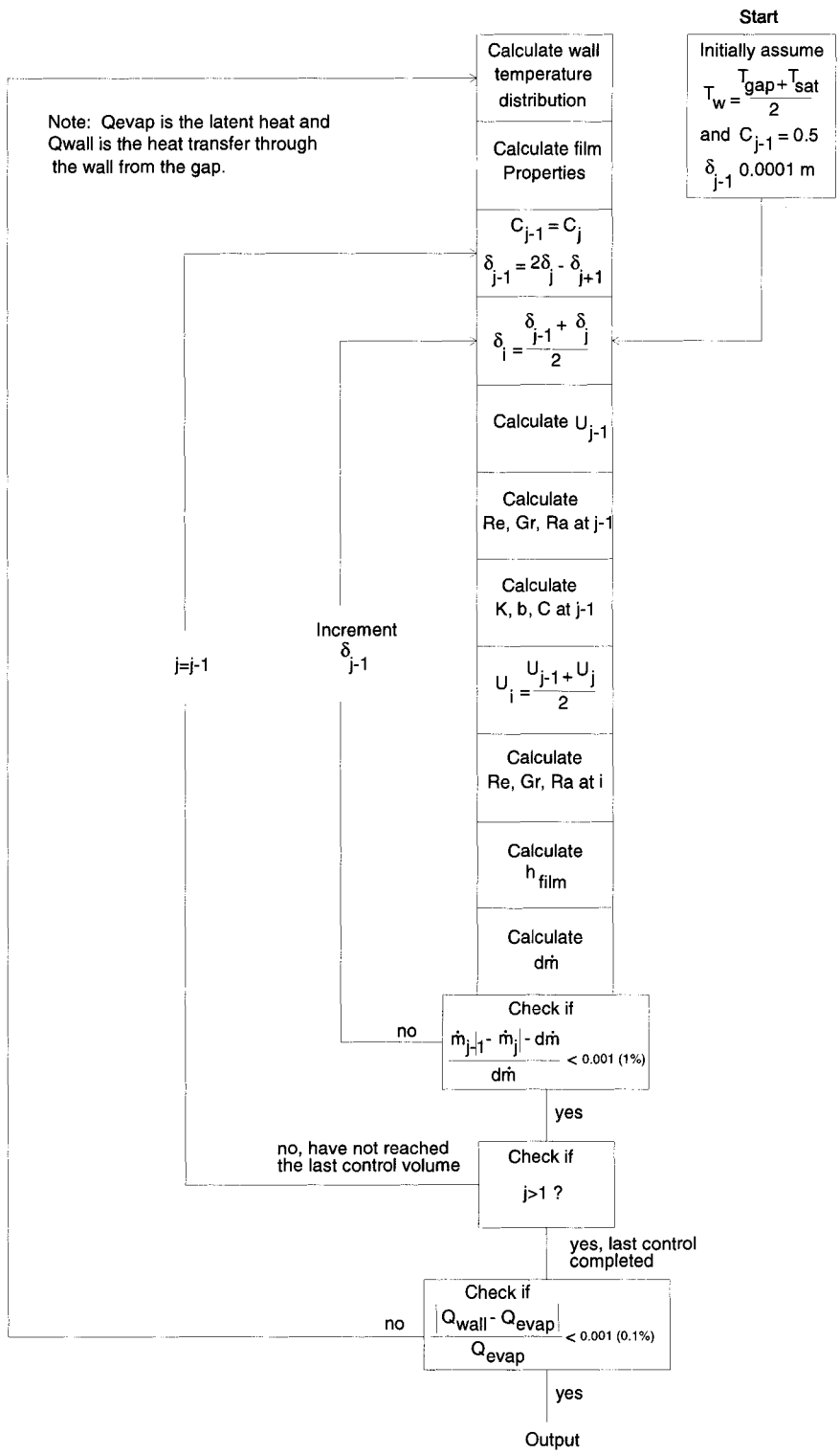

Figure B.3.3: The algorithm used to solve the aero-engine evaporator heat transfer. The basic program outputs are the film profiles; free stream velocity and heat transfer quantities.